UNIVERSIDADE FEDERAL DE SANTA CATARINA
DEPARTAMENTO DE AUTOMAÇÃO E SISTEMAS
PROGRAMA DE PÓS-GRADUAÇÃO EM ENGENHARIA DE AUTOMAÇÃO E SISTEMAS

Juan Gabriel Guerrero Grijalva

Contributions to Folding Mechatronics: a Scissor-like Elements based Approach

Florianópolis
2021

Juan Gabriel Guerrero Grijalva

Contributions to Folding Mechatronics: a Scissor-like Elements based Approach

Tese submetida ao Programa de Pós-Graduação em Engenharia de Automação e Sistemas da Universidade Federal de Santa Catarina para a obtenção do título de Doutor em Engenharia de Automação e Sistemas.
Supervisor: Prof. Edson Roberto De Pieri, Dr.
Co-supervisor:: Prof. Daniel Martins, Dr.

Florianópolis
2021

Ficha de identificação da obra elaborada pelo autor,
através do Programa de Geração Automática da Biblioteca Universitária da UFSC.

Grijalva, Juan Gabriel
Contributions to Folding Mechatronics: a Scissor-Like Elements Based Approach / Juan Gabriel Grijalva ; orientador, Edson Roberto De Pieri, coorientador, Daniel Martins, 2022.
130 p.

Tese (doutorado) - Universidade Federal de Santa Catarina, Centro Tecnológico, Programa de Pós-Graduação em Engenharia de Automação e Sistemas, Florianópolis, 2022.

Inclui referências.

1. Engenharia de Automação e Sistemas. 2. Automação. 3. Mecatrônica. 4. Mecanismos. 5. Controle. I. De Pieri, Edson Roberto. II. Martins, Daniel. III. Universidade Federal de Santa Catarina. Programa de Pós-Graduação em Engenharia de Automação e Sistemas. IV. Título.

Juan Gabriel Guerrero Grijalva

Contributions to Folding Mechatronics: a Scissor-like Elements based Approach

O presente trabalho em nível de Doutorado foi avaliado e aprovado por banca examinadora composta pelos seguintes membros:

Prof. Marcelo Becker , Dr.
Universidade de São Paulo - Escola de Engenharia de São Carlos

Prof. Henrique Simas, Dr.
Universidade Federal de Santa Catarina

Prof. Leonardo Mejia Rincón, Dr.
Universidade Federal de Santa Catarina - Blumenau

Prof. Eugênio de Bona Castelan, Dr.
Universidade Federal de Santa Catarina

Certificamos que esta é a **versão original e final** do trabalho de conclusão que foi julgado adequado para obtenção do título de Doutor em Engenharia de Automação e Sistemas.

Documento assinado digitalmente
Werner Kraus Junior
Data: 09/03/2022 14:49:12-0300
CPF: 531.085.239-53
Verifique as assinaturas em https://v.ufsc.br

Prof. Werner Kraus Junior, Dr.
Coordenação do Programa de
Pós-Graduação

Documento assinado digitalmente
Edson Roberto de Pieri
Data: 09/03/2022 10:48:46-0300
CPF: 002.042.498-13
Verifique as assinaturas em https://v.ufsc.br

Prof. Edson Roberto De Pieri, Dr.
Orientador

Florianópolis, 2021.

Este trabajo es dedicado para la reina de mi vida, Mary Grijalva Pasquel, mi madre adorada.

ACKNOWLEDGEMENTS

First of all, I would like to thank God, everything I do is on his behalf. I also thank Prof. Edson de Pieri, my supervisor, who, in addition to scientific knowledge, has taught me honesty, dedication, discipline, ethics, and professionalism through example. I truly admire how he can develop activities as a teacher, researcher, supervisor, and Technologica-Center Director in such a correct way and always with a smile on his face ready to help and serve those who need it.

When I started my postgraduate activities at UFSC in 2015, I had no idea whatsoever about research or topics related to writing articles, presentations at conferences, knowledge about journals, etc. Consequently, I thank Prof. Eugênio de Bona Castelan, who was my supervisor in my master's degree, for having started me as a researcher. The patience, professionalism, and amount of hours that Prof. Eugênio invested in my training as a researcher is incredible.

Professors who marked my academic life such as (in alphabetical order): Prof. Alexandre Trofino, Prof. Augusto Rodrigues, Prof. Cesar Deschamps, Prof. Daniel Coutinho, Prof. Daniel Martins, Prof. Gisele Orgado, Prof. Henrique Simas, Prof. Juan Pagano, Prof. Julio Normey, Prof. Nestor Roqueiro, Prof. Rodolfo Flesch, Prof. Victor De Negri, among others. I just want to say: thank you!, you are like superheroes for me whom I try to imitate.

I would also like to thank Enio Snoeijer, who does a wonderful job as secretary of PPGEAS and has given me the peace of mind to focus merely on my studies. Finally, I would like to thank the entire city of Florianopolis and its kind people who welcomed me like a brother at all times. Of course, I also acknowledge the financial support of CAPES which made it possible to fulfill my dream through the scholarship they awarded me.

“Solo Dios es perfecto; sin embargo, si vais a hacer
cualquier cosa, hacedlo lo mas perfectamente
posible o simplemente no lo hagais.”
“Only God is perfect; however, if you are going
to do something, do it as perfectly
as possible, otherwise don’t do it.”
(Jose Guerrero Medina)

RESUMO

A mecatrônica dobrável é uma tecnologia que surge devido à necessidade de desenvolver dispositivos que possam ser transportados de forma compacta e na hora de serem utilizados podem ser desdobrados atingindo um tamanho maior de acordo com a aplicação. No projeto de um dispositivo mecatrônico, duas etapas devem ser consideradas: a primeira focada no projeto da estrutura tangível, hardware, onde o principal desafio consiste no projeto da estrutura dobrável; e a segunda etapa consiste no desenvolvimento de um algoritmo de controle, software, que considera as necessidades e restrições do sistema físico. Elementos do tipo tesoura (ETT) são usados para o projeto da estrutura dobrável. Um ETT consiste em um par de vigas unidas por um pivô, uma junta de rotação, para permitir a rotação livre de uma viga em relação à outra em torno do eixo do pivô. Existe uma grande variedade de ETT que facilita a formação de estruturas com morfologias diversas. Com o objetivo de projetar estruturas dobráveis leves, o uso de origami acoplado aos ETTs também é explorado. Quatérnions duais são usados na análise cinemática de ETTs. Na análise cinemática, são considerados aspectos relacionados à cinemática direta e ao espaço de trabalho. A equação de estados é representada por meio de um sistema massa-mola-amortecedor cujos parâmetros são obtidos por meio da teoria de identificação de sistemas. No projeto do controlador, duas abordagens são exploradas: uma em tempo contínuo e outra em tempo discreto. Em tempo contínuo, é apresentada uma abordagem robusta baseada em desigualdades de matrizes lineares. Por outro lado, um controlador preditivo é empregado para lidar com a abordagem em tempo discreto. Restrições na entrada e saída do sistema dinâmico são consideradas pelo controlador preditivo.

Palavras-chave: Estruturas dobráveis. Cinemática. Controle. Mecatrônica.

RESUMO EXPANDIDO

Introdução

O crescimento exponencial da população mundial e a concentração populacional em áreas urbanas levam à necessidade global de desenvolver produtos eficientes, bem como ao surgimento de novas tecnologias com foco na economia de espaço. Sob essa perspectiva, a mecatrônica dobrável visa colaborar com o desenvolvimento de novas ferramentas para o projeto de dispositivos que têm a capacidade de se compactar em um pequeno espaço, com aplicação em áreas como automotiva, aeroespacial, automação residencial, manufatura, robótica, smartphones, etc. Nas últimas décadas, as estruturas dobráveis têm sido bastante utilizadas em inúmeros produtos. Uma das estruturas dobráveis mais conhecidas são aquelas formadas por elementos do tipo tesoura (ETT). Um ETT consiste em um par de vigas unidas por um pivô, uma junta de rotação, para permitir a rotação livre de uma viga em relação à outra em torno do eixo do pivô. Devido ao grande número de elos e juntas necessários para montar as estruturas com ETTs, sua análise cinemática torna-se complicada. Existem abordagens baseadas em matrizes para lidar com a análise cinemática de ETTs. A principal desvantagem das abordagens baseadas em matrizes é a quantidade de linhas e colunas necessárias para representar a relação cinemática entre os vários pontos na estrutura ETT. Neste manuscrito é apresentada uma abordagem baseada em quatérnios duais (QD) para lidar com a análise cinemática de estruturas ETT. Entre as principais vantagens da utilização de QD, na análise cinemática de ETTs, visando a eficiência em termos de esforço computacional e a possibilidade de orientar vetores, retas e planos. As estruturas formadas pelos ETTs são geralmente formadas por elementos homogêneos, podendo aproveitar a exponenciação dos QDs na análise cinemática de montagens homogêneas. Algoritmos baseados em QDs são apresentados para lidar com o cálculo do espaço de trabalho dos ETTs. Com o objetivo de desenvolver uma estrutura leve e dobrável com uma parede fina, um novo tipo de mecanismo, origami tipo tesoura (OTT), é apresentado neste trabalho. O OTT é inspirado no design de leques. Usando um padrão simétrico simples de dobras, quatro morfologias OTTs são exibidas. A equação de estados é representada por meio de um sistema massa-mola-amortecedor cujos parâmetros são obtidos por meio da teoria de identificação de sistemas. A ferramenta matemática utilizada na identificação de sistemas é a técnica dos mínimos quadrados. No projeto do controlador, duas abordagens são exploradas: uma em tempo contínuo e outra em tempo discreto. O controlador robusto, utilizado em tempo contínuo, consiste em definir as incertezas do sistema dentro de um politopo convexo gerado a partir das restrições. Por meio de desigualdades matriciais lineares, condições são estabelecidas para estabilizar e definir um desempenho arbitrário no sistema em malha fechada. Em tempo discreto, é definido um controlador preditivo de tipo generalizado que oferece a possibilidade de lidar com restrições na entrada e saída do controlador.

Objetivos

O principal objetivo deste trabalho é contribuir com ferramentas para o desenvolvimento de dispositivos que tenham a capacidade de compactar mecanismos em um reduzido tamanho usando elementos do tipo tesoura. Para atingir o objetivo principal, os objetivos específicos desta tese são: analisar cinematicamente as estruturas dos ETTs usando quatérnios duais; calcular o espaço de trabalho e as restrições de movi-

mento; explorar o uso de ETTs em conjunto com origami no projeto de estruturas leves dobráveis; projetar produtos com aplicações em domótica, especificamente móveis inteligentes; identificar as limitações e restrições do sistema, que serão consideradas no momento de determinar o algoritmo de controle; obter um modelo matemático que represente a dinâmica do sistema; simular dinamicamente os sistemas de malha fechada e testar os algoritmos de controle em tempo contínuo e em tempo discreto. Com os métodos e ferramentas apresentadas nesta tese, objetiva-se auxiliar projetistas no desenvolvimento de novos dispositivos dobráveis.

Metodologia
Inicialmente, o material existente é revisado em relação à análise cinemática, dinâmica e controle de elementos do tipo tesoura (ETT). O objetivo desta revisão é estabelecer em quais áreas novos métodos podem ser desenvolvidos para o projeto mecatrônico de sistemas baseados em ETTS. Quatérnios duais (QD) são usados para análise cinemática. A cinemática de cada tipo de ETT é representada por um quatérnio dual diferente. A exponenciação do quatérnio é usada em estruturas homogêneas. Usando a programação em Matlab, é testada a eficiência, do ponto de vista computacional, da exponenciação de quatérnios duais. Algoritmos são usados para calcular o espaço de trabalho dos ETTs, que são testados por meio de programas executáveis em Matlab. Além disso, os valores resultantes dos algoritmos do espaço de trabalho são plotados a fim de corroborar os resultados. A cinemática direta de estruturas tridimensionais também é representada por QDs, para isso, a cinemática dos conectores também é representada por QDs. As estruturas dos ETTs são programadas no Simscape. O Simscape é um pacote Simulink que permite programar parâmetros dinâmicos de corpos rígidos como inércia, massa, atrito, rigidez, etc., sendo possível representar sistemas multicorpos de forma próxima à realidade. Para obter as equações de estados que representam a dinâmica dos sistemas ETT, é utilizada a teoria da identificação de sistemas. Os ETTs programados no Simscape são estimulados por meio de entradas do tipo degrau e rampa para obter uma resposta do sistema. Os dados de entrada e saída do sistema são usados em um programa executável baseado em mínimos quadrados para obter um modelo dinâmico. O modelo dinâmico é simplificado em um modelo massa-mola-amortecedor. Uma vez que um modelo dinâmico está disponível, abordagens de tempo contínuas e discretas são aplicadas para projetar um controlador. Em tempo contínuo, é usado um controlador robusto com condições de estabilidade baseadas em desigualdades matriciais lineares (LMI). A programação quadrática é usada para resolver o LMI, especificamente o pacote Matlab CVX. A estratégia de controle de malha fechada é simulada no Simscape. De acordo com os resultados obtidos sobre o desempenho dos sistemas, pode-se concluir sobre a eficácia da estratégia de controle robusto. Além disso, os parâmetros dinâmicos são variados no programa Simscape para testar a robustez do controlador. Em tempo discreto, é aplicado um controlador preditivo que otimiza o erro do sistema de malha fechada em um horizonte previamente estabelecido pelo projetista. O controlador preditivo do sistema é do tipo generalizado, o que permite lidar com limitações e restrições na entrada e saída do sistema. A programação de otimização do controlador é desenvolvida em Matlab. No projeto e simulação de mecanismos semelhantes a origami, o pacote Grasshopper do software Rhinoceros é usado, bem como o 3ds Max.

Resultados e Discussão
Representações cinemáticas baseadas em quatérnios duais (QD) são apresentadas

para cada um dos tipos de ETT. As representações cinemáticas usando QDs foram mais compactas em comparação com as convencionais usando matrizes. O tempo de execução do computador usando a exponenciação dos QDs é mantido constante, enquanto o tempo de execução é exponencialmente incremental quando os QDs são usados para representar cada um dos ETTs. Os algoritmos apresentados para calcular o espaço de trabalho dos ETTs foram eficazes para todos os tipos de ETTs. Usando exemplos de uma lâmpada e um suporte de TV dobrável, o uso de QDs para orientar vetores, linhas e planos foi mostrado. O controlador robusto usado em tempo contínuo mostrou-se eficaz na estabilização e definição de um desempenho arbitrário para vários tipos de estruturas compostas por ETTs. Os parâmetros do sistema dinâmico, previamente definidos como incertos, foram variados para comprovar que as condições de estabilidade definidas no politopo são atendidas. O controlador preditivo de tempo discreto também se mostrou eficaz na estabilização de sistemas ETT. Limitações nos atuadores, bem como restrições na saída do sistema foram consideradas no projeto do controlador preditivo. Sua eficácia foi comprovada em móveis inteligentes e também em um sistema de usinagem. Por fim, foi analisado o uso do origami em conjunto com ETTs para a obtenção de estruturas flexíveis leves e de paredes finas, que têm aplicações potenciais em áreas como aeronáutica, robótica, arquitetura, energias renováveis, entre outras.

Considerações Finais

No momento da publicação deste manuscrito, a última tendência em smartphones são os Folds que são telefones que podem ser carregados no bolso em um tamanho pequeno, mas quando usados pelo usuário podem ser desdobrados atingindo um tamanho grande por parte da tela do dispositivo. A mesma tendência é observada em automóveis híbridos, drones, móveis, casas e estruturas em projetos espaciais, razão pela qual a Mecatrônica Dobrável é considerada uma tecnologia necessária para desenvolver produtos que atendam a demanda de usuários globalmente. É importante notar que esta tecnologia não se limita ao uso de elementos do tipo tesoura, uma vez que existem várias estruturas dobráveis, com as quais uma maior variedade de dispositivos Fold podem ser desenvolvidos.

Palavras-chave: Mecatrônica. Estruturas dobráveis. Quatérnios duais. Cinemática. Controle robusto. Controle preditivo. Origami.

ABSTRACT

Folding Mechatronics is a technology that arises due to the need to develop devices that can be transported in a compact way, and when they are used, they can be deployed, reaching a larger size according to what is necessary. In the design of a mechatronic device, two steps must be considered: the first focused on the design of the tangible structure, hardware, where the main challenge is the design of the folding structure; and the second stage consists of the development of a control algorithm, software, which considers the needs and restrictions of the physical system. Scissor-like elements (SLE) are used for the design of the folding structure. An SLE consists of a pair of beams joined by a pivot, a rotation joint, to allow free rotation of one beam in relation to the other around the pivot axis. There is a wide variety of SLE that facilitates the formation of structures with different morphologies. In order to design lightweight folding structures, the use of origami coupled with SLEs is also explored. Dual quaternions are used in the kinematic analysis of SLEs. In the kinematic analysis, aspects related to direct kinematics and the workspace are considered. The state equation is represented by means of a mass-spring-damper system whose parameters are obtained through systems identification theory. In the controller project, two approaches are explored: one in continuous time and the other in discrete time. In a continuous-time, a robust approach based on inequalities of linear matrices is presented. On the other hand, a predictive controller is employed to handle the discrete time approach. The predictive controller handles restrictions on the input and the output of the dynamic system.

Keywords: Mechatronics. Foldable structures. Dual quaternions. Kinematics. Robust control. Predictive control. Origami.

LIST OF FIGURES

LIST OF TABLES

LIST OF ABBREVIATIONS AND ACRONYMS

ARX	Auto-regressive with exogenous input
CAD	Computer-aided design
CARIMA	Controller auto-regressive with integrated moving-average
DQ	Dual quaternion
GAE	Angulated scissor-like elements
GPC	Generalized predictive control
GPCC	Constrained generalized predictive control
IFAC	International Federation of Automatic Control
LMI	Linear matrix inequalities
MPC	Model Predictive Control
MSD	Mass-spring-damper
SDQ	Screw dual quaternion
SLE	Scissor-like elements
SLO	Scissor-like origami
Ts	Sampling time
ZOH	Zero-order hold

LIST OF SYMBOLS

Cl	Clifford space
$\mathbb{R}$	Euclidian space
$\oplus$	Subspaces direct sum
$P\mathbb{R}$	Hyperspace
ε	Dual part of a number
$\mathcal{V}$	Lyapunov function
$\mathbb{S}$	Definite symmetric matrix
$\mathbb{C}$	Complex number
$\cap$	Sets intersection
$diag$	Main diagonal of a matrix
$\otimes$	Kronecker product

CONTENTS

1 INTRODUCTION

The need to make folding equipment ranges from the Mongolian yurts to more sophisticated devices such as the Da Vinci's umbrella or the velum of the Roman Coliseum's velum (DE TEMMERMAN, N., 2007). Nowadays, the most recent trend of smartphones is to have the ability to fold, that is, to be able to be transported in a small size and to be able to be deployed at the time of use, reaching a large size on the part of the screen. In recent years, due to the exponential increase in world population and the massive concentration of people in urban areas, scientists and engineers have been studying and conceiving efficient solutions, in terms of space, in areas such as automotive, architecture, civil engineering, solar energy grids, among others. For example, Zhao et al. (2011) present the synthesis of a folding stair (as shown in Figure 1) using a homogeneous SLE configuration.

Figure 1 – Folding stairs.

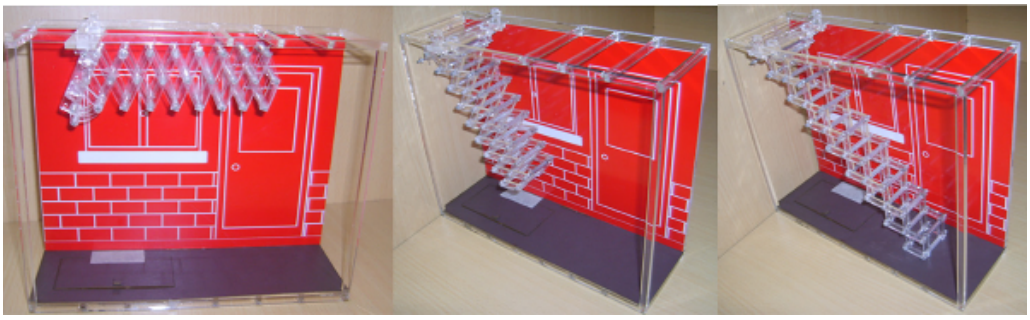

Source – Tsinghua University (2007).

The folding stairs' objective is to avoid allocating in-home stairs and uniting the two floors without constantly occupying the stairs' space.

Figure 2 – Curling bridge in London.

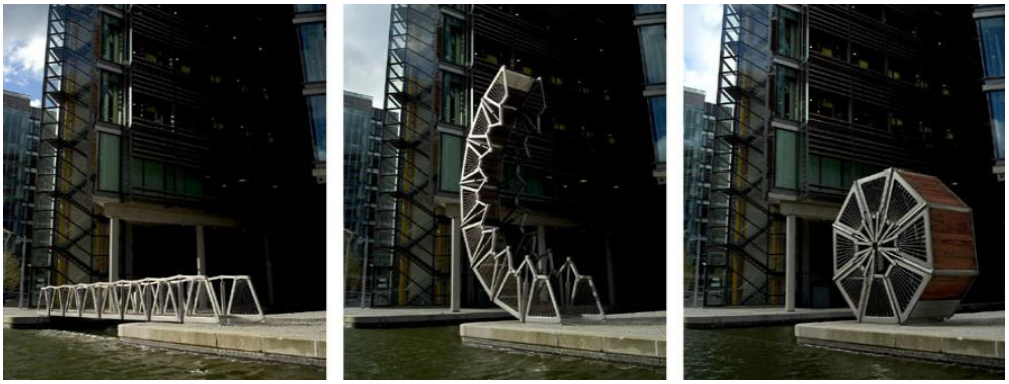

Source – Heatherwick-Studio (2009).

The Rolling Bridge (as can be seen in Figure 2) from Grand Union Canal in London is another example. This bridge (SANABRIA-BARBOZA, D., 2015) was developed by the British designer Thomas Heatherwick and designed by Anthony Hunt with Packman Lucas. The passage of boats is available since the bridge curls up until its two ends join to form an octagonal shape measuring one-half of the waterway's width at that point. Hoberman made the transformable Iris Dome (HOBERMAN, C., 1993) depicted in Figure 3. This invention offers the possibility to assemble a roof in a few minutes by using Angulated scissor-like elements (GAE).

Figure 3 – Iris dome.

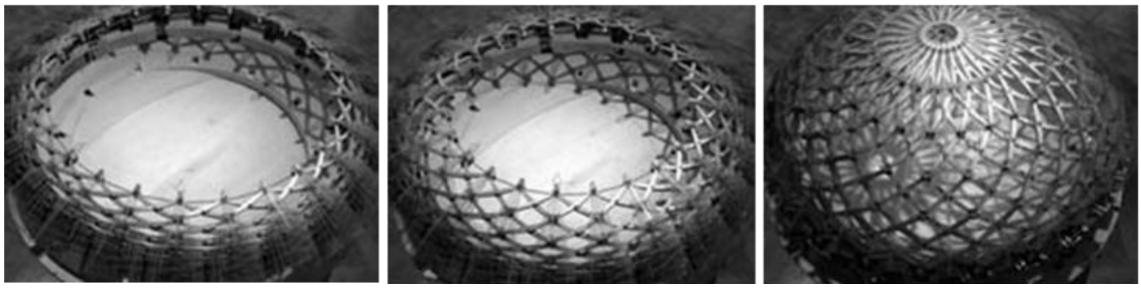

Source – (HOBERMAN, C., 1993).

NASA developed a deployable shield (as shown in Figure 4), transforming into a huge shell. This invention permits blocking off the shine of distant stars. Thus it is possible to employ a telescope to observe other planets where intelligent life could exist (CASEMENT et al., 2012).

Figure 4 – Starshade Project.

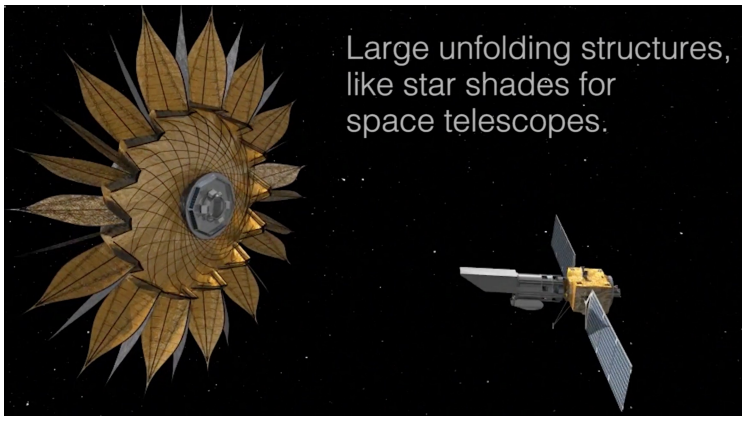

Source – NASA (2012).

The mechanical structures from the examples mentioned above have sophisticated built-in controllers making them mechatronic applications. According to the Inter-

national Federation of Automatic Control (IFAC), Mechatronics is the synergy between mechanics, control and automation systems. Successes in the design of mechatronic devices include considering aspects both in the physical or hardware part and in the control or software part at the same time aiming to obtain a product optimized in both aspects. Accordingly, in this document, Folding Mechatronics is presented as a new technology that seeks the design of mechatronic devices that can compact in small size as possible. Folding Mechatronics' main characteristic when compared to conventional Mechatronics is the in-depth study of reconfigurable mechanisms, specifically rigid and soft deployable structures such as origami, tensegrity, scissor-like elements, among others. From the perspective of control and automation, in Folding Mechatronics, the challenge is to stabilize and obtain satisfactory performance, for the user, by the deployable structures. It is important to consider that the deployable structures may present singularities, uncertainties, limitations and restrictions which the control algorithm must consider to guarantee stability and good performance. Figure 5 shows a diagram of folding mechatronics, showing the main research areas and their interaction. In Figure 5, it can be seen how it is necessary to consider aspects, from a mechanical perspective, related to statics, kinematics, ergonomy, workspace and dynamics. Similarly, control, embedded systems, and communication networks are necessary to design optimized folding mechatronic products from a control and automation perspective.

Figure 5 – Folding Mechatronics - research areas.

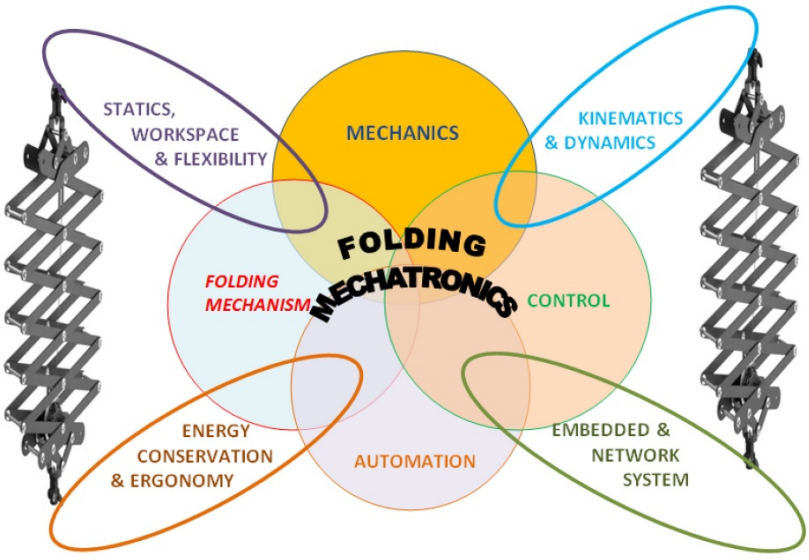

Source – From the author.

Following the diagram of Figure 5, this manuscript presents tools for the mechatronic design of folding devices. Besides, several applications are presented using folding mechatronics, based on home automation (domotics), energy storage, machin-

ing, and space exploration. The folding mechanism chosen to be used in this work is the SLE and origami. The structures composed of SLE are kinematically analyzed using DQ. In dynamic modeling, an identification technique based on least squares is used. For the controller, two options are explored: a robust strategy in continuous-time and a predictive strategy in discrete-time. A brief introduction of these topics are shown in the remaining of this chapter.

1.1 SCISSOR-LIKE ELEMENTS

The SLE concept comes from archaic scissors. The main idea is to assemble various scissors through pivots and revolute joints to lead to more complex configurations. For example, Escrig (1985) presents some structures of translational SLE assemblies. The next year Zanardo (1986) developed a novel configuration using polar SLE assemblies. Many years later Hoberman patented a closed structure of symmetrical GAE, creating the famous toy known as Hoberman sphere. The following year Hoberman patented a radial expansion truss structure (HOBERMAN, C., 1991) using non-symmetrical SLE. Various researchers have been publishing and patenting forms and devices based on translational, polar and angulated planar and spherical SLE. Aiming to show a summary of SLE based on past research, SLE classification based on the motion and geometry is detailed in the following subsections.

1.1.1 Translational with Constant Bar Length

When all bars have the same lengths, and the pivots are located in the middle of the bars, the system constitutes a perfect planar surface. This type of scissor structures is typically used in daily life, commonly applied on rods to dry clothes, industrial elevators, toys, among other applications. The entry movement of the mechanism is between the first two collinear hinges.

Figure 6 – Translational SLE with Constant Bar Length.

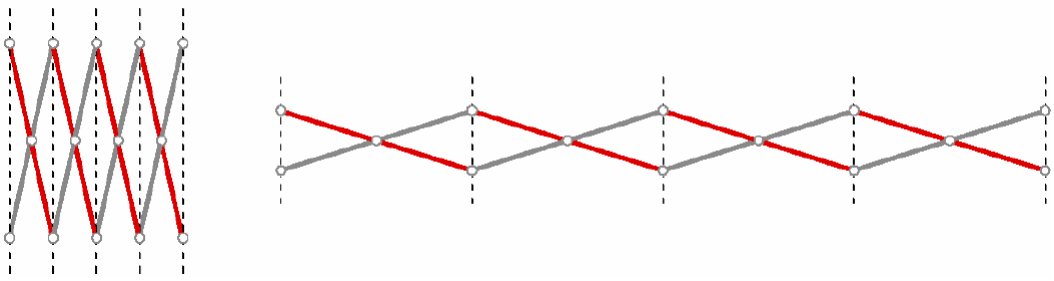

Source – (DE TEMMERMAN, N., 2007).

These symmetrical structures (as can be seen in Figure 6) can form infinite assemblies without risking collision in the folding-unfolding process.

1.1.2 Translational with Different Bar Length

This type of folding structure shows a rectilinear movement so that infinite assemblies do not present a risk of collision in the folding-unfolding process. Based on Figure 7, this type of SLE condition is $a = d$ and $b = c$. Note that the pivots are located in the middle of the bars.

Figure 7 – Translational SLE with Different Bar Length.

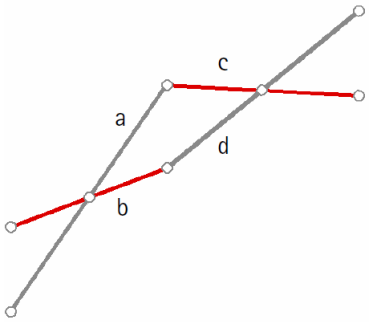

Source – (DE TEMMERMAN, N., 2007).

This type of SLE serves to form structures with an upward or downward inclined shape.

1.1.3 Polar units

When in a planar translational unit the intermediate hinge is moved away from the bars' center a polar unit is formed with unequal semi-bars *a* and *b*, as depicted in Figure 8.

Figure 8 – Polar unit.

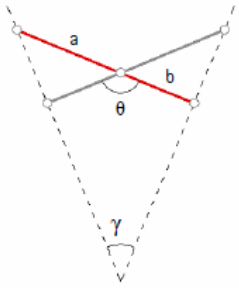

Source – (DE TEMMERMAN, N., 2007).

It is the eccentricity of the intermediate hinge which generates curvature during deployment. The unit lines intersect at an angle γ. This angle varies strongly as the unit deploys, and the intersection point moves closer to the unit as the curvature increases.

1.1.4 Angulated units

Unlike standard pantograph units with straight bars, angulated units consist of two rigidly connected semi-bars of length *a* that form a central kink of amplitude β. Because Chuck Hoberman invented them, they are commonly denoted as Hoberman's units. As opposed to polar units, the major advantage is that angulated units subtend a constant angle γ during deployment (Figure 9).

Figure 9 – Angulated unit or Hoberman's unit.

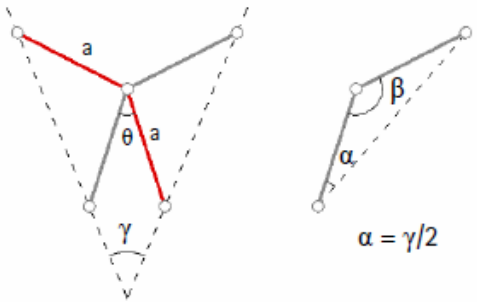

Source – (DE TEMMERMAN, N., 2007).

For this to occur, the bar geometry has to be such that $\alpha = \frac{\gamma}{2}$. This implies that angulated elements can be used for radially deploying closed loop structures, capable of retracting to their perimeter, which is impossible to accomplish with translational or polar units, which demonstrate a linear deployment.

Figure 10 – Radially foldable linkage example.

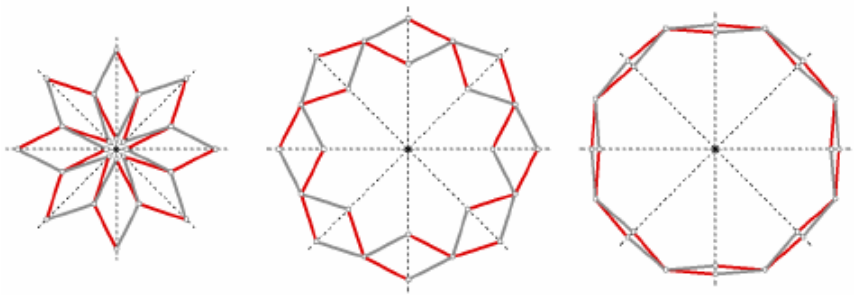

Source – (DE TEMMERMAN, N., 2007).

Figure 10 shows a circular linkage with angulated elements in its undeployed and

deployed configuration. The structure shown in Figure 10 consists of two layers of identical angulated elements, of which one layer is formed by elements in clockwise direction (marked in gray). Simultaneously, the other one is arranged in the counter-clockwise direction (marked in red). As the structure deploys, each layer undergoes a rotation, equal in magnitude but opposite to each other.

1.2 FUNDAMENTALS OF DUAL QUATERNION

Quaternions have proven themselves in many science and computing fields as unambiguous, uncumbersome, computationally efficient method to represent rotational information. Dual quaternion (DQ) is interesting and important because they cut down the volume of algebra. They make the solution more straightforward and robust (CHEVALLIER, D., 1991). Dual quaternion allows unifying the translation and rotation into a single state; instead of defining separate vectors. While matrices offer a comparable alternative to DQ, they can be inefficient and cumbersome in comparison. Dual quaternion provides a compact, unambiguous, singularity-free, and computational minimalistic rigid transform (RADAVELLI et al., 2015). Besides, DQ is the most efficient and most compact form of representing rotation and translation. Dual quaternion can easily take the place of matrices in hierarchies at no additional cost (CHEVALLIER, D., 1991). For rigid hierarchies that combine and compare rigid transforms on a frame-by-frame basis (e.g., character inverse kinematics and joint constraints), alternative methods such as matrices need to be converted to quaternions to generate reliable contrast data. This can be done without any conversion using DQ.

1.2.1 Advantages of dual quaternions

Dual quaternions are used as a tool for expressing and analyzing the physical properties of rigid bodies. Dual quaternion can formulate a problem more concisely, solve it more rapidly and in fewer steps, present the result more plainly to others, be put into practice with fewer code lines, and debugged effortlessly. Furthermore, there is no loss of efficiency; DQ can be just as efficient if not more efficient than using matrix methods. There are several reasons for using DQ, which are summarized as follows (RADAVELLI et al., 2015):

- Singularity-free.
- Un-ambiguous.
- Shortest path interpolation.
- Most efficient and compact form for representing rigid transforms (3x4 matrix 12 floats compared to a DQ 8 floats).

- Unified representation of translation and rotation.
- It can be integrated into a current system with little coding effort.
- The individual translation and rotational information are combined to produce a single invariant coordinate frame.
- The possibility to orientate straight lines, vectors and planes. Opposite to the conventional techniques, which allow only to deal with points.

1.2.2 Quaternions

Quaternions were introduced by Hamilton in 1866 and have been widely accepted up to the present time. Quaternions are an extension of complex number theory to formulate a four-dimensional manifold. A quaternion is defined as:

$$q = a_0 + a_1 i + a_2 j + a_3 k = a_0 + \mathbf{q} \tag{1}$$

where a_0, a_1, a_2 and a_3 are the real values, while i, j, k are the imaginary part. Based on Clifford algebra, the imaginary part has the following properties:

- $i^2 = j^2 = k^2 = -1$
- $jk = i$, $kj = -i$
- $ki = j$, $ik = -j$
- $ij = k$, $ji = -k$

To simplify the explanation about their operations, Equation 1 is represented by $q = (w, v)$ being w the scalar component and v the vector component. So, quaternions can perform the fundamental arithmetic operations as follows:

1. Addition: $q_1 + q_2 = (w_1 + w_2, \quad v_1 + v_2)$
2. Product:
   a) Scalar product: $a_0 q = (a_0 w, a_0 v)$
   b) Homogeneous product: $q_1 q_2 = (w_1 w_2 - v_1 v_2, \quad w_1 v_2 + w_2 v_1 + (v_1 \times v_2))$
3. Conjugate: $q^* = (w, -v)$
4. Norm: $\|q\| = qq^*$

Further reading on quaternions can be found in (RADAVELLI et al., 2015).

1.3 DUAL QUATERNION

When quaternions are combined with dual number theory, it is gotten DQ which Clifford presented in 1882. While the unit quaternion, a quaternion with norm equal to one, only can represent rotation, the unit DQ can represent both translation and rotation. Each DQ consists of eight elements or two quaternions. The two quaternion elements are called the real part and the dual part as follows

$$\begin{aligned} h = & \quad q_o + \varepsilon q_d \\ = & \quad a_0 + a_1 i + a_2 j + a_3 k + \varepsilon(b_0 + b_1 i + b_2 j + b_3 k) \end{aligned} \tag{2}$$

where q_o and q_d are quaternions and a_i, and b_i are real values. Let recall the dual number property $\varepsilon^2 = 0$, then the elementary arithmetic operations necessary to use DQ are:

1. Addition: $h_1 + h_2 = q_{o1} + q_{o2} + \varepsilon(q_{d1} + q_{d2})$
2. Product:
   a) Scalar product: $a_0 h = (a_0 q_o, a_0 q_d)$
   b) Homogeneous product: $h_1 h_2 = q_{o1} q_{o2} + \varepsilon(q_{o1} q_{d2} + q_{d1} q_{o2})$
3. Conjugate: $h^* = q_o^* + \varepsilon q_d^*$
4. Norm: $\|h\| = hh^*$
5. Unit condition: $\|h\| = 1 \Rightarrow q_o^* q_d + q_d^* q_o = 0 \quad \wedge \quad q_o q_d^* = 1.$

1.4 CONTROL STRATEGIES BASED ON LMI AND PREDICTIVE CONTROL

In the last two decades, LMI has emerged as a powerful tool in the field of control systems analysis and design (DUAN et al., 2013). Many problems, such as state feedback synthesis, robustness analysis and design, can be reduced to convex or quasi-convex problems involving LMI. Due to successful developments of efficient and reliable algorithms for solving LMI, these problems can now be solved both efficiently and numerically reliably, thereby making this the most attractive feature of LMI. Using LMI in the analysis and design of control systems, and with the help of MATLAB, or the open-source software packages YALMIP and CVX, more and more theoretical and practical control applications can be solved, which might not have been otherwise possible using traditional methods.

Predictive control is an advanced process control method that the process industry has used in chemical plants and oil refineries since the 1980s.In recent years it has also been used to control power systems. Controllers for this type of control depend

on dynamic models of the process in question, more often empirical linear models obtained by system identification. The main advantage of the MPC is the fact that it allows the immediate time slot to be optimized while also taking into account future time slots. This is achieved by optimizing a finite time horizon but only implementing the current time slot. The MPC can anticipate future events and take control actions accordingly. Conventional controllers do not have this prediction feature. The MPC almost universally implements a digital control system, although research is currently available to achieve faster response times with specially designed analog circuitry (VICHIK et al., 2014). This technique can deal with limitations and constraints in the dynamic system. This feature can be deeply appreciated in Chapter 5.

1.5 THESIS OBJECTIVES

This work presents contributions to folding mechatronics whose main purpose is to develop devices that can fold and unfold as necessary. In the development of these devices, the design of the folding structure is critical. Since there is many mechanisms to form folding structures, this thesis focuses explicitly on SLE use. Consequently, this manuscript's main objective is to show tools for the mechatronic design of folding devices that use SLE in areas such as kinematics, dynamics, and control.

1.5.1 Kinetostatic design

In kinetostatic design, the objectives defined below are related to the tangible part, hardware, of the system; in this case the structure composed mainly of SLE.

- Kinematically analyze the structures of SLE using DQ.
- Calculate workspace and movement constraints.
- Explore the use of origami in the design of lightweight folding structures.
- Design products with home automation applications, specifically smart furniture.
- Identify the limitations and restrictions of the system, which will be considered when determining the control algorithm.

Once the tangible part is ready, the mechatronic's device software objectives are detailed below.

1.5.2 Dynamics and control

Every mechatronic device must have a controller that adapts to the uncertainties, limitations and constraints of the hardware and the needs of the user in terms of

performance; thus, the specific objectives in the area of dynamics and control are shown below.

- Obtain a mathematical model that represents the dynamics of the system.
- Dynamically simulate the systems and validate the dynamic models.
- Design controllers in continuous-time and discrete-time considering uncertainties, limitations, and constraints.

1.6 THESIS CONTRIBUTIONS

The original contributions of this thesis can be organized in two stages: one dedicated to the mechanics and the other one dedicated to automation.

1.6.1 Mechanical design of SLE-based structures

The contributions concerning mechanical design are highlighted, such as the use of DQ in the kinematic analysis of SLE, the identification of restrictions in the unfolding of structures, and origami in conjunction with SLE; all summarized below.

1.6.1.1 Use of DQ in the kinematic analysis of SLE

Dual quaternion can represent kinematic relations of extended SLE structures. In the case of homogeneous structures, solutions based on exponentiation are presented to reduce the computational execution time. In heterogeneous structures, the use of connectors, also represented by DQ, to form three-dimensional structures is explored. To compute the workspace and identify singularities in the deployment of structures, algorithms based on DQ are presented. Through practical examples, the possibility of orienting vectors, lines and planes stands out, which is possible thanks to the use of DQ.

1.6.1.2 Origami and SLE

A new type of semi-soft mechanism is presented, which combines SLE and origami, allowing the possibility of forming large and lightweight structures with potential applications in space exploration, energy storage, robotics, home automation. One of the advantages of this hybrid mechanism is that the rigid part composed of SLE can be used to perform kinematic analysis of the semi-soft structure.

1.6.2 Automation of SLE-based devices

Contributions relative to the automation of SLE-based devices, in continuous-time and discrete-time, are detailed below.

1.6.2.1 Dynamic model

SLE-based structures' dynamic model is obtained through the theory of identification of systems, specifically least squares. The states equation is simplified in an MSD model.

1.6.2.2 Controller in continuous-time

In continuous-time, a robust controller is presented, which considers uncertainties in the dynamic model. The uncertainties are previously defined in a simplex. The stability and stabilization conditions are defined through LMI, which considers the Lyapunov stability theorems.

1.6.2.3 Controller in discrete-time

A model-based predictive controller is used in discrete-time. The use of limitations in actuators and restrictions in the dynamic performance of SLE-based systems is explored. These algorithms are tested in domotics and machining applications.

1.7 THESIS OUTLINE

Chapter 1 introduces deployable devices and the origin of Folding Mechatronics and its areas of interaction. Based on previous works, it is presented a review of SLE, DQ, LMI and predictive control approaches. Besides, the objectives and contributions of this manuscript are detailed in this chapter.

Chapter 2 shows the use of DQ in the kinematic analysis of planar and spherical SLE complemented with practical applications based on domotics.

Chapter 3 depicts scissor-like origami, a novel hybrid mechanism composed mainly of SLE and origami. Also, the kinematic analysis of many points in the structure of these mechanisms is performed using the DQ approach presented in Chapter 2.

Chapter 4 introduces an approach, based on identification theory, to deal with the dynamics of SLE based systems. Also, it is presented a continuous-time strategy to deal with uncertainties in the control of SLE systems.

Chapter 5 shows how to deal with limitations and constraints in SLE-based systems using a discrete-time strategy based on MPC.

Chapter 6 details the conclusions and perspectives to continue with the research shown in this manuscript.

2 KINEMATIC ANALYSIS OF SCISSOR-LIKE ELEMENTS USING DUAL QUATERNIONS

This chapter presents a standard approach, based on DQ, to deal with the kinematic analysis of SLE. Kinematic relations of homogeneous SLE are simplified using DQ exponentiation. The steps to identify kinematic singularities are detailed by an algorithm. A second algorithm is introduced to deal with the computation and plotting of reachable and dexterous workspace. In this approach, not just points and vectors but lines and planes are represented by DQ. Applications on domotics are good examples of motion of points, lines, and planes.

2.1 RIGID DISPLACEMENTS BY CLIFFORD ALGEBRA

Quaternions have proven to be efficient at representing rotations with clear geometric meaning (TSAI, L., 1999; LI; DAI, J., 2015; YU; LI; JIANGUO; BENCIOLINI, B., 2017) unfortunately, they do not handle translations. William Clifford introduced DQ to combine rotations and translations while retaining the benefits of the rotations representation of quaternion. This section presents concepts, notations, and definitions about Clifford algebra and their application in DQ's displacement of rigid bodies. Well-known algebraic systems like complex numbers, matrix, vector, quaternion are included in Clifford algebra and unified in a coherent mathematical language (RADAVELLI, L., 2012). Rotation and translation of geometric entities such as points, lines, planes, areas and volumes are basic operations in Clifford algebra. The following sections of this chapter exploit these characteristics.

Definition 2.1

A n-dimensional Clifford space (Cl(n)*), viewed as an extension of Euclidean vector space, becomes Clifford algebra, with* 2^n *elements, when geometric product is defined. The orthonormal basis* $\{\sigma_1, \ldots, \sigma_n\}$ *considered as Euclidean vector* $\mathbb{R}^n$ *is constrained to*

$$\sigma_i\sigma_j + \sigma_j\sigma_i = 0, \forall i \neq j \quad \wedge \quad \sigma_i^2 = \varepsilon,$$

where $\varepsilon = \underbrace{+1}_{\lambda^p}, \underbrace{0}_{\lambda^r}, \underbrace{-1}_{\lambda^q}$ *represents the signature of any generator* σ_i*.*

The Clifford space notation to this signature is $Cl_{\lambda^p,\lambda^r,\lambda^q}(n)$. The dimension n of the Clifford space can be computed as the sum of the signatures $\lambda^{p,r,q}$.

Definition 2.2

The elements in Cl(n) *are called according to the amount of generators, i.e, an element with* σ_i *is called vector, with* $\sigma_i\sigma_j$ *is called bivector, with* $\sigma_i\sigma_j\sigma_k$ *is called trivector, and so on. The elements with zero generators are scalars.*

Based on Definition 2.2, a multivector is a general element of Clifford algebra, and the number of generators defines the degree of any element.

Definition 2.3

A j-dimensional subspace of Cl(n)*, defined by homogeneous multivectors of j degree, is denoted by* $\langle M \rangle_j$.

By using Definition 2.3, it is possible to decompose a Clifford space as follows

$$Cl_{\lambda^p,\lambda^r,\lambda^q}(n) = \langle M \rangle_0 \oplus \langle M \rangle_1 \oplus \ldots \oplus \langle M \rangle_n . \tag{3}$$

In Equation (3), " $\oplus$ " represents the direct sum of subspaces.

Definition 2.4

The subspaces of Cl(n) *with even degrees, i.e,* $\langle M \rangle_2$, $\langle M \rangle_4$*, and so on, are defined as spinors and the direct sum of the spinors of Cl*(n) *is denoted by* $Cl^+(n)$.
The spinors are employed in rotation and translation of rigid bodies (LOUNESTO, 2001; SELIG, 2004; HESTENES, 2012). The following subsection presents these concepts.

2.1.1 Isomorphism between Clifford algebra and dual quaternions

Based on the definitions established above, the DQ's concept and its property to rotate and translate rigid bodies are presented in this subsection. The primal Clifford space employed in rigid displacements is $Cl_{0,1,3}(4)$, which belongs to the hyperspace $P\mathbb{R}^3$ with orthonormal basis $\left\{\sigma_1^r, \sigma_1^q, \sigma_2^q, \sigma_3^q\right\}$. Note that by Definition 2.1 it can be written:

$$\left(\sigma_1^r\right)^2 = 0 \quad \wedge \quad \left(\sigma_1^q\right)^2 = \left(\sigma_2^q\right)^2 = \left(\sigma_3^q\right)^2 = -1.$$

Also, by Definition 2.1 and 2.3 note that there exist 2^4 elements in $Cl_{0,1,3}(4)$ as follows

$$\begin{aligned} Cl_{0,1,3}(4) =& \langle M \rangle_0 \oplus \langle M \rangle_1 \oplus \langle M \rangle_2 \oplus \langle M \rangle_3 \oplus \langle M \rangle_4 \\ =& \langle scalar \rangle \oplus \left\langle \sigma_1^r, \sigma_1^q, \sigma_2^q, \sigma_3^q \right\rangle \oplus \left\langle \sigma_1^r\sigma_1^q, \sigma_1^r\sigma_2^q, \sigma_1^r\sigma_3^q, \sigma_1^q\sigma_2^q, \sigma_2^q\sigma_3^q, \sigma_3^q\sigma_1^q \right\rangle \\ & \oplus \left\langle \sigma_1^r\sigma_1^q\sigma_2^q, \sigma_2^q\sigma_3^q\sigma_1^r, \sigma_3^q\sigma_1^r\sigma_2^q, \sigma_1^q\sigma_2^q\sigma_3^q \right\rangle \oplus \left\langle \sigma_1^r\sigma_1^q\sigma_2^q\sigma_3^q \right\rangle . \end{aligned}$$

By Definition 2.4, the spinors from $Cl_{0,1,3}(4)$ are extracted as follows

$$Cl^+(4) = \left\langle 1, \sigma_1^r\sigma_1^q, \sigma_1^r\sigma_2^q, \sigma_1^r\sigma_3^q, \sigma_1^q\sigma_2^q, \sigma_2^q\sigma_3^q, \sigma_3^q\sigma_1^q, \sigma_1^r\sigma_1^q\sigma_2^q\sigma_3^q \right\rangle .$$

Any element h in $Cl^+(4)$ can be written as

$$h = 1 + \upsilon_1\sigma_2^q\sigma_3^q + \upsilon_2\sigma_3^q\sigma_1^q + \upsilon_3\sigma_1^q\sigma_2^q + \omega_0\sigma_1^r\sigma_1^q\sigma_2^q\sigma_3^q + \omega_1\sigma_1^r\sigma_1^q + \omega_2\sigma_1^r\sigma_2^q + \omega_3\sigma_1^r\sigma_3^q.$$

Note that the expression above is formed by one scalar, six bivectors and one tetravector giving a total of eight elements. By Definition 2.1, the above expression can be rewritten as

$$\begin{aligned} h =& 1 + \upsilon_1\sigma_2^q\sigma_3^q + \upsilon_2\sigma_3^q\sigma_1^q + \upsilon_3\sigma_1^q\sigma_2^q \\ &+ \left(\sigma_1^r\sigma_1^q\sigma_2^q\sigma_3^q\right)\left[\omega_0 + \omega_1\sigma_2^q\sigma_3^q + \omega_2\sigma_3^q\sigma_1^q + \omega_3\sigma_1^q\sigma_2^q\right]. \end{aligned} \tag{4}$$

In Equation (4) $\upsilon_i, \omega_i \in \mathbb{R}$,

$$\sigma_2^q\sigma_3^q \leftrightarrow i, \quad \sigma_3^q\sigma_1^q \leftrightarrow j, \quad \sigma_1^q\sigma_2^q \leftrightarrow k, \quad \sigma_1^r\sigma_1^q\sigma_2^q\sigma^q \leftrightarrow \varepsilon, \tag{5}$$

then by replacing Equation (5) in Equation (4), namely

$$h = 1 + \upsilon_1 i + \upsilon_2 j + \upsilon_3 k + \varepsilon\left[\omega_0 + \omega_1 i + \omega_2 j + \omega_3 k\right]. \tag{6}$$

Definition 2.5

A DQ, denoted as $\mathbb{H}_2$, is a dual number composed by eight elements $\mathbb{H}_2 \in \mathbb{R}^8$; namely

$$h = \upsilon_0 + \upsilon_1 i + \upsilon_2 j + \upsilon_3 k + \varepsilon(\omega_0 + \omega_1 i + \omega_2 j + \omega_3 k), \tag{7}$$

where υ_i, ω_i are real coefficients, ε represents the dual unit of the number and i, j, k are the unit vector along the x–, y– and z–axis respectively. The elements of $\mathbb{H}_2$ satisfy the properties $i^2 = j^2 = k^2 = ijk = -1$ and $\varepsilon^2 = 0$.

From Equation (6) and Definition 2.5 it is concluded the isomorphism between Clifford algebra and DQ.

2.1.2 Rotation and translation of rigid bodies by dual quaternions

Subsection 2.1.1, starting from the isomorphism with Clifford Algebra, detailed the origin of DQ. Here, DQ is used to rotate and translate rigid bodies. For simplicity, Equation (7) is represented by

$$h^a = \upsilon^a + \varepsilon\omega^a. \tag{8}$$

Equation (8) is used in the following definition.

Definition 2.6

For two given DQ, h^a and h^b, the homogeneous product is computed as

$$\begin{aligned} h^a h^b =& \begin{bmatrix} \upsilon_0^a & -\upsilon_1^a & -\upsilon_2^a & -\upsilon_3^a \\ \upsilon_1^a & \upsilon_0^a & -\upsilon_3^a & \upsilon_2^a \\ \upsilon_2^a & \upsilon_3^a & \upsilon_0^a & -\upsilon_1^a \\ \upsilon_3^a & -\upsilon_2^a & \upsilon_1^a & \upsilon_0^a \end{bmatrix} \begin{bmatrix} \upsilon_0^b \\ \upsilon_1^b i \\ \upsilon_2^b j \\ \upsilon_3^b k \end{bmatrix} \\ &+ \varepsilon \left(\begin{bmatrix} \upsilon_0^a & -\upsilon_1^a & -\upsilon_2^a & -\upsilon_3^a \\ \upsilon_1^a & \upsilon_0^a & -\upsilon_3^a & \upsilon_2^a \\ \upsilon_2^a & \upsilon_3^a & \upsilon_0^a & -\upsilon_1^a \\ \upsilon_3^a & -\upsilon_2^a & \upsilon_1^a & \upsilon_0^a \end{bmatrix} \begin{bmatrix} \omega_0^b \\ \omega_1^b i \\ \omega_2^b j \\ \omega_3^b k \end{bmatrix} + \begin{bmatrix} \omega_0^a & -\omega_1^a & -\omega_2^a & -\omega_3^a \\ \omega_1^a & \omega_0^a & -\omega_3^a & \omega_2^a \\ \omega_2^a & \omega_3^a & \omega_0^a & -\omega_1^a \\ \omega_3^a & -\omega_2^a & \omega_1^a & \omega_0^a \end{bmatrix} \begin{bmatrix} \upsilon_0^b \\ \upsilon_1^b i \\ \upsilon_2^b j \\ \upsilon_3^b k \end{bmatrix} \right). \end{aligned}$$

It is important to highlight that, in general, DQ's product does not satisfy the commutative property.

Definition 2.7

Two conjugation relations are defined for DQ as follows

1. Conjugate of DQ: $h^* = \upsilon_0 - \upsilon_1 i - \upsilon_2 j - \upsilon_3 k + \varepsilon(\omega_0 - \omega_1 i - \omega_2 j - \omega_3 k)$.
2. A dual conjugate of DQ: $\overline{h^*} = \upsilon_0 - \upsilon_1 i - \upsilon_2 j - \upsilon_3 k - \varepsilon(\omega_0 - \omega_1 i - \omega_2 j - \omega_3 k)$.

In the motion of points, lines, and planes, it is necessary to use both DQ conjugations. The following subsection introduces these calculations.

Definition 2.8

A DQ is called unit DQ if $hh^* = 1$*. Then, it satisfies the following pair of conditions*

$$\upsilon_0^2 + \upsilon_1^2 + \upsilon_2^2 + \upsilon_3^2 = 1 \quad \wedge \quad \upsilon_0\omega_0 + \upsilon_1\omega_1 + \upsilon_2\omega_2 + \upsilon_3\omega_3 = 0.$$

The conditions detailed in Definition 2.8 let us visualize a unit hypersphere of three dimensions, and a three-dimensional hyperplane perpendicular to the normal at the point $\upsilon_0, \upsilon_1, \upsilon_2, \upsilon_3$ on the hypersphere. Note that the hyperspace $P\mathbb{R}^3 \subset \mathbb{R}^4$, then a DQ representing a rotation and a translation is defined in $\mathbb{R}^8$. This manifold interpretation is used in the following definition.

Definition 2.9

Let $\Upsilon = \cos\frac{\vartheta}{2} + \hat{u}\sin\frac{\vartheta}{2}$ *be a spinor from* $Cl_{0,0,3}(3)$ *that represents a rotation about a unit vector* $\hat{u}$ *through* ϑ*. Its conjugate is* $\Upsilon^* = \cos\frac{\vartheta}{2} - \hat{u}\sin\frac{\vartheta}{2}$ *such that* $\Upsilon\Upsilon^* = 1$*. Let* $t = (0, t_x i, t_y j, t_z k)$ *be a translation spinor from* $Cl_{0,0,3}(3)$*. Its corresponding conjugate is* $t^* = -t$*. A geometric body* ξ*, under the rotation* Υ *followed by the translation* t *becomes the point* $\Upsilon\xi + t$*. The transformation sequence* Υ, t *can be compacted in the below DQ as follows*

$$\begin{aligned} h =& \Upsilon + \tfrac{\varepsilon}{2} t\Upsilon \\ =& \cos\tfrac{\vartheta}{2} + \hat{u}\sin\tfrac{\vartheta}{2} + \tfrac{\varepsilon}{2}\left(-\sin\tfrac{\vartheta}{2}\left(t\cdot\hat{u}\right) + \cos\tfrac{\vartheta}{2}t + \sin\tfrac{\vartheta}{2}t\times\hat{u}\right). \end{aligned}$$

The following section applies DQ presented in Definition 2.9 to the displacement of points, lines, and planes in the next section.

2.2 MOVEMENT OF POINTS, LINES AND PLANES

This work aims to use DQ to analyze SLE assemblies' kinematics which has a point, a line, or a plane as an end-effector. Therefore, in this subsection, by using the

definitions detailed in the last subsections, the motion of points, lines and planes using DQ is presented.

Proposition 2.1

The DQ presented in Definition 2.9 is a unit DQ.

Proof.

By Definitions 2.8 and 2.9:

$$\begin{aligned} hh^* =& \left(\Upsilon + \tfrac{\varepsilon}{2} t\Upsilon\right)\left(\Upsilon^* + \tfrac{\varepsilon}{2}(t\Upsilon)^*\right) \\ =& \left(\Upsilon + \tfrac{\varepsilon}{2} t\Upsilon\right)\left(\Upsilon^* + \tfrac{\varepsilon}{2}\Upsilon^* t^*\right) \\ =& \Upsilon\Upsilon^* + \tfrac{\varepsilon}{2}\left(\Upsilon\Upsilon^* t^* + t\Upsilon\Upsilon^*\right) \\ =& 1 + \tfrac{\varepsilon}{2}\left(t^* + t\right) \\ =& 1. \end{aligned}$$

Proposition 2.2

For a given point $\mu^p = (0, \mu_x^p i, \mu_y^p j, \mu_z^p k)$ in the hyperspace $P\mathbb{R}^3$, represented in DQ coordinates by $\xi^p = \mathbf{1} + \varepsilon(\mu^p)$, where $\mathbf{1} = (1, 0i, 0j, 0k)$, a rotation Υ and a translation t is represented by ${}'\xi^p = h\xi^p\overline{h^*}$.

Proof.

$$\begin{aligned} {}'\xi^p =& 1 + \varepsilon\left(\Upsilon\xi^p\Upsilon^* + t\right) \\ =& 1 + \varepsilon\left(\Upsilon\xi^p\Upsilon^*\right) + \varepsilon t \\ =& 1 + \varepsilon\left(\Upsilon\xi^p\Upsilon^*\right) + \varepsilon\tfrac{t}{2} + \varepsilon\tfrac{t}{2} \\ =& 1 + \varepsilon\left(\Upsilon\xi^p\Upsilon^*\right) + \varepsilon\tfrac{t}{2} - \varepsilon\tfrac{t^*}{2} \\ =& \left(\Upsilon + \varepsilon\tfrac{t}{2}\Upsilon\right)\left(1 + \varepsilon\xi^p\right)\overline{\left(\Upsilon^* - \varepsilon\Upsilon^*\tfrac{t^*}{2}\right)} \\ =& \left(\Upsilon + \varepsilon\tfrac{t}{2}\Upsilon\right)\left(1 + \varepsilon\xi^p\right)\overline{\left(\Upsilon^* + \varepsilon\Upsilon^*\tfrac{t^*}{2}\right)} \\ =& \left(\Upsilon + \varepsilon\tfrac{t}{2}\Upsilon\right)\left(1 + \varepsilon\xi^p\right)\overline{\left(\Upsilon + \varepsilon\tfrac{t}{2}\Upsilon\right)}^* \\ =& h\xi^p\overline{h^*}. \end{aligned}$$

Proposition 2.3

A line in DQ coordinates can be represented by $\xi^L = l + \varepsilon m$, where $l = (0, l_x i, l_y j, l_z k)$ is the vector displacement of the line in the hyperspace $P\mathbb{R}^3$, $m = (0, m')$ with $m' = l \times l_0$ is the moment of the line where l_0 is the position vector of any arbitrary point in the line. Then, a rotation followed by a line translation is computed as ${}'\xi^L = h\xi^L h^*$.

Proof.

The rotation, in this case, affects to the vector displacement $\Upsilon l \Upsilon^*$ as well the moment $\Upsilon m \Upsilon^*$. On the other hand, the translation only affects to the moment through $t \times (\Upsilon l \Upsilon^*)$.

$$\begin{aligned}
{}'\xi^L &= \Upsilon l \Upsilon^* + \varepsilon \left[\Upsilon m \Upsilon^* + t \times (\Upsilon l \Upsilon^*)\right] \\
&= \Upsilon l \Upsilon^* + \varepsilon(\Upsilon m \Upsilon^*) + \varepsilon \left[\frac{t(\Upsilon l \Upsilon^*) - (\Upsilon l \Upsilon^*)t}{2}\right] \\
&= \Upsilon l \Upsilon^* + \varepsilon(\Upsilon m \Upsilon^*) + \varepsilon \frac{t}{2}(\Upsilon l \Upsilon^*) - \varepsilon(\Upsilon l \Upsilon^*)\frac{t}{2} \\
&= \left(\Upsilon + \varepsilon \frac{t}{2}\Upsilon\right)(1 + \varepsilon m)\left(\Upsilon^* + \varepsilon \Upsilon^* \frac{t^*}{2}\right) \\
&= \left(\Upsilon + \varepsilon \frac{t}{2}\Upsilon\right)(1 + \varepsilon m)\left(\Upsilon + \varepsilon \frac{t}{2}\Upsilon\right)^* \\
&= h \xi^L h^*.
\end{aligned}$$

Note that the DQ coordinates' line representation is based on *Plücker* coordinates (FEATHERSTONE, R., 2007; RADAVELLI, L., 2012).

Proposition 2.4

The rotation and translation of a plane, represented in DQ coordinates as $\xi^N = n - \epsilon d$*, where* $n = (0, n_x i, n_y j, n_z k)$ *is the normal vector represented in the hyperspace* $P\mathbb{R}^3$ *and* $d = (d', 0, 0, 0)$ *where* d' *is the distance of the plane from the origin, is given by* ${}'\xi^N = h \xi^N h^*$*.*

Proof.

The rotation of a plane affects the orientation of the normal vector $\Upsilon n \Upsilon^*$, while the translation affects the distance of the plane from the origin; however, it is necessary to consider the projection of the translation over the normal vector $d + t \cdot (\Upsilon n \Upsilon^*)$.

$$\begin{aligned}
{}'\xi^N &= \Upsilon n \Upsilon^* - \varepsilon \left[d + t \cdot (\Upsilon n \Upsilon^*)\right] \\
&= \Upsilon n \Upsilon^* - \varepsilon d + \varepsilon \left[\frac{t(\Upsilon n \Upsilon^*) + (\Upsilon n \Upsilon^*)t}{2}\right] \\
&= \Upsilon n \Upsilon^* - \varepsilon d + \varepsilon \frac{t}{2}(\Upsilon n \Upsilon^*) + \varepsilon(\Upsilon n \Upsilon^*)\frac{t}{2} \\
&= \left(\Upsilon + \varepsilon \frac{t}{2}\Upsilon\right)(n - \varepsilon d)\left(\Upsilon^* - \varepsilon \Upsilon^* \frac{t^*}{2}\right) \\
&= \left(\Upsilon + \varepsilon \frac{t}{2}\Upsilon\right)(n - \varepsilon d)\overline{\left(\Upsilon^* + \varepsilon \Upsilon^* \frac{t^*}{2}\right)} \\
&= \left(\Upsilon + \varepsilon \frac{t}{2}\Upsilon\right)(n - \varepsilon d)\overline{\left(\Upsilon + \varepsilon \frac{t}{2}\Upsilon\right)}^* \\
&= h \xi^N \overline{h^*}.
\end{aligned}$$

Note that in Propositions 2.2, 2.3, and 2.4, DQ's conjugate is used in the motion of lines; while, DQ's dual conjugate is used in the motion of points and planes. The definitions and propositions presented in this section will be used in SLE structures' kinematic analysis in the next section.

2.3 APPLICATION OF DQ IN SLE

There are translational SLE with the possibility to translate along a straight trajectory in one or more axis. Also, there are polar SLE that, in addition to translation, can rotate through a fixed axis to describe curvilinear trajectories. Moreover, three-dimensional folding structures can be assembled by using connectors. In practical applications, it is possible to find, besides a point, a line or a plane as an end-effector in SLE structures. Thus, by taking advantage of the DQ properties, this section introduces an approach to deal with kinematic analysis of complex homogeneous and heterogeneous assemblies of SLE.

Definition 2.10

An SLE unit, also known as pantograph, is a composition of two bars connected at an intermediate point through a revolute joint called pivot which allows them to rotate freely about an axis perpendicular to their common plane but constrains all other degrees of freedom. The end points of these bars can be hinged to the next SLE unit. These joints are called hinges depicted in Figure 11. Also, the geometrical parameters of a standard SLE are shown in Figure 11.

Figure 11 – Parts and geometrical parameters of an standard SLE.

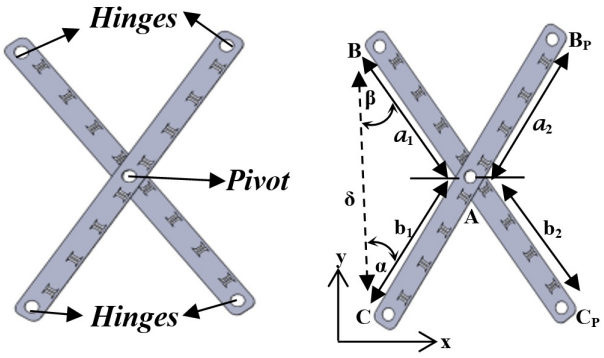

Source – From the author.

2.3.1 Representation of translational SLE by DQ

There are two types of translational SLE (AKGUN, Y., 2010): the first type with equal bar lengths and the second type with different bar lengths.

2.3.1.1 Translational SLE with constant bar lengths: type 1

This type of folding structures can only translate without any rotation. When all bars have the same lengths $a_1 = a_2 = b_1 = b_2 = a_l$, and the pivots are located in the

middle of the bars, these assemblies describe a straight translation. Definitions 2.9 and 2.10 are employed to describe the kinematic relation of a point in the pivot or the hinges from the origin frame C through a translation spinor $t_I = (0, t_x i, t_y j, 0k)$ as follows.

- From the origin C to the pivot A: $h_{IA} = 1 + \varepsilon t_I$, with $t_x = \frac{\sqrt{4a_I^2 - \delta^2}}{4}$ and $t_y = \frac{\delta}{4}$.
- From the origin C to the upper hinge B_P: $h_{IB_P} = 1 + \varepsilon t_I$, with $t_x = \frac{\sqrt{4a_I^2 - \delta^2}}{2}$ and $t_y = \frac{\delta}{2}$.
- From the origin C to the lower hinge C_P: $h_{IC_P} = 1 + \varepsilon t_I$, with $t_x = \frac{\sqrt{4a_I^2 - \delta^2}}{2}$ and $t_y = 0$.

Note that the input parameters are the SLE aperture δ and the length of the bar a_I. In extensive SLE assemblies, the most used DQ, among the DQ defined above, is the h_{IC_P}. It happens because the hinge C_P of the i SLE is linked with the hinge C of the $i+1$ SLE, leading into uniform displacement of the frame origin, as seen in the following example. Since the multiplication of quaternions is bidirectional, the translations and rotations are half.

Example 2.1

Consider the SLE structure in Figure 12, the kinematic relation of a point ξ^P in $A_3, A_4, B_{P3}, B_{P4}, C_{P4}$, from the origin C is given by

$$
\begin{aligned}
{}^{A_3}_{C}\xi^P &= h_{IC_P} h_{IC_P} h_{IA} \xi^P \overline{h^*_{IA} h^*_{IC_P} h^*_{IC_P}} \\
{}^{A_4}_{C}\xi^P &= h_{IC_P} h_{IC_P} h_{IC_P} h_{IA} \xi^P \overline{h^*_{IA} h^*_{IC_P} h^*_{IC_P} h^*_{IC_P}} \\
{}^{B_{P3}}_{C}\xi^P &= h_{IC_P} h_{IC_P} h_{IB_P} \xi^P \overline{h^*_{IB_P} h^*_{IC_P} h^*_{IC_P}} \\
{}^{B_{P4}}_{C}\xi^P &= h_{IC_P} h_{IC_P} h_{IC_P} h_{IB_P} \xi^P \overline{h^*_{IB_P} h^*_{IC_P} h^*_{IC_P} h^*_{IC_P}} \\
{}^{C_{P4}}_{C}\xi^P &= h_{IC_P} h_{IC_P} h_{IC_P} h_{IC_P} \xi^P \overline{h^*_{IC_P} h^*_{IC_P} h^*_{IC_P} h^*_{IC_P}}.
\end{aligned}
$$

The relations above come from Proposition 2.2. Also, it is possible to verify that the most used DQ is h_{IC_P} and its dual conjugate. Therefore it is considered necessary to introduce DQ exponentiation for homogeneous DQ in the following point.

DQ exponentiation of translational SLE type1

By using Definition 2.6, if a point $\xi^P = 1 + \varepsilon 0$ is affected by homogeneous motions represented by h_{IC_P} then

$$
\left[{}'\xi_I^P\right]^n = \left[h_{IC_P}\right]^n \xi^P \left[\overline{h^*_{IC_P}}\right]^n = [1 + \varepsilon(n\sqrt{4a_I^2 - \delta^2} i + 0j + 0k)]
$$

where n is the number of SLE.

Figure 12 – Folding structure composed by 4 translational SLE with constant bar lenght.

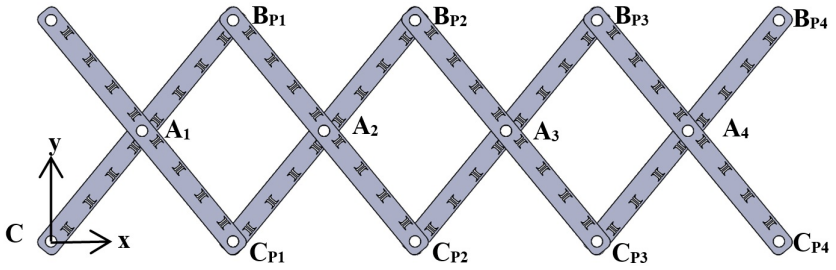

Source – From the author.

In Example 2.1 the relation ${}^{C_{P4}}_{C}\xi^{P}$ can be rewritten as $[{}^{C_{P4}}_{C}\xi^{P}_{I}]^4$, thus reducing the computational effort (GRIJALVA, J., 2019). DQ exponentiation can be proven here and in the sequel by using Definition 2.6 and Proposition 2.2 as follows

$$\begin{aligned}
\left[{}'\xi^{P}_{I}\right]^1 &= \left[h_{IC_P}\right]^1 \xi^{P} \left[\overline{h^{*}_{IC_P}}\right]^1 = \quad [1+\varepsilon(\sqrt{4a_I^2-\delta^2}i+0j+0k)] \\
\left[{}'\xi^{P}_{I}\right]^2 &= \left[h_{IC_P}\right]^2 \xi^{P} \left[\overline{h^{*}_{IC_P}}\right]^2 = \quad [1+\varepsilon(2\sqrt{4a_I^2-\delta^2}i+0j+0k)] \\
\left[{}'\xi^{P}_{I}\right]^3 &= \left[h_{IC_P}\right]^3 \xi^{P} \left[\overline{h^{*}_{IC_P}}\right]^3 = \quad [1+\varepsilon(3\sqrt{4a_I^2-\delta^2}i+0j+0k)] \\
&\vdots \qquad\qquad \vdots \qquad\qquad\qquad \vdots \\
\left[{}'\xi^{P}_{I}\right]^n &= \left[h_{IC_P}\right]^n \xi^{P} \left[\overline{h^{*}_{IC_P}}\right]^n = \quad [1+\varepsilon(n\sqrt{4a_I^2-\delta^2}i+0j+0k)].
\end{aligned}$$

2.3.1.2 Translational SLE with different bar lengths: type 2

This kind of SLE can only translate without any rotation,similar to the previous case. Bar lengths are $a_1 = b_2 = a_Y$ and $b_1 = a_2 = b_Y$. These assemblies describe an inclined translation. Definitions 2.9 and 2.10 are used to describe the kinematic relation of a point in the pivot or the hinges from the origin frame C through a translation spinor $t_Y = (0, t_x i, t_y j, 0k)$ as follows.

- From the origin C to the pivot A: $h_{YA} = 1 + \varepsilon t_Y$, with $t_x = \frac{b_Y \cos\tau_Y}{2}$ and $t_y = \frac{b_Y \sin\tau_Y}{2}$ where $\tau_Y = \frac{\pi}{2} - \alpha_Y$; $\alpha_Y = \arccos\left(\frac{\delta^2+b_Y^2-a_Y^2}{2\delta b_Y}\right)$.
- From the origin C to the upper hinge B_P: $h_{YB_P} = 1 + \varepsilon t_Y$, with $t_x = \frac{(a_Y+b_Y)\cos\tau_Y}{2}$ and $t_y = \frac{(a_Y+b_Y)\sin\tau_Y}{2}$; τ_Y, α_Y defined above.
- From the origin C to the lower hinge C_P: $h_{YC_P} = 1+\varepsilon t_Y$, where $t_x = \frac{b_Y \sin\alpha_Y + a_Y \sin\beta_Y}{2}$ and $t_y = \frac{b_Y\cos\alpha_Y - a_Y\cos\beta_Y}{2}$ with $\beta_Y = \arccos\left(\frac{\delta^2-b_Y^2+a_Y^2}{2\delta a_Y}\right)$; α_Y defined above.

Note that the input parameters are the SLE aperture δ and the lengths of the bars a_Y, b_Y. The DQ presented in this subsection is employed in the next example.

Example 2.2

In the SLE assembly in Figure 13, the kinematic relation of a point ξ^P inA_3, B_{P2}, C_{P2}, from the origin C is given by

$$\begin{aligned}
{}^{A_3}_{C}\xi^P &= h_{YC_P} h_{YC_P} h_{YA} \xi^P \overline{h^*_{YA} h^*_{YC_P} h^*_{YC_P}} \\
{}^{B_{P2}}_{C}\xi^P &= h_{YC_P} h_{YB_P} \xi^P \overline{h^*_{YB_P} h^*_{YC_P}} \\
{}^{C_{P2}}_{C}\xi^P &= h_{YC_P} h_{YC_P} \xi^P \overline{h^*_{YC_P} h^*_{YC_P}}.
\end{aligned}$$

Figure 13 – Folding structure composed by 3 translational SLE with different bar lenght.

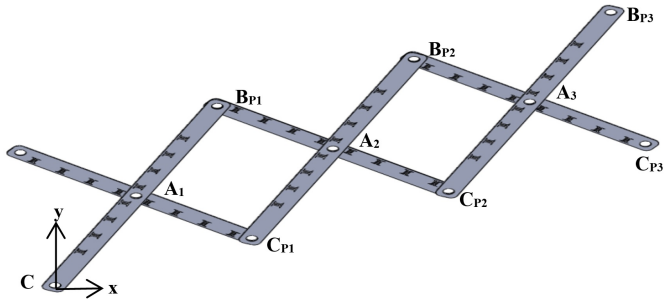

Source – From the author.

Like the last case, DQ exponentiation for this type of SLE is presented in the following point.

DQ exponentiation of translational SLE type 2

Homogeneous displacements represented by h_{YC_P} in a point $\xi^P = 1 + \varepsilon 0$ can be defined through DQ exponentiation as

$$\begin{aligned}
\left[{}'\xi^P_Y\right]^n &= \left[h_{YC_P}\right]^n \xi^P \left[\overline{h^*_{YC_P}}\right]^n \\
&= [1 + \varepsilon(n(b_Y \sin\alpha_Y + a_Y \sin\beta_Y)i + n(b_Y \cos\alpha_Y - a_Y \cos\beta_Y)j + 0k)],
\end{aligned}$$

where n is the number of SLE. In the Example 2.2 the relation ${}^{C_{P2}}_{C}\xi^P$ can be rewritten as $[{}^{C_{P2}}_{C}\xi^P_Y]^2$.

2.3.2 Representation of polar SLE by DQ

The main characteristic of these structures is to deploy and contract as a part of a single arc. Besides of translation, there exists a rotation by this type of SLE. The lengths of the bars are $a_1 = a_2 = a_S$ and $b_1 = b_2 = b_S$. Definitions 2.9 and 2.10 are used to describe the kinematic relation of a point in the pivot or the hinges from the origin frame C through a rotation spinor $\Upsilon_S = \cos\frac{\vartheta}{2} + \hat{u}\sin\frac{\vartheta}{2}$ and a translation spinor $t_S = (0, t_x i, t_y j, 0k)$ as follows.

- From the origin to the pivot A: $h_{SA} = 1 + \varepsilon t_S$, with $t_x = \frac{b_S \cos\tau_S}{2}$ and $t_y = \frac{b_S \sin\tau_S}{2}$ where $\tau_S = \frac{\pi}{2} - \alpha_S$; $\alpha_S = \arccos\left(\frac{\delta^2 + b_S^2 - a_S^2}{2\delta b_S}\right)$.
- From the origin C to the upper hinge B_P: $h_{SB_P} = 1 + \varepsilon t_S$, with $t_x = \frac{(a_S + b_S)\cos\tau_S}{2}$ and $t_y = \frac{(a_S + b_S)\sin\tau_S}{2}$; τ_S, α_S defined above.
- From C to the lower hinge C_P: $h_{SC_P} = \Upsilon_S + \varepsilon t_S$, where $t_x = \frac{b_S \sin\alpha_S + b_S \sin\beta_S}{2}$ and $t_y = \frac{b_S \cos\beta_S - a_S \cos\alpha_S}{2}$ with $\beta_S = \arccos\left(\frac{\delta^2 - b_S^2 + a_S^2}{2\delta a_S}\right)$; ; $\hat{u} = (0i + 0j + k)$; $\vartheta = -\arctan\left(\frac{(a_S - b_S)\sin\frac{\alpha_S + \beta_S}{2}}{(a_S + b_S)\cos\frac{\alpha_S + \beta_S}{2}}\right)$; α_S defined above.

Note that the input parameters are the SLE aperture δ and the lengths of the bars a_S, b_S. In the following example, the DQ presented in this subsection is applied.

Example 2.3

The kinematic relation of a point ξ^P in the positions A_2, B_{P2}, C_{P3}, in Figure 14 from the origin C is expressed as

$$
\begin{aligned}
{}^{A_2}_{C}\xi^P &= h_{SC_P} h_{SA} \xi^P \overline{h^*_{SA} h^*_{SC_P}} \\
{}^{B_{P2}}_{C}\xi^P &= h_{SC_P} h_{SB_P} \xi^P \overline{h^*_{SB_P} h^*_{SC_P}} \\
{}^{C_{P3}}_{C}\xi^P &= h_{SC_P} h_{SC_P} h_{SC_P} \xi^P \overline{h^*_{SC_P} h^*_{SC_P} h^*_{SC_P}}.
\end{aligned}
$$

It is important to highlight that the expression above can be employed to displace lines and planes too, being just necessary to replace ξ^L, ξ^N instead of ξ^P.

Figure 14 – Folding structure composed by 3 polar SLE.

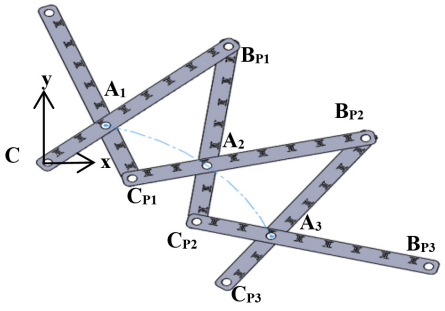

Source – From the author.

In the homogeneous displacements such as ${}^{C_{P3}}_{C}\xi^P$ in Example 2.3, based on Definition 2.6, DQ exponentiation can be used as follows.

DQ exponentiation of polar SLE

Homogeneous displacements represented by h_{SC_P} in a point $\xi^P = 1 + \varepsilon 0$ can be defined through DQ exponentiation as

$$\begin{aligned}\left[{}'_S\xi^P\right]^n &= \left[h_{SC_P}\right]^n \xi^P \left[\overline{h^*_{SC_P}}\right]^n \\ &= [1 + \varepsilon(n\left(\sigma_2\sigma_5 - \sigma_1\sigma_6 + \sigma_4\cos\tfrac{\vartheta}{2} - \sigma_3\sin\tfrac{\vartheta}{2}\right) i \\ &\quad + n\left(\sigma_1\sigma_5 + \sigma_2\sigma_6 + \sigma_3\cos\tfrac{\vartheta}{2} + \sigma_4\sin\tfrac{\vartheta}{2}\right) j + 0k)],\end{aligned}$$

where

$$\begin{aligned}&\sigma_1 = \frac{t_y\cos\frac{\vartheta}{2}}{2} - \frac{t_x\sin\frac{\vartheta}{2}}{2}, \quad \sigma_2 = \frac{t_x\cos\frac{\vartheta}{2}}{2} + \frac{t_y\sin\frac{\vartheta}{2}}{2}, \quad \sigma_3 = \frac{\sigma_5 t_y}{2} - \frac{\sigma_6 t_x}{2}, \quad \sigma_4 = \frac{\sigma_5 t_x}{2} - \frac{\sigma_6 t_y}{2}, \\ &\sigma_5 = \cos\frac{\vartheta}{2}, \quad \sigma_6 = \sin\frac{\vartheta}{2}.\end{aligned}$$

The parameters t_x and t_y correspond to the DQ h_{SCP}, which relates the lower hinge from the origin. Note that in Example 2.3 the expression ${}^{C_{P3}}_{C}\xi^P$ can be replaced by $\left[{}^{C_{P3}}_{C}\xi^P\right]^3$.

2.3.3 Representation of connectors by DQ

The use of connectors in three-dimensional SLE structures is quite common. However, these connectors' kinematic impact is generally small, being sometimes ignored or considered ideal. It means that the translation that produces these connectors is considered null, i.e, the folding roof presented in (GRIJALVA, J., 2019). Thereby, aiming for accuracy, a DQ representation of a connector is introduced in this subsection, taking into account the rotation and translation that it causes in the assembly.

Figure 15 – Connector of SLE and description of its geometrical parameters.

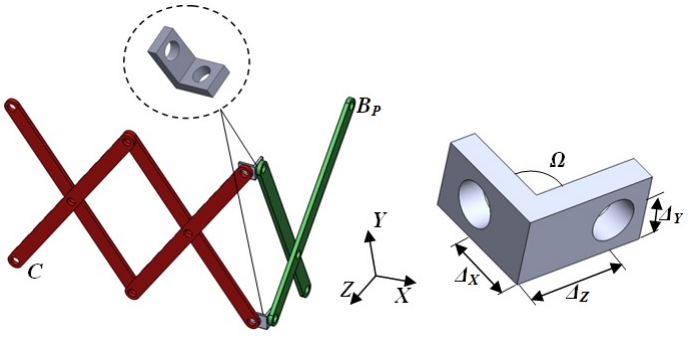

Source – From the author.

Figure 15 depicts a connector with *L*-shape. The parameters are $\Delta_X, \Delta_Y, \Delta_Z$ that represent translations in *x*–, *y*–, *z*–axis respectively, and $\Omega, 0 < \Omega < \pi$ is the angle between the connector beams. The above-mentioned parameters can be embedded in a DQ

through translation and rotation spinors $t_L = (0, \Delta_X, \Delta_Y, -\Delta_Z)$, $\Upsilon_L = \cos\frac{\pi-\Omega}{2} + \hat{u}\sin\frac{\pi-\Omega}{2}$ with $\hat{u} = (0, \pm 1, 0)$. The symbol $\pm$ in $\hat{u}$ is going to depend of the desired rotation according to right-hand rule. Thus, $h_L = \Upsilon_L + \frac{\varepsilon}{2} t_L \Upsilon_L$. In Figure 15, a structure is shown composed of two translational SLE with constant bar (in red) and one polar SLE (in green), both assemblies linked by a connector. Then, the kinematic relation of a point ${}^{P}\xi$ in B_P from the origin C is given by

$$ {}^{B_P}_{C}\xi^{P} = h_{IC_P} h_{IC_P} h_L h_{SB_P} \, {}^{P}\xi \, \overline{h^*_{SB_P} h^*_L h^*_{IC_P} h^*_{IC_P}}. $$

2.3.4 Analysis of singularities in SLE

Deployable structures, including SLE, usually deal with singularities. These singularities can cause a change of mobility. Previously to compute the reachable workspace of a folding structure, it is indispensable to identify the singularity points in the mechanism's path. Thus, in this subsection Algorithm 1 is introduced, based on the theory mentioned above, to identify singularities in SLE assemblies.

Algorithm 1 Algorithm for detection of singularities in SLE

1: **procedure** PARAMETERS DESCRIPTION
2: Define the dimensions of the SLE bars
3: Compute $\delta_{MAX} = a_1 + b_1$ ▷ Based on Figure 11
4: Determine the kinematic relation ${}^{CP}_{C}\xi$
5: Choose the searching increment (S_{bty}) ▷ Searching accuracy
6: **procedure** SEARCHING LOOP
7: $aux_1 = 100 : -S_{bty} : 0$ ▷ Vector from 100 to 0 with $-S_{bty}$ increment
8: $n = size(aux_1)$ ▷ Number of elements in vector aux_1
9: $\delta_{[n]} = \delta_{MAX} \times 0.01 \times aux_1$ ▷ Vector with n possible values of δ
10: **for** $i = 1$ **to** n **do**
11: ${}^{CP}_{C}\xi_{[i]}(\delta_i)$ ▷ Calculate ${}^{CP}_{C}\xi$ for each interaction
12: $t_{[i]} = (0, t_{x[i]}, t_{y[i]}, t_{z[i]})$ ▷ Extract the translation spinor
13: **if** $t_{x[i]}, t_{y[i]}, t_{z[i]} \notin \mathbb{R}$ **then**
14: Break ▷ Stop the loop
15: $\delta_{BIF} = \delta_{[i]}$ ▷ Value of δ at singularity time

2.3.5 Analysis of workspace in SLE

Analogously to serial robots, SLE structures usually have a end-effector, then it is necessary to know the dexterous or reachable workspace of SLE mechanisms. The singularity analysis is essential because it is possible to know the limit of the input δ. Therefore, the first step of this approach is to apply Algorithm 1 to compute δ_{BIF}. Some SLE assemblies are free of singularities. If this is the case, then Algorithm 1 must be omitted. Algorithm 2 details the steps to calculate and plot the reachable workspace of an SLE structure. If it is desired to compute the dexterous workspace, then in line 7 of

the Algorithm 2 it is necessary to replace ℓ by $\ell = 100 \times \delta_{arb}/\delta_{MAX}$ where δ_{arb} is an arbitrary value of $\delta_{arb}, \delta_{MAX} > \delta_{arb} > \delta_{BIF} > 0$.

Algorithm 2 Algorithm for computation and plotting of workspace in SLE

procedure PARAMETERS DESCRIPTION(Geometry-dimensions)
    Define the dimensions of the SLE bars
    Compute $\delta_{MAX} = a_1 + b_1$ ▷ Based on Figure 11
    Determine the kinematic relation ${}^{CP}_{C}\xi^{P,L,N}$
    Choose the increment (S_{bty}) ▷ Plotting accuracy
procedure WORKSPACE COMPUTATION LOOP
    $aux_1 = 100 : -S_{bty} : \ell$ ▷ Vector from 100 to $\ell = 100 \times \delta_{BIF}/\delta_{MAX}$ with $-S_{bty}$ increment
    $n = size(aux_1)$ ▷ Number of elements in vector aux_1
    $\delta_{[n]} = \delta_{MAX} \times 0.01 \times aux_1$ ▷ Vector with n possible values of δ
    for $i = 1$ **to** n **do**
        ${}^{CP}_{C}\xi_{[i]}(\delta_i)$ ▷ Calculate ${}^{CP}_{C}\xi$ for each interaction
        $t_{[i]} = (0, t_{x[i]}, t_{y[i]}, t_{z[i]})$ ▷ Extract the translation spinor
        $\Upsilon_{[i]} = \cos\frac{\vartheta_{[i]}}{2} + \hat{u}\sin\frac{\vartheta_{[i]}}{2}$ ▷ Extract the rotation spinor
        Plot the orientation of the point, line or plane $\xi^{P}_{[i]}, \xi^{L}_{[i]}, \xi^{N}_{[i]}$

2.4 NUMERICAL AND PRACTICAL EXAMPLES

This section uses all the theory presented above in applications based on domotics. In these applications, the general folding condition was considered, which can be found in Appendix A, in the synthesis of the SLE mechanisms introduced in this section. The first example is a retractable lamp. The chosen end-effector is a line that emulates the central beam of a light bulb. The second example is a folding furniture for displays like televisions or digital photo frames, which will be represented like a plane to verify the DQ advantage of orientating points, lines and planes.

2.4.1 Retractable lamp

The folding structure shown in Figure 16 can be employed to assemble a lamp used over a table, in the corner of a lounge, or on the streets to illuminate a public place. The lamp presented below will be used like a hall lamp, and the central beam of light is represented as a line ξ^{L}. The proposed assembly is presented in Figure 16. The structure is composed of two translational SLE with constant bar length (in red), two translational SLE with different bar length (in blue), and three polar SLE (in green). To plot the reachable workspace, the kinematic relations of the points are defined below

$A_1, B_{P1}, C_{P1}, C_{P2}$ from the origin C.

$$
\begin{aligned}
{}^{A_1}_{C}\xi^{P} &= h_{IC_P}h_{IC_P}h_{YC_P}h_{YC_P}h_{SC_P}h_{SC_P}h_{SA}\xi^{P}\overline{h^*_{SA}h^*_{SC_P}h^*_{SC_P}h^*_{YC_P}h^*_{YC_P}h^*_{IC_P}h^*_{IC_P}} \\
{}^{B_{P1}}_{C}\xi^{P} &= h_{IC_P}h_{IC_P}h_{YC_P}h_{YC_P}h_{SC_P}h_{SC_P}h_{SB_P}\xi^{P}\overline{h^*_{SB_P}h^*_{SC_P}h^*_{SC_P}h^*_{YC_P}h^*_{YC_P}h^*_{IC_P}h^*_{IC_P}} \\
{}^{C_{P1}}_{C}\xi^{P} &= h_{IC_P}h_{IC_P}\xi^{P}\overline{h^*_{IC_P}h^*_{IC_P}} = \left[{}^{C_{P1}}_{C}\xi^{P}_{I}\right]^2 \\
{}^{C_{P2}}_{C}\xi^{P} &= h_{IC_P}h_{IC_P}h_{YC_P}h_{YC_P}\xi^{P}\overline{h^*_{YC_P}h^*_{YC_P}h^*_{IC_P}h^*_{IC_P}}.
\end{aligned}
$$

Figure 16 – Retractable lamp a) folding state b) with lamp c) collisioned.

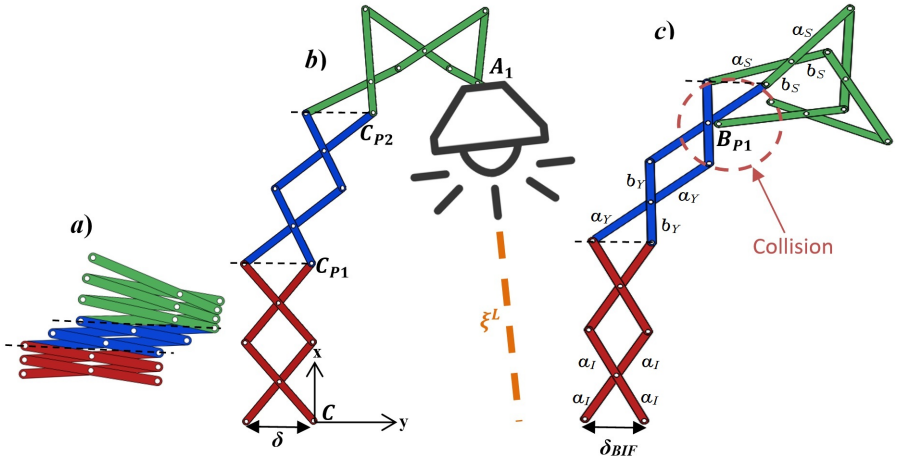

Source – From the author.

The geometric dimensions of the SLE structure in Figure 16 are detailed in Table 1.

Figure 17 – Reachable workspace of points $A_1, B_{P1}, C_{P1}, C_{P2}$.

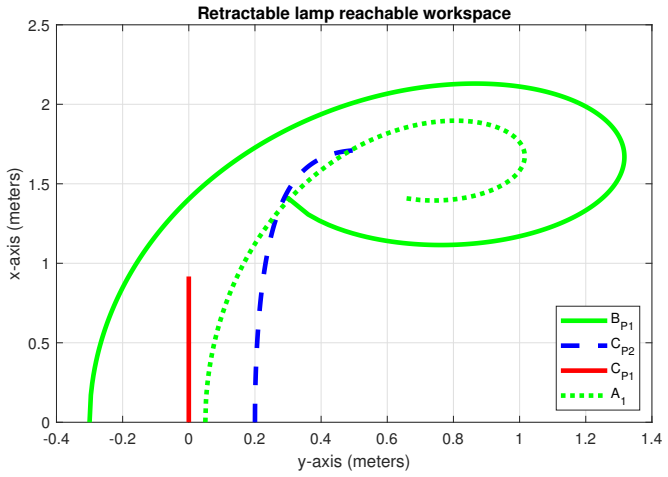

Source – From the author.

Table 1 – Bar length dimensions of Figures 16 and 19.

	a_I	a_Y	b_Y	a_S	b_S
Bar length [meters]	0.25	0.3	0.2	0.35	0.15

Source – From the author.

In Figure 17, by using Algorithm 2, it is depicted the reachable workspace of aforementioned points. In Figure 17 the axis are orientated according to Figure 16.b. The collision between the bars of the structure is highlighted in Figure 16.c , when $\delta = \delta_{BIF}$, leading to the lost of mobility. Using the numerical values shown in Table 1 and the Algorithm 1, $\delta_{BIF} = 0.19$ m is calculated, which means that the reachable workspace is computed for $0.5 > \delta > 0.19$ m. The kinematic relation for the line ξ^L depicted in Figure 16.b. is defined as follows

$$\overset{A_1}{C}\xi^L = h_{IC_P}h_{IC_P}h_{YC_P}h_{YC_P}h_{SC_P}h_{SC_P}h_{SA}\xi^L h^*_{SA}h^*_{SC_P}h^*_{SC_P}h^*_{YC_P}h^*_{YC_P}h^*_{IC_P}h^*_{IC_P}.$$

In the expression above, the line ξ^L has a vector displacement $l^{'} = (1.5i, 0j, 0k)$ and a moment $m^{'} = 0$. Because of Proposition 2.2, note that the above kinematic relation employs DQ's conjugation instead of DQ's dual conjugation. By using $\overset{A_1}{C}\xi^L$, in Figure 18 it is plotted the lines orientation, that represent the lamp light beam, for $\delta = 0.202, 0.23, 0.29, 0.36, 0.45, 0.5$. Let interpret a numerical example, for $\delta = 0.45$ m the value of $\overset{A_1}{C}\xi^L$ is

$$\overset{A_1}{C}\xi^L = [0 + 1.37i - 0.62j + 0k + \varepsilon(0 + 0i + 0j - 0.4461k)]. \tag{9}$$

Figure 18 – Orientation of the light beam represented by a line on the x-y frame.

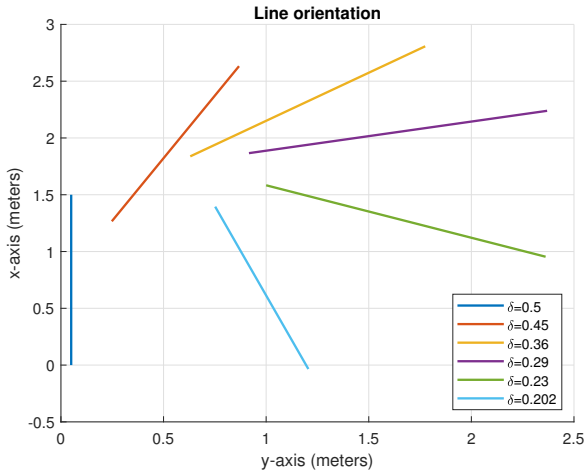

Source – From the author.

From Equation (9), the displacement vector $l' = (1.37i - 0.62j + 0k)$ and the moment $m' = (0i + 0j - 0.4461k)$ are extracted; using $l_0 = l' \times m'$, $l_0 = (0.2765i + 0.6094j + 0k)$ is computed being an arbitrary point over the line. If it is desired to orientate the line segment as depicted in Figure 18, then $l' = P_F - P_S$ can be used, where, P_F is the final point and P_S is the starting point of any segment line. Using ${}^{A_1}_{C}\xi^P$, the starting point can be extracted, then the value of l' can be extracted from ${}^{A_1}_{C}\xi^L$.

2.4.2 Folding furniture for displays

Each year the size of televisions increases while the area of the rooms decreases. One possible solution to this contradiction is to fix the display on the wall. The main drawback is that the display can not be inclined. The furniture presented in this subsection was designed to be fixed on the roof of a room (as seen in Figure 19.a) with the possibility to regulate its inclination. In this example, it is intended to apply the orientation of planes emulating flat displays, as well as the use of connector to create a three-dimensional structure. The structure is composed of one translational SLE with constant bar length (in red), one connector (as shown in Figure 19.b), one translational SLE with different bar lengths(in blue), and two polar SLE (in green).

Figure 19 – Folding furniture for flat displays a) deploying condition b) singularity c) side view d) front view.

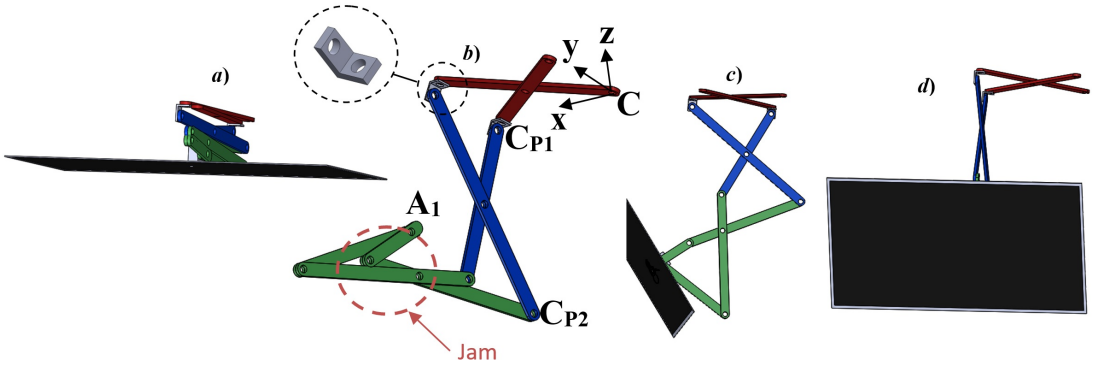

Source – From the author.

The kinematic relations of the points A_1, C_{P1}, C_{P2} from the origin frame C can be written as follows

$$\begin{aligned} {}^{A_1}_{C}\xi^P &= h_{IC_P} h_L h_{YC_P} h_{SC_P} h_{SA} \xi^P \overline{h^*_{SA} h^*_{SC_P} h^*_{YC_P} h^*_L h^*_{IC_P}} \\ {}^{C_{P1}}_{C}\xi^P &= h_{IC_P} \xi^P \overline{h^*_{IC_P}} \\ {}^{C_{P2}}_{C}\xi^P &= h_{IC_P} h_L h_{YC_P} \xi^P \overline{h^*_{YC_P} h^*_L h^*_{IC_P}}. \end{aligned} \tag{10}$$

The connector h_L in Equation (10) has $\Omega = \pi/2$ and $\Delta_X = 0.5, \Delta_Z = -1$ cm according to Figure 15. Using Algorithm 1 the value of δ at singularity time was computed as

δ_{BIF} = 0.2 m. This time the singularity was also caused by a collision as depicted in Figure 19.b. The dimensions of the bars are depicted in Table 1.

Figure 20 – Reachable workspace: points A_1, C_{P1}, C_{P2} in Figure 19.

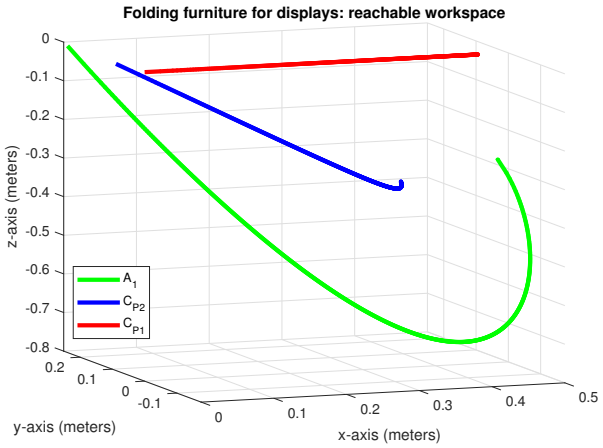

Source – From the author.

In Figure 20, by using Algorithm 2, it is plotted the reachable workspace of the arbitrary chosen points A_1, C_{P1}, C_{P2} according to Figure 19.b. Because of the connector Figure 20 becomes three-dimensional. Now, it is assumed that there is a television display fixed in the point A_1. Based on Proposition 2.4 the plane of the display can be represented by $\xi^N = n - \varepsilon d$, where $n = (0, i, 0j, 0k)$ and $d = 0$ at the origin. The kinematic relation of the plane from the origin is given by

$$\overset{A_1}{C}\xi^N = h_{IC_P} h_L h_{YC_P} h_{SC_P} h_{SA} \xi^N \overline{h^*_{SA} h^*_{SC_P} h^*_{YC_P} h^*_L h^*_{IC_P}}. \tag{11}$$

Note that in Equation (11) it is employed the dual conjugation according to Proposition 2.4. In Figure 21, the orientation of planes is plotted according to various values given to δ. Let interpret one of the plotted results, in the case of δ = 0.43 m the orientation of the plane was

$$\overset{A_1}{C}\xi^N = [0 + 0i - 0.26j - 0.97k - \varepsilon\,(0.48 + 0i + 0j + 0k)]\,,$$

which means a plane with normal vector $n = (0i - 0.26j - 0.97k)$ at distance d = 0.48 m from the origin. However, if it is desired to compute a point in the plane, then $\overset{A_1}{C}\xi^P$ can be used from Equation (10).

The representation of spherical SLE using DQ is presented in the next Section.

Figure 21 – Folding furniture for TV: orientation for planes emulating a flat display.

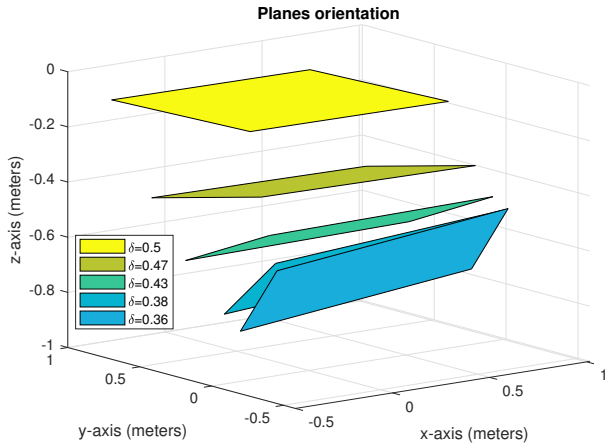

Source – From the author.

2.5 SPHERICAL ELEMENTS

In this section, a spherical SLE classification is presented, based on the classification shown above. Additionally, a kinematic representation of these spherical elements is detailed using a Screw dual quaternion (SDQ) operator. Some benefits of this type of spherical SLE are presented through practical applications.

2.5.1 Equivalence between planar and spherical SLE

An SLE unit, also known as pantograph, is two bars connected to each other at an intermediate point through a revolute joint called pivot which allows them to rotate freely about an axis perpendicular to their common plane but constrains all other degrees of freedom. The end points of these bars can be hinged to the next SLE unit. These joints are called hinges depicted on Figure 22. We can see on the left side the conventional SLE unit. On the right side, it can be visualized the spherical class of SLE both detailed through frontal, side and top view.
Based on the parameters in Figure 22 in the next section, a classifications for spherical SLE is presented.

2.5.2 Spherical SLE classification

Based on Figure 22 let define point A_1 as the pivot of any planar SLE unit, C_1, B_1 and C_2, B_2 as the left and right hinges respectively, same way with spherical SLE being the pivot defined as D_1; E_1, F_1 and E_2, F_2 left and right hinges. Depending on the bar lengths and the pivot position (AKGUN, Y., 2012) the SLE units can be classified as:

Figure 22 – Planar and spherical SLE unit a) isometric view b) front view c) side view d) top view.

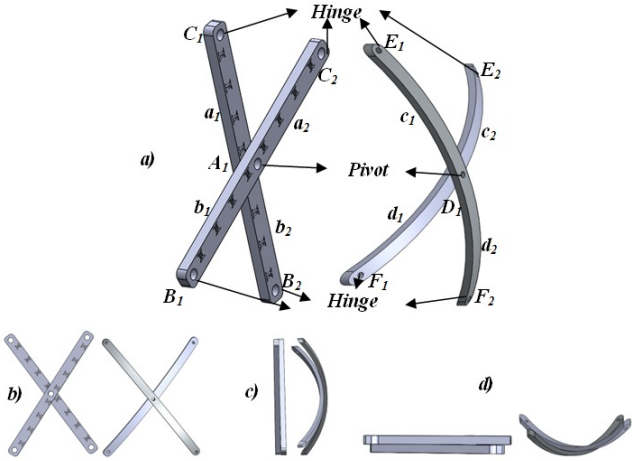

Source – From the author.

- Translational unit: Pivot A_1 and D_1 are located at the middle of the bars C_1B_2 and C_2B_1 for planar and E_1F_2, E_2F_1 for spherical units. The length of both bars is not necessary the same. The hinges of each bar and the pivot are collinear to each other.
- Polar unit: The only difference compared with translational units is that the bars' pivot is not at the middle.
- Angulated unit: The hinges of each bar and the pivot are not collinear to each other. The position of the pivot between the hinges of each bar and the bar's lengths is arbitrary.

The geometry of SLE assemblies depends on dimensions in bar's length and pivot location. These dimension are not arbitrary at all being necessary to achieve many conditions detailed in the following subsections.

2.5.2.1 Translational assemblies with constant bar length (SLE_S^{TC})

This type of structures can only translate without any rotation. When all bars have the same lengths $a_1 = a_2 = b_1 = b_2$ for the planar case and $c_1 = c_2 = d_1 = d_2$ for the spherical case (based on Figure 22), and the pivots are located in the middle of the bars, these assemblies describe a straight translation (as seen in Figure 23).

2.5.2.2 Translational assemblies with different bar length (SLE_S^{TD})

Similar to the previous case, the structure can only translate without any rotation. Bars configurations are $a_1 = b_2 < b_1 = a_2$ for the planar case and $c_1 = d_2 < d_1 = c_2$

Figure 23 – Translational assemblies - constant bar length: *i*. folding condition *ii*. deploying condition of planar assembly *iii*. folding condition *iv*. deploying condition (front view) *v*. deploying condition (side view) *vi*. deploying condition (top view) of spherical approach.

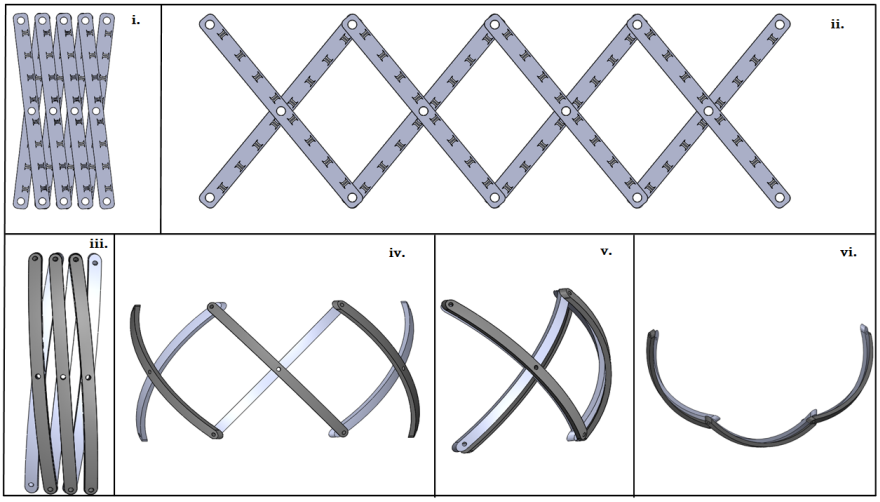

Source – From the author.

Figure 24 – Translational assemblies - different bar length: *i*. folding condition *ii*. deploying condition of planar assembly *iii*. folding condition *iv*. deploying condition (front view) *v*. deploying condition (side view) *vi*. deploying condition (top view) of spherical approach.

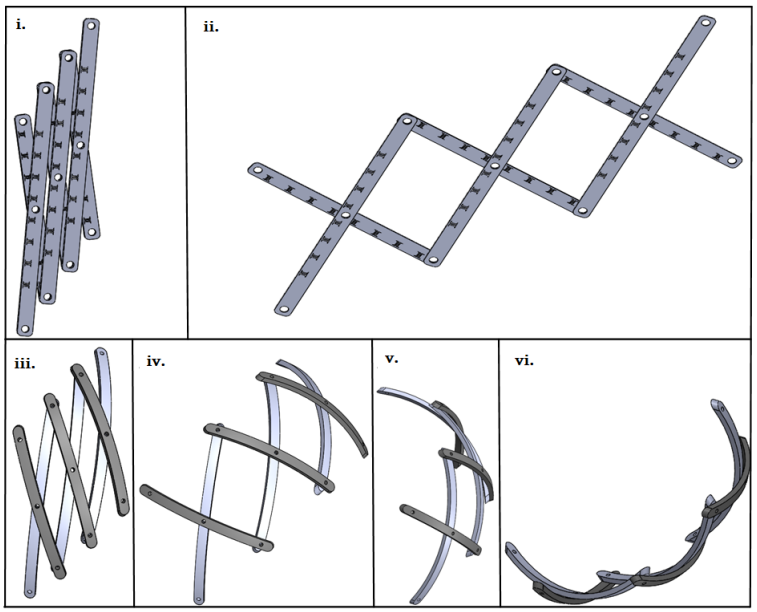

Source – From the author.

for the spherical case (based on Figure 22). These assemblies describe an inclined translation (as seen in Figure 24).

2.5.2.3 Curvilinear assemblies with polar units (SLE_S^P)

The main characteristic of this structures is to deploy and contract as a part of a single arc (as shown in Figure 25). Bars configurations are $a_1 = a_2 > b_1 = b_2$ for the planar case and $c_1 = c_2 > d_1 = d_2$ for the spherical case according to Figure 22.

Figure 25 – Curvilinear assemblies - polar units *i*. folding condition *ii*. deploying condition of planar assembly *iii*. folding condition *iv*. deploying condition (front view) *v*. deploying condition (side view) *vi*. deploying condition (top view) of spherical approach.

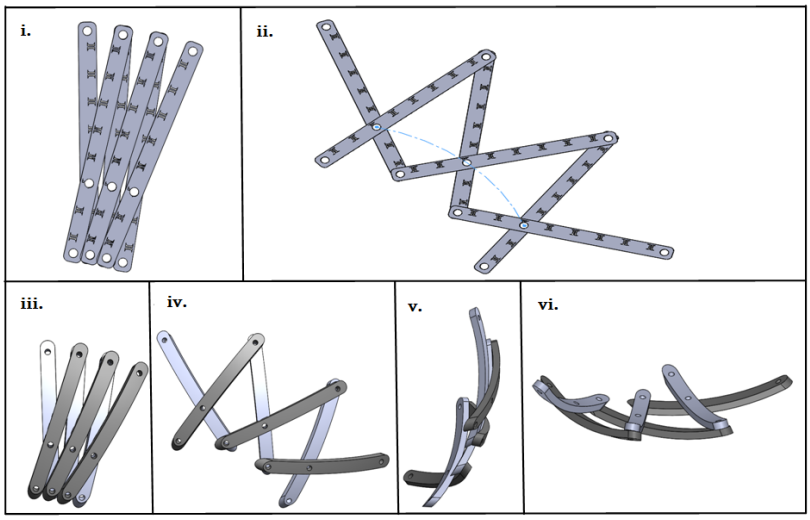

Source – From the author.

2.5.2.4 Curvilinear assemblies with GAE units (SLE_S^{GAE})

In the last typologies of assemblies described before, the pivot and the hinges were collinear. Oppositely, in this case, they are not collinear. For example the GAE units in Figure 26 have an angle of $\pi/2$ rad between the pivot and the hinges. On the other hand, the length of the bars is not a restriction according to designer interests.

Note

On Figure 24 the assembly has an ascending inclination. If it is desired a descending inclination, then the bar length condition would be $a_1 = b_2 > b_1 = a_2$ for planar and $c_1 = d_2 > d_1 = c_2$ for spherical units.

Figure 26 – Curvilinear assemblies - GAE units *i*. folding condition *ii*. deploying condition of planar assembly *iii*. folding condition *iv* .deploying condition (front view) *v*. deploying condition (side view) *vi*. deploying condition (top view) of spherical approach.

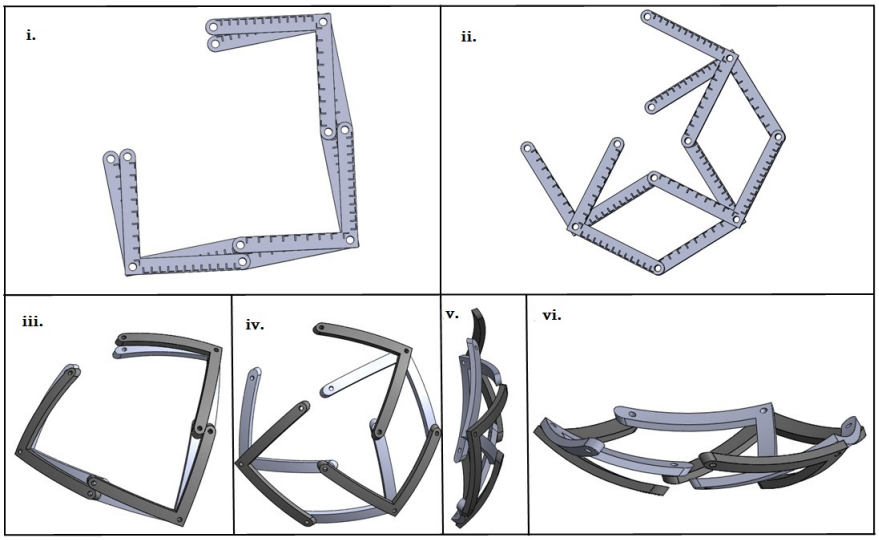

Source – From the author.

Same way in the case on Figure 25, if it is desired an ascending structure, then the conditions would be $a_1 = a_2 < b_1 = b_2$ for planar and $c_1 = c_2 < d_1 = d_2$ for spherical units. The following section presents a DQ representation of SLE units' kinematics shown in this section; besides, practical application of conventional and spherical SLE are presented through heterogeneous assemblies.

2.5.3 Application of DQ in spherical SLE

Spinners were used in the previous sections to form DQs that represent the kinematics of the SLE. Another possibility is to use an SDQ operator to form DQ. The SDQ operator is detailed as follows:

$$h = \begin{bmatrix} \cos\frac{\omega}{2} \\ \left(\sin\frac{\omega}{2}\right) s_x i \\ \left(\sin\frac{\omega}{2}\right) s_y j \\ \left(\sin\frac{\omega}{2}\right) s_z k \\ -\frac{\delta}{2}\sin\frac{\omega}{2}\varepsilon \\ \left(\frac{\delta}{2}\cos\frac{\omega}{2}\right) s_x \varepsilon i \\ \left(\frac{\delta}{2}\cos\frac{\omega}{2}\right) s_y \varepsilon j \\ \left(\frac{\delta}{2}\cos\frac{\omega}{2}\right) s_z \varepsilon k \end{bmatrix}^T \tag{12}$$

The DQ in Equation (12) represents a rotation ω around s, $\|s\| = 1$, with a position vector s_0, $s_0 \perp s$ and a translation $t = \delta s$ where δ is the shift along s, a displacement ξ' of a point $\xi = \begin{bmatrix} 1 & 0i & 0j & 0k & 0\varepsilon & 0\varepsilon i & 0\varepsilon j & 0\varepsilon k \end{bmatrix}$ is represented by $\xi' = h\xi h^*$, where h^* is a cojugate DQ of h, detailed information and its application in SLE systems can be found in (RADAVELLI, 2014; GRIJALVA, 2019). For convenience the SDQ operator is rewritten in spherical coordinates. Equation (6) shows the DQ representing the kinematic relations of the spherical SLE.

$$h_S = \begin{bmatrix} 1 & 0i & 0j & 0k & 0\varepsilon & \frac{r\cos\psi\cos\lambda}{2}\varepsilon i & \frac{r\cos\psi\sin\lambda}{2}\varepsilon j & \frac{r\sin\psi}{2}\varepsilon k \end{bmatrix}. \tag{13}$$

On Figure 27 it is depicted an spherical SLE unit, there the input aperture $\widehat{P} = \overline{EF}$ is the arc length between the input hinges E, F, $c_{1,2}$ is the arc length between the pivot D and the upper hinges, same way $d_{1,2}$ is the arc length from the center D to the lower hinges, τ and μ are the angles between the arc $\widehat{P}$ and both bars. For simplicity, in this case, it is employed spherical coordinates; thus, r is the radius, λ is the azimuth and φ is the elevation angle.

Figure 27 – Spherical SLE - geometrical parameters.

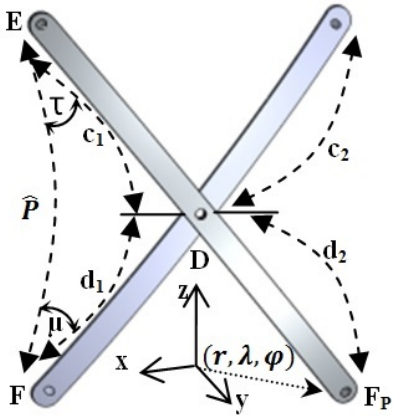

Source – From the author.

In order to form the DQ for each type of spherical SLE, the parameters of Equation (13) are presented in Table 2. According to Figure 27, for h_S^{TC} it can be said that $c = c_1 = c_2 = d_1 = d_2$, for h_S^{TD} it is held that $c = c_1 = d_2$ and $d = c_2 = d_1$, for h_S^{P} it is held that $c = c_1 = c_2$ and $d = d_1 = d_2$, finally for h_S^{GAE} it is held that $c = c_1 = c_2 = d_1 = d_2$ note that in this case the pivot and hinges are not collinear setting a perpendicular configuration. In Table 2, r is the radius of the spherical plane where the bars rotate freely. Based on Figure 27 note that $\hat{P} < c_1 + d_1$ and $0 < \tau, \mu < \pi/2$ rad.
Some of the DQ presented in this section are employed in practical examples below.

Table 2 – DQ parameters for spherical SLE units.

	h_S^{TC}	h_S^{TD}	h_S^P	h_S^{GAE}
ψ	$r^{-1}\sqrt{4c^2-\hat{P}^2}$	$r^{-1}(d\sin\mu + c\sin\tau)$	$r^{-1}d(\sin\mu+\sin\tau)$	$r^{-1}\left(c\sin\tau-\frac{\hat{P}}{2}\right)$
λ	0	$r^{-1}(d\cos\mu - c\cos\tau)$	$r^{-1}d(\cos\mu-\cos\tau)$	$r^{-1}\left(\frac{\hat{P}}{2}-c\cot\left(\frac{\hat{P}}{2c}\right)\right)$
μ	$\arccos\left(\frac{\hat{P}}{2c}\right)$	$\arccos\left(\frac{\hat{P}^2-c^2+d^2}{2\hat{P}d}\right)$	$\arccos\left(\frac{\hat{P}^2-c^2+d^2}{2\hat{P}d}\right)$	$\arccos\left(\frac{\hat{P}}{2c}\right)$
τ	μ	$\arccos\left(\frac{\hat{P}^2-c^2+d^2}{2\hat{P}c}\right)$	$\arccos\left(\frac{\hat{P}^2-c^2+d^2}{2\hat{P}c}\right)$	μ

Source – From the author.

2.5.4 Benefits and practical examples of spherical SLE

One of the main limitations of planar SLE is that to form three-dimensional structures it is necessary to use connectors leading into a structure with many joints and links. Using spherical SLE it is possible to form three-dimensional structures with fewer joints and links; accordingly, this section shows practical applications of spherical SLE, which will be compared with applications in which planar SLE is used.

2.5.4.1 Folding roof

It is possible to built three-dimensional applications by employing planar SLE. For example, the folding roof depicted in Figure 28 has perpendicular assemblies of SLE turning into an spatial structure. The length of each bar in the SLE from the structure shown in Figure 28 is equal to 12.5 cm. For the kinematic analysis, four reference points R_1^1, R_2^1, R_3^1 and R_4^1 and an origin O^1 are chosen. To compute the workspace, the approach presented in Section 2.3 is used.

The roof workspace is depicted on Figure 29, there it is possible to verify on the left side the workspace of the four reference points R_1^1, R_2^1, R_3^1 and R_4^1; on the right side by developing a mesh-grid of the data from the four points is shown the workspace of a folding roof; for example, if a plastic drape is deployed over the folding assembly the maximum covering capacity would be the area depicted on the right side of Figure 29. On the other hand, it is possible to design a folding roof by using spherical SLE. In Figure 30 one possibility is depicted, by employing homogeneous SLE_S^{TC}. In this case one reference point R_1^2 is chosen with an origin O^2. Since this is a homogeneous assembly it is possible to use DQ exponentiation to describe its kinematics as follows

$$\underset{R_1^2}{\overset{O^2}{A}} = \mathcal{H}_{S-TC}^4. \tag{14}$$

The main function of any roof is to cover a determined region. Let this area be called like the protected region (PR). Suppose an assembly of spherical SLE is projected on a plane, for example, the structure presented in Figure 30.b. In that case, the system's hinges will describe the vertices of a rectangle over the ground, it happens according

to the principle of transference (CHEVALLIER, D., 1996).

Figure 28 – Folding roof based built by planar SLE units: a) folding condition b) deploying condition, c) front view d) side view.

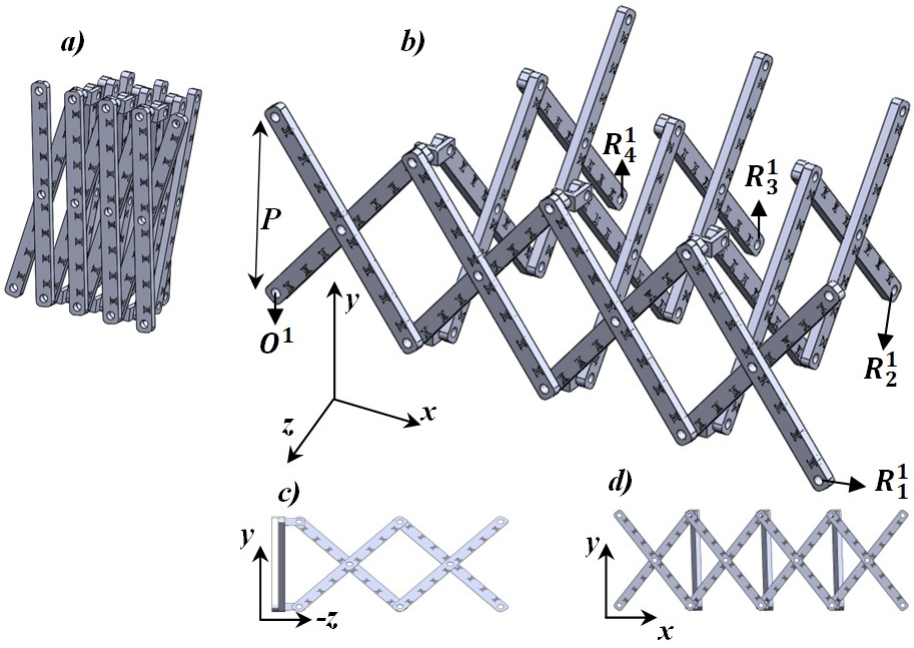

Source – From the author.

In Figure 30.a it is depicted a retractable roof structure, in folding condition, conformed by four spherical SLE ($n = 4$). On the right side, it is presented the structure in deploying condition. The dimensions of the PR defined by $A_{1,2,3,4}$ can be written in function of the parameters of the spherical SLE assembly as follows:

$$\overline{A_1A_2} = 2r \sin\left(\frac{n\hat{P}}{2r}\right) \tag{15}$$

$$\hat{P} = 2r \arcsin\left(\frac{\overline{A_2A_4}}{2r}\right) \tag{16}$$

$$a_h = \sqrt{\frac{\hat{P}^2}{2}} \tag{17}$$

$$H = r - \sqrt{\frac{4r^2 - \left(\overline{A_1A_2}\right)^2}{4}}, \tag{18}$$

where $a_h = c_1 = c_2 = d_1 = d_2$. Assuming that the desired dimensions for the PR are $\overline{A_1A_2}$ = 9m and $\overline{A_2A_4}$ = 2.76m, then by using Equation (15) and Equation (16), $\hat{P}$ = 2.8 m and r = 5 m can be computed. The length of the links of the spherical SLE can be defined by employing Equation (17); in this case it is held that a_h = 1.98 m.

Figure 29 – Folding roof built with planar SLE: workspace analysis.

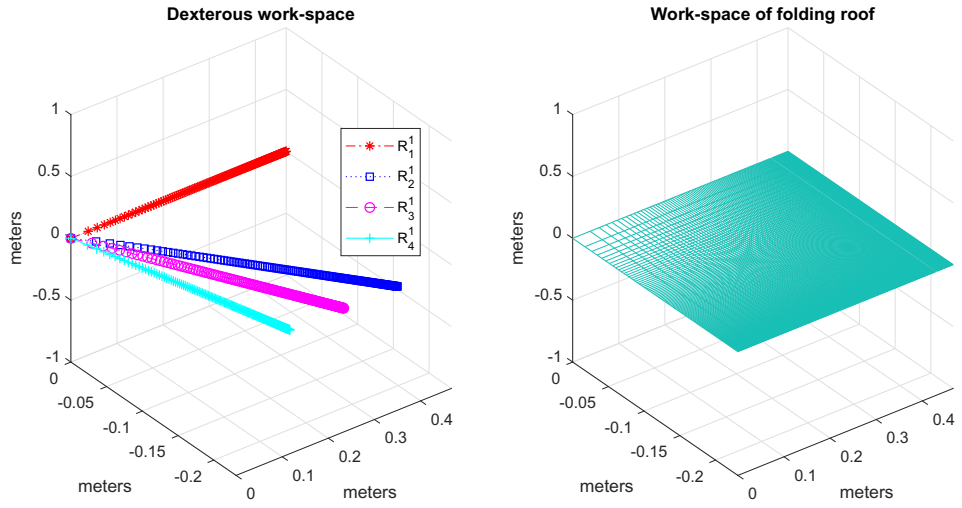

Source – From the author.

The height of the roof can be calculated using Equation (18); in this case it is held that H = 2.18 m. In conclusion the dimensions of the SLE_S^{TC}, according to Figure 27, are $c_1 = c_2 = d_1 = d_2$ = 0.198 m.

Figure 30 – Folding roof formed by spherical SLE: a) folding condition b) deploying condition.

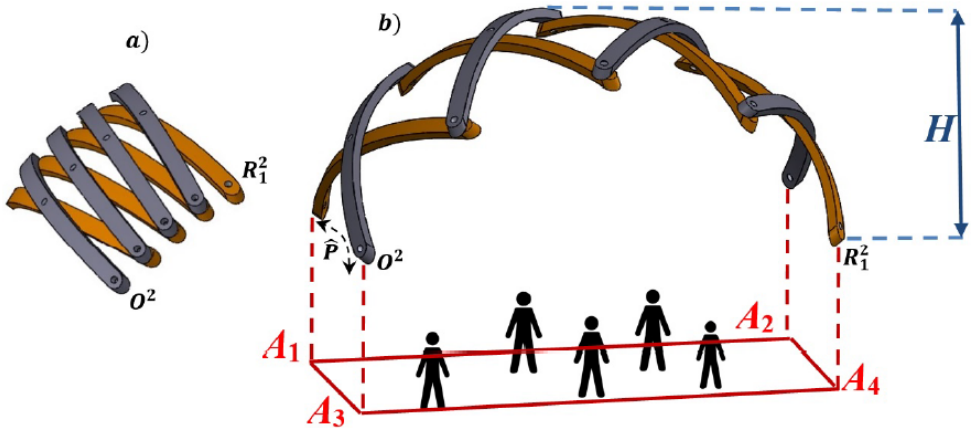

Source – From the author.

The workspace of this structure is depicted in Figure 31, on the left side it is plot the dexterous workspace for an aperture $\hat{P}$ in the range 0.5 < $\hat{P}$ < 1 m. Note that in the example on Figure 31, the workspace slides over a spherical hull. Due to the general folding condition, all the assemblies employing spherical SLE will slide over an spherical

hull.

Figure 31 – Folding roof built by spherical SLE: workspace analysis.

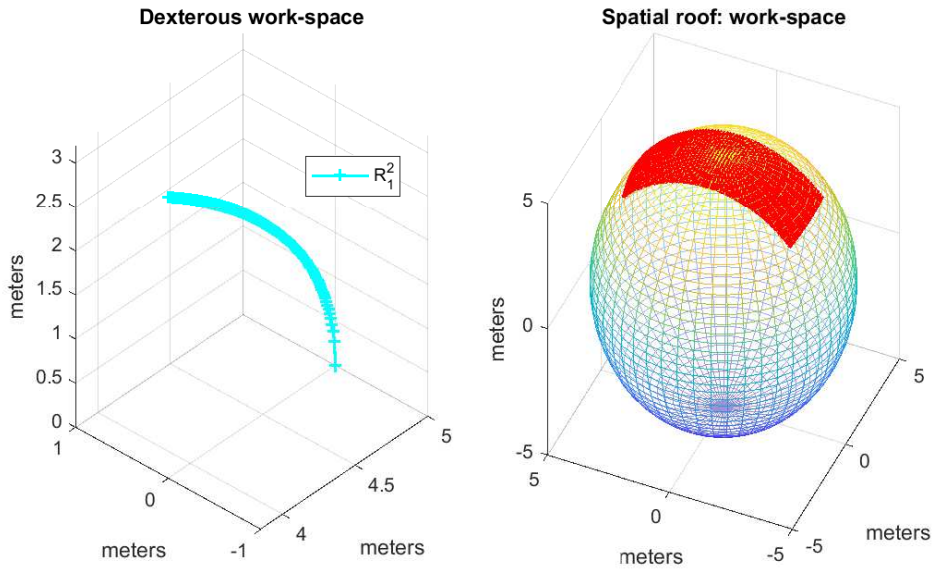

Source – From the author.

It can be clearly verified on the right side of Figure 31; for example, if a plastic drape is deployed over the folding assembly, then the covering capacity would be the area (in red) depicted over the reference sphere. It is important to highlight that in this case, the number of SLE decreases to four compared to the folding roof (Figure 28) built of planar SLE, which was made up of ten SLE units.

2.5.4.2 Retractable lamp

An alternative design for a three-dimensional retractable lamp structure is presented in Figure 32. This assembly is formed by heterogeneous SLE: one SLE_S^{TC} (in red), two SLE_S^{TD} (in blue) and one SLE_S^P (in green). Three reference points are chosen to be analyzed R_1^4, R_2^4 and R_3^4, the origin is set in O^4. By using DQ, the kinematic equations of the previously mentioned points are:

$$\begin{aligned} {}^{O^4}_{R_1^4}A &= h_S^{TC}\xi h_S^{TC*} \\ {}^{O^4}_{R_2^4}A &= h_S^{TC}h_S^{TD}h_S^{TD}\xi h_S^{TD*}h_S^{TD*}h_S^{TC*} \\ {}^{O^4}_{R_3^4}A &= h_S^{TC}h_S^{TD}h_S^{TD}h_S^{p}\xi h_S^{p*}h_S^{TD*}h_S^{TD*}h_S^{TC*}. \end{aligned} \tag{19}$$

According to Figure 27, the dimensions of the spherical folding lamp structure are: $c = c_1 = c_2 = d_1 = d_2 = 0.25$ m for SLE_S^{TC}, in the SLE_S^{TD} it is held that $c = c_1 = d_2 = 0.3$ m and $d = c_2 = d_1 = 0.2$ m and for SLE_S^P the dimensions are $c = c_1 = c_2 = 0.35$ m and

$d = d_1 = d_2 = 0.15$ m.

Figure 32 – Spherical lamp structure: a) folding condition b) deploying condition (isometric view) c) front view d) side view e) top view.

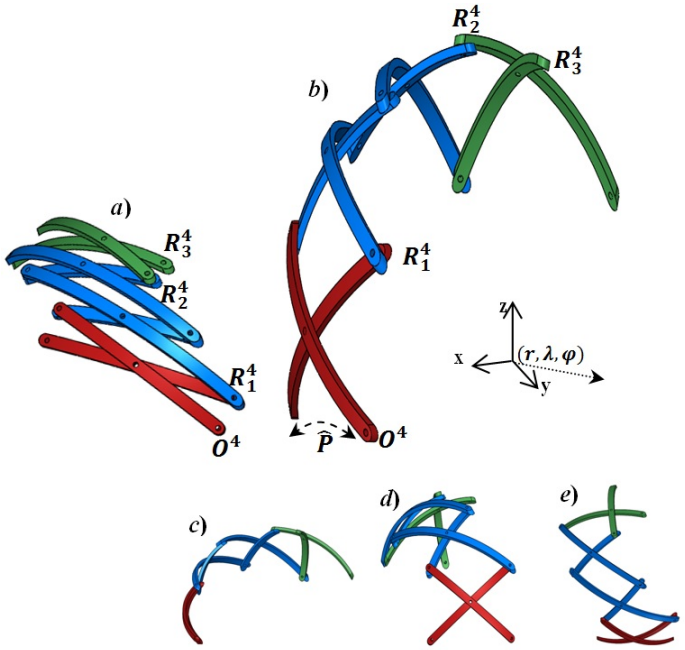

Source – From the author.

Note that in this case the measures are referred to arc lengths with radius $r = 3.5$ m achieving the general folding conditions.

Figure 33 – Dexterous workspace of spherical retractable lamp structure.

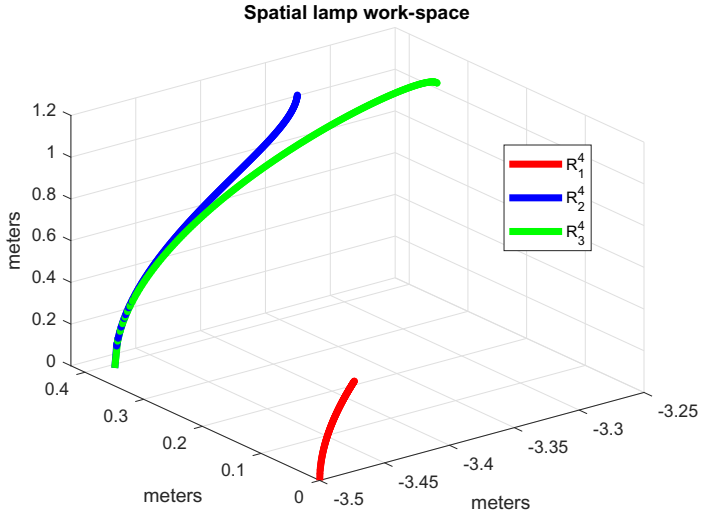

Source – From the author.

The dexterous workspace of the spherical folding assembly depicted in Figure 33 is computed using Algorithm 2, there the aperture $\hat{P}$ is in the range $0.25 < \hat{P} < 0.5$ m.

2.6 CHAPTER CONCLUSION

This chapter addresses the kinematic analysis of SLE structures based on DQ. It starts with SLE representation, connectors, and end-effectors by DQ. Kinematic relations of homogeneous assemblies of SLE are simplified by using DQ exponentiation. The analysis of singularities is developed by Algorithm 1. Using Algorithm 2 it is possible to detect singularities in the SLE structure which are considered in the computation and plotting of reachable or dexterous workspace. The kinematic theory developed in the beginning of the chapter was applied in practical examples. Also, some practical examples shows the DQ characteristics to orientate points, lines and planes.

A classification for spherical SLE was presented based on planar SLE. The main difference between planar and spherical SLE is that conventional SLE rotate over an straight plane while spherical SLE do it over an spherical plane. This fact restricts the possibility of create planar assemblies by using the spherical approach. On the other hand, it gives a new possibility to create structures that can not be possible employing planar SLE. In general the advantages and drawbacks between planar and spherical SLE, can not be defined; these are going to depend strictly on the application.

3 SCISSOR-LIKE ORIGAMI

Inspired by a folding hand fan; this chapter presents a novel kind of semi-soft mechanism composed of scissor-like elements (SLE) and origami. The main function of the SLE assembly is to regulate the motion and performance of origami, avoiding the need for smart material, which is typically used as actuators in origami robots. A methodology to design a broad range of possible shapes for scissor-like origami (SLO) devices is introduced starting from a simple crease pattern and conventional SLE. SLO can unfold into large structures and fold compactly in addition to the potential of yield compliance being an option to consider when designing robot limbs, solar panels, and structures for space exploration.

Using hands and a single sheet of paper, complex flat (2D) or three-dimensional (3D) objects with distinct mechanical properties can be manufactured by folding, making origami a quick and inexpensive option for prototyping (CHEN et al., 2019). In the last decades, engineers and researchers have been gradually constructing origami applications in aerospace, architecture, robotics, biomedicine, and other fields (ZHOU, 2017; LI; PENG, R., 2018; CHEN; BHOVAD; NELSON, T., 2019). Origami can have more degrees of freedom (DoF) than conventional machines (RUS, D., 2018). For example, a manipulator arm typically has six or fewer DoF. The large amount of DoF in origami can lead to the need to use numerous actuators and sensors to control motion and performance.

The control of origami devices, assuming rigid faces and lower pairs in folds, includes angle control and coordination of the various joint actuators to regulate their morphology. One possibility is to use nonconventional sensors, like carbon ink or flexible piezoresistive sensors. Another possibility is to control the origami systems with open-loop controllers (RUS, D., 2018). Feedback origami systems, such as the fluid-driven origami robot presented in (LI et al., 2017), require specialized pneumatic equipment and a precise manufacturing method. In other cases, the entire body of origami is made from smart materials like piezoelectric, alloys, and shape memory polymers. Due to hysteresis, many actuators, the lack of sensors, or the need of specialized equipment, controlling origami can be expensive, complex, or imprecise. Another possibility could be the coupling of an external mechanism, for example a deployable structure composed of SLE that will regulate the motion and configuration of the creases in the origami.

There are key hardware and software challenges related to materials, control, mechanisms, and other fields to promote the development of origami-based robots with application in biomedical devices, renewable energy, space exploration, etc. Thus, this chapter shows SLO, a semi-soft mechanism that inherits mechanical attributes from SLE and origami, such as the potential of yield compliance, folding capability, and

lightweight despite the large size it can reach.

3.1 FOUNDATIONS OF SCISSOR-LIKE ORIGAMI

Origami is an ancient art that was originated in China and spread to Japan in the Tang Dynasty (CHEN et al., 2019). A practical application of origami in ancient times was folding hand fans. It is not possible to specify the origin of the fan, neither in time nor in space (PEREZ-GONZALEZ, J., 1994). Based on ancient murals, paintings, and poems, it is possible to conclude that many civilizations knew the hand fan, such as Egyptian, Assyrian, Greek, etc., whose main purpose was to relieve the suffocating heat. Inspired by the design of a bat's wing, the first folding fan registered in China, made of light blue paper and bamboo, was brought by a Japanese monk in 988 A.D. (QIAN G., 2004). The advantages of a rigid structure coupled to origami, like the folding hand fan, are the main motivation to research the SLO method. Therefore, this section describes the main parts of SLO based on the standard structure of the folding hand fan.

3.1.1 Parts of a folding hand fan

According to Figure 34, the standard main parts of the folding fan are (PEREZ-GONZALEZ, J., 1994):

Figure 34 – Parts of a folding fan: 1. rod, 2. guide, 3. gate, 4. origami, 5. pivot.

Source – From the author.

1. *Rod:* This item is a thin straight bar, especially made of wood or metal. The rods are divided into two parts: the guide and the gate;
2. *Guide:* This part of the rod is glued to the faces or folds of the origami;

3. *Gate:* This part of the rod is responsible for transmitting the movement of the user's hand to the guide and origami. Furthermore, the morphology of origami is governed by this part;

4. *Origami:* This is the soft part of the fan that makes up most of the fan body. It is usually made of paper, cardboard, silk and vellum. Thanks to this item, the handheld fan has a light weight, although it can reach a large size.

5. *Pivot:* The bottom of the folding hand fan rods are joined to each other at a joint called pivot.

3.1.2 Origin of SLO

The shape of the folding fan, shown above, has an inaccurate configuration because the positioning of the rods depends on the user's hand.If an SLE assembly replaces the fan pivot, it is possible to regulate the fan morphology accurately, as shown in Figure 35.

Figure 35 – Folding fan based on SLO: a) folding condition, b) deployed condition.

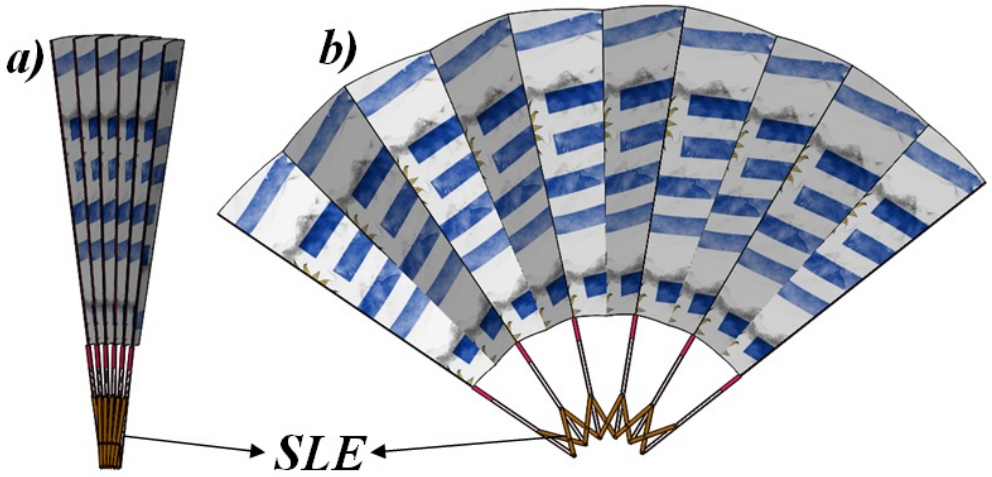

Source – From the author.

Moreover, the problem of controlling the whole device is simplified to controlling the SLE. In the same way, SLO kinematic analysis could be developed using well-known approaches employed in SLE kinematic analysis. In the SLO device in Figure 35 it is possible to see the SLE structure composed of five polar SLE guiding the configuration and performance of the origami without interfering with the fan's functionality.

3.1.2.1 SLO Definition

An SLO unit consists of an SLE coupled to an origami fold through rods so that the mobility of the origami is not interrupted by the SLE and vice versa, but even the SLE does not alter the functionality of the origami.
The definition presented above will be demonstrated in the remainder of this chapter. The methodology for designing four SLO morphologies using a simple crease pattern is introduced in the next section.

3.2 MORPHOLOGIES DESIGN METHODOLOGY

This section shows that using a simple symmetric crease pattern and translational and polar SLE can achieve various SLO morphologies. It is important to highlight that this technique is not limited to the pattern presented in this section.

Figure 36 – Crease pattern.

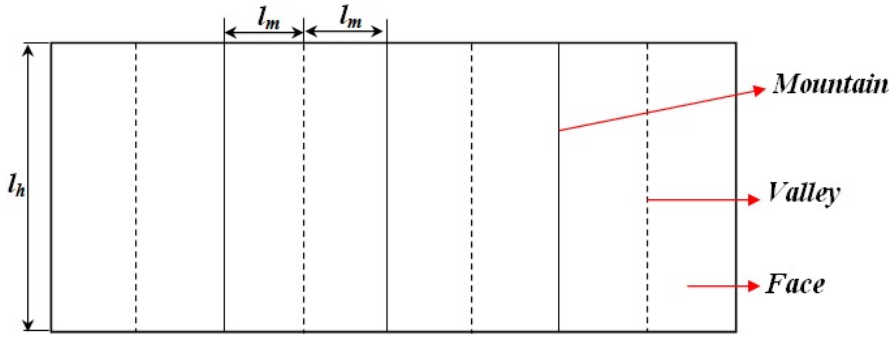

Source – From the author.

A crease refers to the line segment marked on the paper after being folded. Depending on the direction in which the paper is folded, creases can be divided into *mountain* creases and *valley* creases as shown in Figure 36. The area surrounded by these creases is the origami *face*, which will not be deformed during folding in an ideal case.

3.2.1 SLO using translational SLE

According to the classification for SLE presented in the last chapter, two types of translational SLO are defined:

3.2.1.1 Translational SLO with constant bar length

Translational SLE with constant bar length are used in straight configurations. In Figure 37, it is depicted an SLO assembly formed by four translational SLE with constant bar length.

Figure 37 – Translational SLO with constant bar lengths and collinear rod: a) folding condition, b) deployed condition.

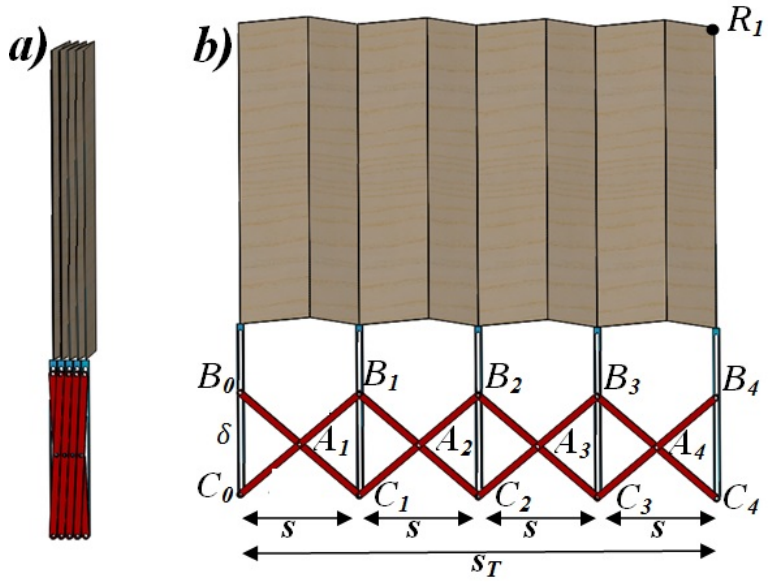

Source – From the author.

To design the morphology in Figure 37 it can be used the next geometrical relations

$$s = \sqrt{4a^2 - \delta^2}, \tag{20}$$

$$s_T = Ns = 8l_m, \tag{21}$$

where $a = \overline{B_0A_1} = \overline{C_0A_1} = \overline{A_1B_1} = \overline{A_1C_1}$, l_m is the distance between the mountain and the valley creases (see Figure 36), N is the number of SLE, and $\delta = \overline{B_0C_0}$ is the input overture of the SLE. Using Equation (20) and Equation (21), it is possible to calculate the distance l_m in the pattern of Figure 36. In the examples presented in the Figures 35 and 37, the guide and the gate, in the rod are collinears. It is possible to modify the angle between the gate and the guide. For example, in Figure 38 the gate and the guide are perpendiculars. This possibility gives the chance to create a greater variety of SLO morphologies.

Example

For the morphology depicted in Figure 37, compute the maximum dimensions and creases of a sheet of paper. The pattern shown in Figure 36 considers a length $a = 6$ *cm for each SLE and a maximum overture* $\delta = 5$ *cm.*

Using Equation (20) it can be calculated the span $s = 10.9$ cm for each SLE, then by multiplying s by the N number of SLE, in this case $N = 4$, it can be held that $s_T = 43.63$ cm, that is the length of the unfolded origami.

Figure 38 – Translational SLO with constant bar lengths and perpendicular gate and guide: a) folding condition, b) deployed condition.

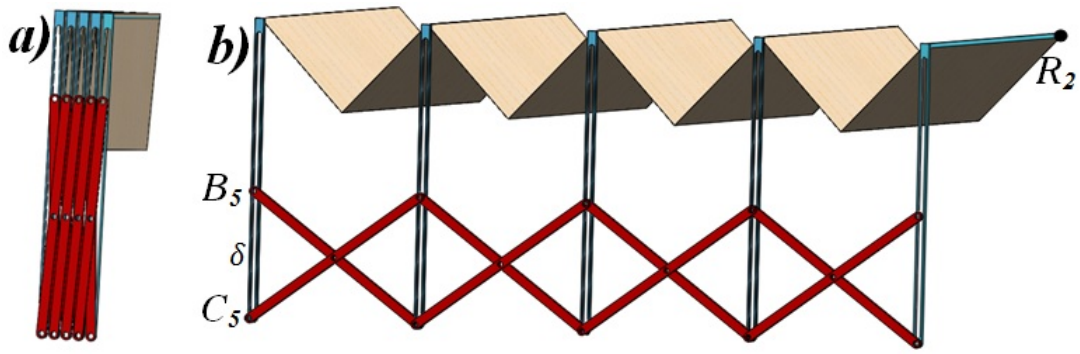

Source – From the author.

The distance between valleys and mountains can be computed using Equation (21), l_m = 5.45 cm. The height l_h of the origami (see Figure 36) has not restrictions. These results can also be used in the morphology depicted in Figure 38, where the gate and the guide are perpendiculars.

3.2.1.2 Translational SLO with different bar length

Translational SLE with different bar length are employed in tilted assemblies. The SLO structure in Figure 39 comprises four translational SLE with different bar lengths. The main geometrical relations of the SLO in Figure 39 are described as follows

$$r = \sqrt{\left(d\sin\hat{\alpha} + c\sin\hat{\beta}\right)^2 + \left(d\cos\hat{\alpha} - c\cos\hat{\beta}\right)^2}, \tag{22}$$

$$\hat{\alpha} = \arccos\left(\frac{\delta^2 + d^2 - c^2}{2\delta d}\right), \tag{23}$$

$$\hat{\beta} = \arccos\left(\frac{\delta^2 + c^2 - d^2}{2\delta c}\right), \tag{24}$$

$$r_T = Nr = 8l_m, \tag{25}$$

with $c = \overline{E_0D_1} = \overline{D_1F_1}$, $d = \overline{F_0D_1} = \overline{D_1E_1}$, $\hat{\alpha} = \angle E_0F_0D_1$, $\hat{\beta} = \angle F_0E_0D_1$, and $\delta = \overline{E_0F_0}$ is the input overture. To obtain an ascending inclination as depicted in Figure 39 the length of d must be greater than c.

Figure 39 – Translational SLO with different bar lengths and perpendicular gate and guide: a) folding condition, b) deployed condition.

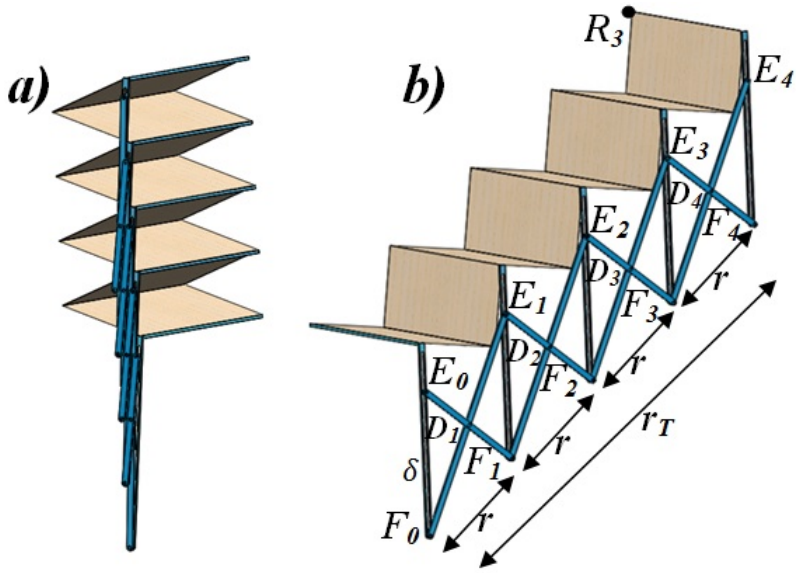

Source – From the author.

Example

Calculate the dimensions and creases of a sheet of paper, as shown in Figure 36, to assemble the morphology depicted in Figure 39. The bars of the translational SLE have the following dimensions: c = 8 cm, d = 4 cm, and the maximum overture $\delta = 7$ *cm.*

The angles $\hat{\alpha}$ and $\hat{\beta}$ can be obtained using Equations (23) and (24); thus, it can be held that $\hat{\alpha} = 0.52$ rad and $\hat{\beta} = 1.55$ rad, the span $r = 10.63$ cm is computed using Equation (22), the length of the paper $r_T = 42.51$ cm and the distance $l_m = 5.31$ cm between valleys and mountains are calculated using Equation (25). The height l_h of the sheet of paper could be equal to or greater than the length of the guide in the rod.

3.2.2 SLO using polar SLE

In the last subsection, by using translational SLE, the deployment of origami followed a linear trajectory. In this subsection, SLO using polar SLE is introduced to form curvilinear trajectories in the deployment of the origami. The geometrical relations employed in this configuration are detailed below

$$\hat{\varepsilon} = \arccos\left(\frac{\delta^2 + f^2 - e^2}{2\delta f}\right), \tag{26}$$

$$\hat{\eta} = \arccos\left(\frac{\delta^2 + e^2 - f^2}{2\delta e}\right), \tag{27}$$

$$\hat{\gamma} = \frac{\hat{\varepsilon} + \hat{\eta}}{2}, \tag{28}$$

$$\hat{\theta} = \arctan\left(\frac{e\sin\hat{\gamma} - f\sin\hat{\gamma}}{e\cos\hat{\gamma} + f\cos\hat{\gamma}}\right), \tag{29}$$

$$\overline{OI_1} = \frac{e\sin\hat{\gamma} - \delta\sin\hat{\theta}}{\sin\hat{\theta}}, \tag{30}$$

$$\overline{OH_0} = \overline{OI_1} + \overline{I_1H_0}, \tag{31}$$

$$t = 2\overline{OH_0}\cos\hat{\theta}, \tag{32}$$

$$Nt = 8l_m, \tag{33}$$

where $e = \overline{I_3G_1} = \overline{I_4G_1}$, $f = \overline{I_1G_1} = \overline{I_2G_1}$, $\hat{\varepsilon} = \angle I_3I_1G_1$, $\hat{\eta} = \angle I_1I_3G_1$, $\hat{\gamma} = \angle I_3G_1O_1$, $\hat{\theta} = \angle H_0OO_1$, and $\delta = \overline{I_1I_3}$ the input overture. Note that $\overline{I_1H_0}$ is a constant value equal to the length of the gate.

Figure 40 – Polar SLO with perpendicular gate and guide: a) folding condition, b) deployed condition (isometric view), c) deployed condition (frontal view), d) geometrical parameters.

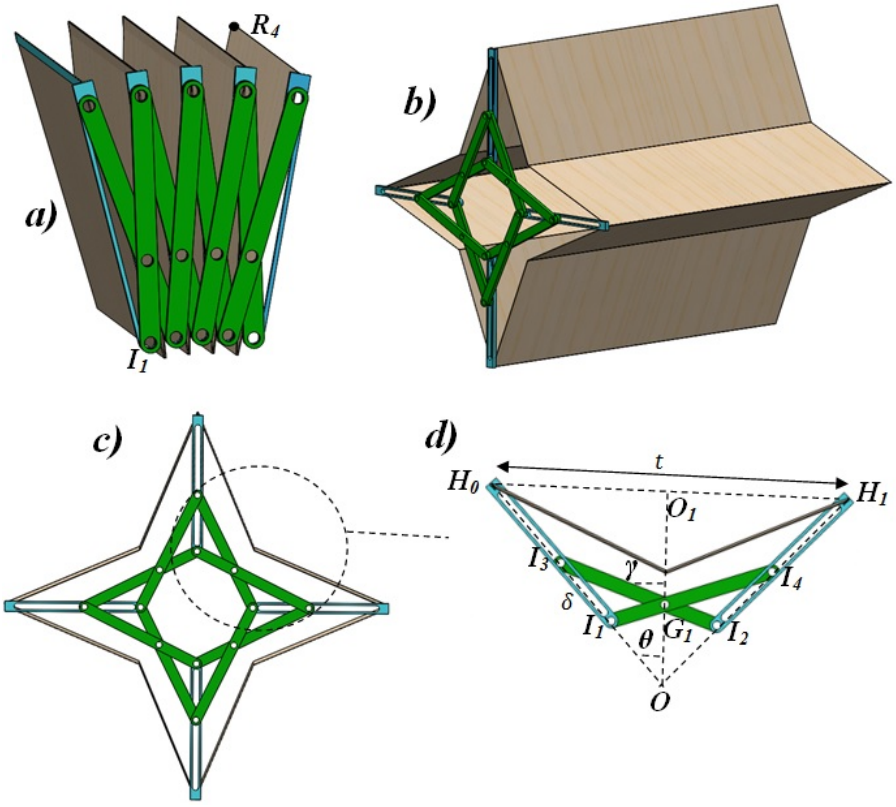

Source – From the author.

3.2.2.1 Example

Calculate the dimensions and creases in the origami of the SLO in Figure 40. The SLE assembly has the following dimensions e = 6 *cm,* f = 3 *cm and* δ = 5 *cm.*
The angles $\hat{\varepsilon}$ = 1.63 rad, $\hat{\eta}$ = 0.52 rad, $\hat{\gamma}$ = 1.07 rad, and $\hat{\theta}$ = 0.54 rad are computed using Equations (26)-(29). The length of the gate $\overline{I_1 H_0}$ can be any value greater than $e + f$ = 9 cm, so it is chosen a value of 10 cm. Using Equations (30)-(33), the value of l_m = 13.06 cm can be obtained which is the distance between mountains and valleys according to the pattern in Figure 36. The length of the unfolded origami is 52.27 cm and the height of the paper is equal to or greater than the guide in the rod. Note that in this example, the origami configuration is not closed like the design in Figure 40. It happened because the value of $\hat{\theta} < \pi/4$. If it is desired to obtain a closed configuration, then $\hat{\theta} = \pi/4$.

3.3 KINEMATIC ANALYSIS

In SLO kinematic analysis, it is possible to take advantage of the semi-soft property of the mechanism. The solid parts in the SLO, the SLE and the rods, can be used as references to calculate the motion in the origami. There are many approaches to deal with multibodies kinematics specially focused on SLE. For example, the Denavit-Hartenberg method (TSAI L., 1999) or the matrix dependency constraint method (FARRUGIA P., 2008); the screw theory or the approaches presented in (ZHAO, 2009; FENG, 2014) are available. Using DQ we can find the approach presented in Chapter 2. In the next numerical example, DQ is used in the kinematic analysis of arbitrarily located points in the SLO mechanisms shown above.

3.3.1 Example

According to the numerical examples presented in Section 3.2, determine the displacements of the points R_1, R_2, R_3 and R_4 on the SLO mechanisms from Figures 37-40 using DQ. The thickness of the origami is l_t = 2 mm and its height is l_h = 30 cm. The displacements of the points R_1, R_2, R_3 and R_4 are plot in Figure 41 which start from a folded state to a deployed state in the SLO. Note that the analyzed points are located on the origami; nonetheless, the kinematic analysis of points located on the rigid structure can also be computed using the approaches as mentioned earlier.

3.4 CHAPTER CONCLUSION

Inspired by folding hand fans, SLO-based machines with built-in compliance and rigidity can be used for physical tasks requiring the device's softness and rigidity. The synergistic coupling of SLE and rods in origami offers the possibility of creating

lightweight devices considering the large size they can reach and precisely controlled using well-known approaches.

Figure 41 – Kinematic analysis of points R_1, R_2, R_3, and R_4 from Figures 37-40.

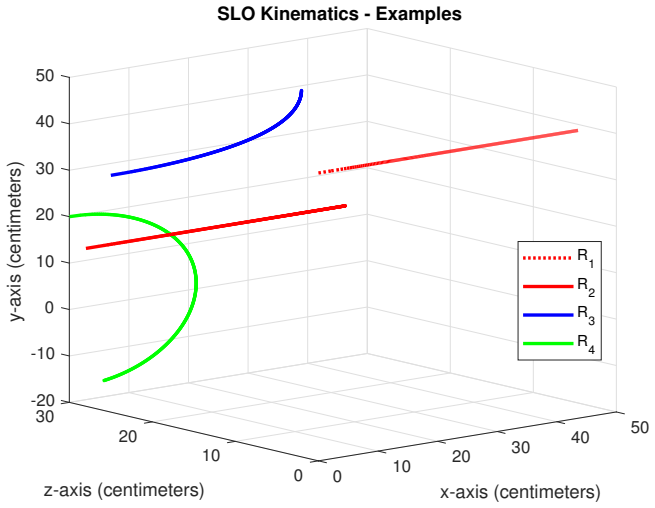

Source – From the author.

Four morphologies were presented using a simple pattern and homogeneous SLE assemblies. The kinematic analysis of four points located on the origami of the four SLO morphologies was developed using DQ.

4 DYNAMICS AND ROBUST CONTROL

Mechatronics is the synergy between mechanics, control and automation systems. The previous chapters considered a proposal to deal with the mechanical design of folding assemblies based on SLE and origami. Now it is time to focus over the dynamics and the controller, which will interact with the mechanical system through actuators and other electronic devices. One of the challenges of this research is to propose a procedure to design, as easy and effective as possible, folding mechatronics-based products. Accordingly, this Chapter presents an approach to deal with the dynamics and robust control in continuous time of SLE-based systems.

4.1 OBTAINING THE DYNAMIC EQUATION: STRATEGY

System identification has been widely employed in automation and control theory (LENNART, L., 1999). Despite any SLE assembly has one DoF (YOU Z., 2014), this kind of structures has plenty of revolute joints. By using Newtonian or Lagrangian mechanics, it is possible to obtain the dynamic equation. If the number of links and joints increases, it could increase the order of the differential equation. Usually, mechanical systems involve friction, stiffness, vibration, and other dynamical issues. When Newtonian or Lagrangian methodologies are employed, these dynamic issues are omitted because of complexity, low influence, lack of knowledge, among other reasons, affecting the precision of the dynamic equation. An alternative is an identification approach based on an MSD model because those models have one DoF and a limited region of motion. Analogous to the dynamic modeling of car-suspensions or human dynamic effects on structures that are not necessarily assembled with an MSD mechanism, many researches employ this approach to represent their dynamics (ALY, 2012; LAI, 2017).

4.1.1 Analogous MSD model

The MSD model consists of mass nodes distributed throughout an object and interconnected via a network of springs and dampers. There are many configurations of MSD models depending on the system to be simulated. Any SLE-based system has one DoF. The model is represented in Figure 42, which consists of a mass m interconnected to the ground by a parallel configuration of spring with constant k, and a damper with viscous damping coefficient b. This model is chosen to simulate an SLE system. On the up-left side of Figure 42 there is a retractable mirror in the folding state and the up-right side in the deploying state. Below, the MSD model configuration employed in this research to simulate a SLE based system is depicted. Both systems need one force F in one direction to move the mass. This force is considered as the input force provided by the actuator to the dynamic system.

Figure 42 – Analogy between an SLE system (a retractable mirror) and an MSD model.

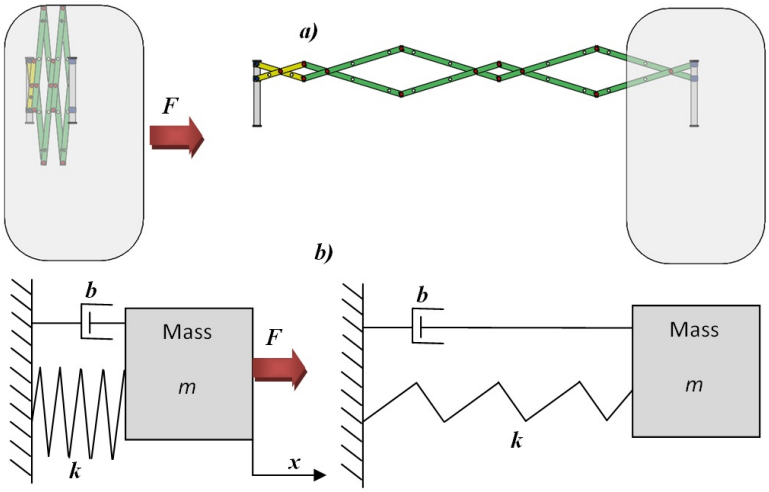

Source – From the author.

4.1.2 Parameters description and state equation

System identification theory offers the possibility to compute desired parameters based on input-output data from experimental plants. In this case, the parameters of interest are the mass m, the spring constant k, and the viscous damping coefficient b. The experimental plant is affected by an input force F causing a displacement x to the mass. Based on Figure 42, the following dynamic model is defined

$$\sum fx = 0 \longrightarrow m\ddot{x} + b\dot{x} + kx = F. \tag{34}$$

By applying Laplace transformation in Equation (34) with $x(0) = 0$ and $\dot{x}(0) = 0$, and defining the input force as $f(s)$ and the movement output as $y(s) = x(s)$, it can be held that

$$G_{(s)} = \frac{y(s)}{f(s)} = \frac{F}{ms^2 + bs + k} \tag{35}$$

therefore, the state equation is

$$\underbrace{\begin{bmatrix} \dot{x_1} \\ x_2 \end{bmatrix}}_{\dot{x}_f} = \underbrace{\begin{bmatrix} 0 & 1 \\ -\frac{k}{m} & -\frac{b}{m} \end{bmatrix}}_{A_f} \underbrace{\begin{bmatrix} x_1 \\ x_2 \end{bmatrix}}_{x_f} + \underbrace{\begin{bmatrix} 0 \\ \frac{1}{m} \end{bmatrix}}_{B_f} \underbrace{\begin{bmatrix} F \end{bmatrix}}_{u} \tag{36}$$

where the state x_1 is the displacement and the state x_2 is the velocity.

4.1.3 Least Squares

The least squares method provides the overall rationale for the placement of the line of best fit among the data points. The most common application of the least squares

method is to interpolate a straight line that minimizes the sum of the squares of the errors. This method of regression analysis correlates with a set of data points. In this case, the input force corresponds to the independent variable associated with the input, and the output is the displacement of the mass associated with the system's output. The linear equation that best fits these points is determined trough last squares method. This method employs discrete time models, based on Equation (34) it is proposed an Auto-regressive with exogenous input (ARX) model given by

$$x_k + a_1 x_{k-1} + \cdots + a_{n_a} x_{k-n_a} = b_1 u_{k-n_k} + \cdots + b_{n_b} u_{k-n_k-n_b+1} + e_k \tag{37}$$

in (37) k is each sample at a discrete time and e_k is zero-mean white noise, then it is possible to predict the next output value given previous observations:

$$x_k = -a_1 x_{k-1} - \cdots - a_{n_a} x_{k-n_a} + b_1 u_{k-n_k} + \cdots + b_{n_b} u_{k-n_k-n_b+1} + e_k \tag{38}$$

in compact form

$$x_k = \varphi_k^T \theta + e_k \tag{39}$$

where

$$\theta = \begin{bmatrix} -a_1 & -a_{2_a} & \cdots & b_{n_b} \end{bmatrix}^T \tag{40}$$

$$\varphi_k = \begin{bmatrix} x_{k-1} & x_{k-2} & \cdots & u_{k-n_k-n_b+1} \end{bmatrix}^T \tag{41}$$

Equation (40) is the parameter vector, and Equation (41) is the regressor. By optimization, the minimal error (LENNART, L., 1999) between estimated and given data is:

$$\widehat{\theta} = \left(\varphi_k^T \varphi_k\right)^{-1} \varphi_k^T x_k \tag{42}$$

where $\widehat{\theta}$ are the identified parameters. Using a Zero-order hold (ZOH), the identified parameters in $\widehat{\theta}$ can be expressed in continuous time, using Equation (36).

4.1.4 Example

Identify the parameters of the retractable mirror depicted in Figure 42.

Since there is no real plant, Computer-aided design (CAD) to create a solution was employed. Then, it was loaded to Simulink by using *Simmechanics* toolbox. In this way were carried out all the simulations of all the SLE systems presented in this Chapter.

4.1.4.1 Simulation

In this case, the system's input is the force supplied by a linear actuator, and the output is the position of the mirror. A ramp input was applied; see Figure 43, in the actuator.

Figure 43 – Input-output signals.

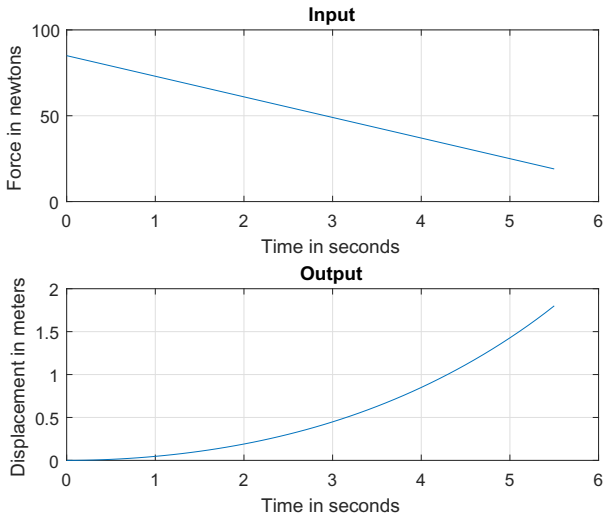

Source – From the author.

Figure 43 shows the system's output which represents the deployment of the mirror system. It was tested other inputs such as step and sinusoidal forces. The step input sends an inaccurate parameters estimation than the one shown in Figure 43. On the other hand, the sinusoidal input did not cover all the reachable region of the mirror, leading to an inaccurate estimation. Then, the ramp input was the best option compared with other conventional inputs.

The sample time, in the simulation, is 0.1 seconds; it was chosen because the mirror is supposed to follow people, then it is a slow process. Moreover, the variation in the output is not representative in 0.1 seconds. Thus there is no loss of important information in the identification process. By using the data from Figure 43 and the Equation (42), the next parameters are identified:

$$\begin{aligned} m &= \quad 9.15[kg] \\ b &= \quad 1.38[kg.m/s] \\ k &= \quad 0.075[kg/m] \end{aligned} \tag{43}$$

In Figure 44 it is compared the estimated with the actual system using the parameters in Equation (43).

Based on the results in Equation (43), the system's error is depicted in Figure 45. Based on Figure 44, the maximum error in the estimation is about 5.5 *cm* which could be considered insignificant in this application. Figure 45 shows the error estimation at each sample and uses the same scales than Figure 44. Let consider the estimation

error in each sample as ξ_i, then the sum of the square error is defined as $J_{LS} = \sum_{i=1}^{N} \xi_i^2$ (LENNART, L., 1999).

Figure 44 – Actual vs estimated outputs.

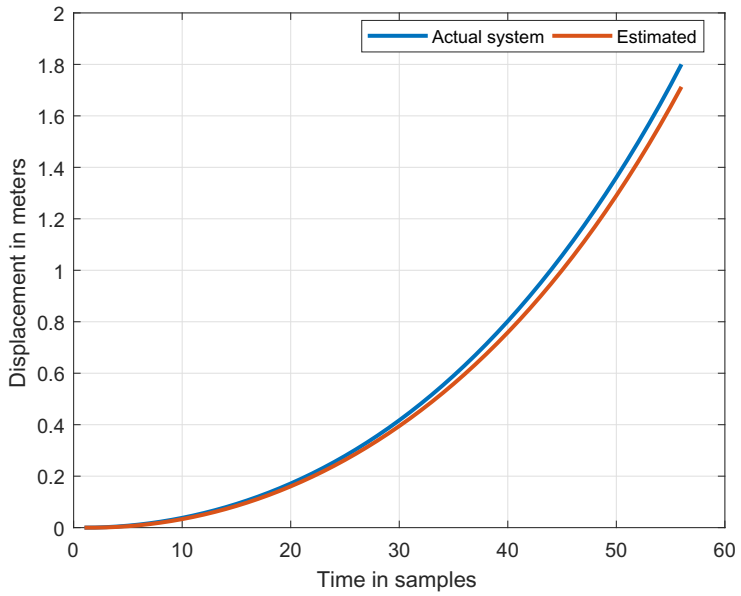

Source – From the author.

Thus, the estimation error, in this example, is $J_{LS} = 6.7\ cm$ being possible to conclude as a good estimation in the retractable mirror system.

Figure 45 – Error estimation.

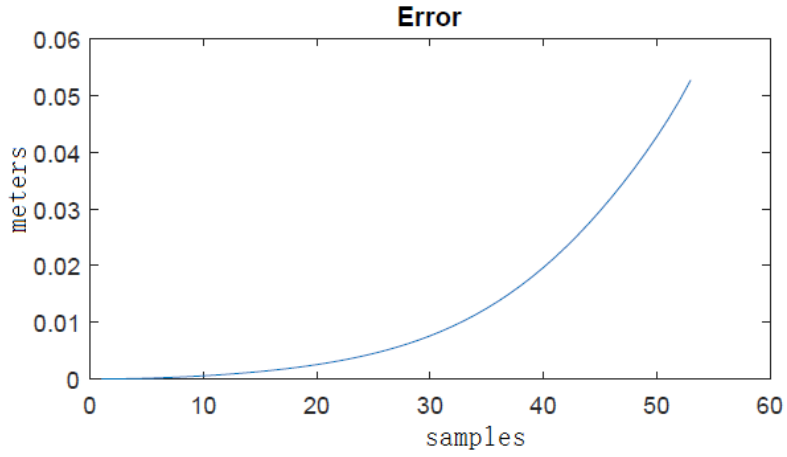

Source – From the author.

4.2 CONTROL STRATEGY

Figure 46 shows the feedback control technique scheme; there, it is possible to see one extra state η corresponding to the error integration.

Figure 46 – Standard robust control technique for SLE systems.

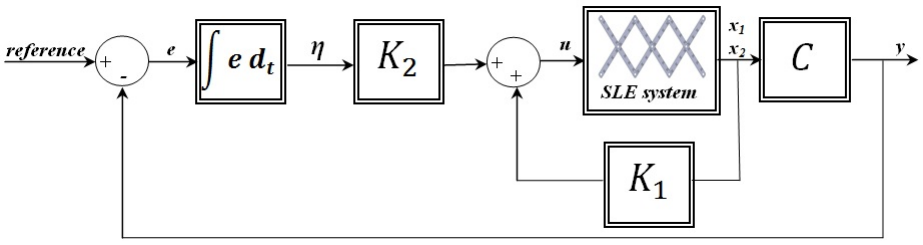

Source – From the author.

This augmented state will ensure zero steady-state error in the performance, so the state equation in (36), due to the augmented state now is rewritten as follows

$$\begin{aligned} \dot{x} &= Ax + Bu + Er \\ u &= Kx \end{aligned} \tag{44}$$

where

$$x = \begin{bmatrix} x_f \\ \eta \end{bmatrix}, \quad A = \begin{bmatrix} A_f & 0 \\ -C & 0 \end{bmatrix}, \quad B = \begin{bmatrix} B_f \\ 0 \end{bmatrix}, \quad E = \begin{bmatrix} 0 \\ I \end{bmatrix}, \quad K = \begin{bmatrix} K_1 & K_2 \end{bmatrix}.$$

In Equation (44), $C = \begin{bmatrix} 1 & 0 \end{bmatrix}$, r is the reference input, and I is an identity matrix. The following section defines the stability, stabilization and performance LMI conditions to set the robust control law.

4.3 ROBUST CONTROL TECHNIQUE

In this section, the strategy employed to set a robust controller of an SLE system based on the MSD model is described. Section 4.1 shows the identification technique and the system's parameters: mass m, spring constant k and viscous damping coefficient b. Thereby, an uncertain SLE assembly analogous could be considered, such as an MSD model with uncertain parameters k and b. The uncertain parameters are written as constraints in a polytope. Then, through LMI conditions, the polytopic system is controlled using $\mathbb{D}$-quadratic stabilization (EBIHARA et al., 2015).

4.3.1 Description of uncertainties in the polytope

The set $\Omega \in \mathbb{R}$ formed by all the possible values of the uncertain parameters k and b is limited in a polytope $\mathbb{E}^i$ where i is the number of vertices. Polytope is a hull

defined by V_i vertices, thus in Figure 47 it is depicted the four vertices $V_{1,..,4}$ formed from the combination of the upper (b_U, k_U) and lower (b_l, k_l) bounds of the uncertain coefficients k and b.

Let define $\Delta k_{max}, \Delta b_{max}, \Delta k_{min}, \Delta b_{min} \in \Omega$ the maximum and minimum variations of the uncertain parameters. From the polytope $\mathbb{E}^4$ we can determine

$$\begin{aligned} k_l < k < k_U \Rightarrow k + \Delta k_{max} = k_U; \quad k - \Delta k_{min} = k_l \\ b_l < b < b_U \Rightarrow b + \Delta b_{max} = b_U; \quad b - \Delta b_{min} = b_l. \end{aligned} \tag{45}$$

The variations of matrix A are expressed by

$$\begin{aligned} \Delta A^k_{min} = \begin{bmatrix} 0 & 0 & 0 \\ -\frac{\Delta k_{min}}{m} & 0 & 0 \\ 0 & 0 & 0 \end{bmatrix}; \quad \Delta A^k_{max} = \begin{bmatrix} 0 & 0 & 0 \\ \frac{\Delta k_{max}}{m} & 0 & 0 \\ 0 & 0 & 0 \end{bmatrix} \\ \Delta A^b_{min} = \begin{bmatrix} 0 & 0 & 0 \\ 0 & -\frac{\Delta b_{min}}{m} & 0 \\ 0 & 0 & 0 \end{bmatrix}; \quad \Delta A^b_{max} = \begin{bmatrix} 0 & 0 & 0 \\ 0 & \frac{\Delta b_{max}}{m} & 0 \\ 0 & 0 & 0 \end{bmatrix}. \end{aligned} \tag{46}$$

Figure 47 – Polytope of uncertain parameters k and b.

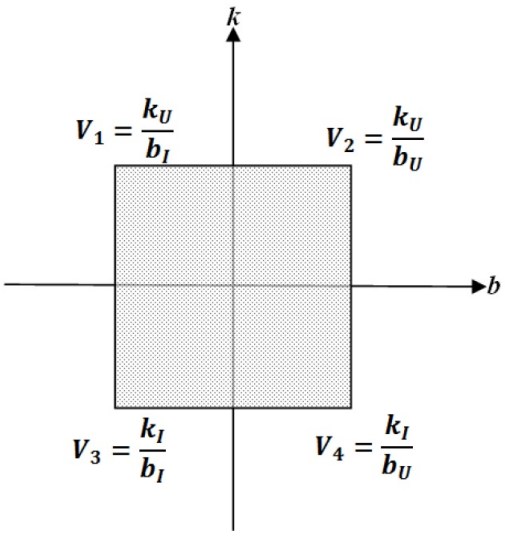

Source – From the author.

Now it can be defined the $A(V_i)$ matrix for each vertex of $\mathbb{E}^4$ in Figure 47 as follows

$$\begin{aligned} A(V_1) &= A + \Delta A^k_{max} + \Delta A^b_{min} \\ A(V_2) &= A + \Delta A^k_{max} + \Delta A^b_{max} \\ A(V_3) &= A + \Delta A^k_{min} + \Delta A^b_{min} \\ A(V_4) &= A + \Delta A^k_{min} + \Delta A^b_{max} \end{aligned} \tag{47}$$

From Equation (47) and employing the notation from (EBIHARA et al., 2015) it can be defined the hull of the polytope like

$$conv(A) := \left\{ \sum_{j=1}^{4} \Omega_j A^j \right\}. \tag{48}$$

Since Ω is linear time invariant (LTI), the model described in Equation (48) can be represented like a linear matrix valued function $A(\cdot) : \mathbb{R}^i \rightarrow \mathbb{R}^{n \times n}$ given by

$$A(\Omega) = \sum_{j=1}^{4} \Omega_j A^j \tag{49}$$

4.3.2 LMI conditions for stability and stabilization

The controller presented in this Chapter intends to obtain a desired performance from the SLE system. One possibility to achieve this goal is by allocating the poles in arbitrary regions through a feedback loop. The sequel will introduce stability and stabilization LMI conditions to design the control law.

Theorem 4.1

For a given Lyapunov function $\mathcal{V}(x) = x^T P x$ where $P \in \mathbb{S}^n$ and $\mathbb{S}^n$ stands for the field of real symmetric $n \times n$ matrices. An LTI system governed by the differential equation $\dot{x} = Ax, x(0) = 0$, is asymptotically stable if there exists $\mathcal{V}(x) > 0, \forall x \neq 0$ such that $\dot{\mathcal{V}} = x^T(A^T P + PA)x < 0$.

Proof

Let define an eigenvector ξ of A, with its corresponding eigenvalue $\lambda \in \mathbb{C}$ where $\mathbb{C}$ stands for the field of complex numbers. Then it can be held that $A\xi = \lambda\xi$, if $A^T P + PA < 0$ holds, then it is possible to affirm

$$\xi^*(A^T P + PA)\xi < 0$$

where ξ^* is the complex conjugate transpose of ξ, the above inequality implies

$$(\lambda + \lambda^*)\xi^* P \xi < 0.$$

Since $P > 0$, then $\xi^* P \xi > 0$; the condition above holds if $\lambda + \lambda^* < 0$, it means that the eigenvalue of A is in the negative complex plane $\mathbb{C}^-$, so the system is asymptotically stable.

Note that Theorem 4.1 does not hold for an uncertain system, then it is necessary to recall the next Theorem.

Theorem 4.2

The LTI uncertain system $\dot{x} = A(\Omega)x$ is asymptotically stable for all $\Omega \in \mathbb{E}^4$ if there exists $P \in \mathbb{S}^n$ such that

$$P > 0, \quad PA_j + A_j^T P < 0 \qquad (j = 1, .., 4) \tag{50}$$

Proof

Suppose that Equation (50) holds; so, for any $\Omega \in \mathbb{E}^4$:

$$P > 0, \qquad \sum_{j=1}^{4} \Omega_j (PA_j + A_j^T P) < 0$$

equivalent to

$$P > 0, \quad PA(\Omega) + A(\Omega)^T P < 0.$$

From the above inequality and Theorem 4.1, it can be concluded that the uncertain LTI system $\dot{x} = A(\Omega)x$ is stable for all Ω.
The next definition introduces the concept of $\mathbb{D}$-stability, which is a generalization of asymptotic stability.

Definition 4.1

Let $\mathbb{D}$ be a domain on the left complex plane, which is symmetric about the real axis. Then, a matrix $A \in \mathbb{R}^{n \times n}$ is defined such $\mathbb{D}$-stable if:

$$\lambda_i(A) \in \mathbb{D}, \quad i = 1, 2, \ldots, n.$$

Definition 4.2

A $\mathbb{D}$-region on the complex plane is called an LMI region if there exist matrices $L = L^T \in \mathbb{R}^{n \times n}$ and $M \in \mathbb{R}^{n \times n}$ such that

$$\mathbb{D}_{LM} = \left\{ s = \sigma + j\omega | \quad s \in \mathbb{C}, \quad L + sM + s^* M^T < 0 \right\},$$

where σ is the real and ω the imaginary part of s. The characteristic function of $\mathbb{D}_{LM}$ is

$$F_{\mathbb{D}}(s) = L + sM + s^* M^T.$$

Proposition 4.1

The set of elements $s \in \mathbb{D}_{LM}$ is convex.

Proof

Let allocate any two elements $s_{1,2}$ in convexity conditions

$$s = \Omega s_1 + (1-\Omega)s_2, \qquad 0 \leq \Omega \leq 1,$$

by definition

$$L + s_1 M + s_1^* M^T < 0, \qquad L + s_2 M + s_2^* M^T < 0,$$

from the last expressions, it can be held that

$$\begin{aligned} L + sM + s^* M^T =& L + (\Omega s_1 + (1-\Omega)s_2)M + (\Omega s_1^* + (1-\Omega)s_2^*)M^T \\ =& L + \Omega s_1 M + \Omega s_1^* M^T + (1-\Omega)s_2 M + (1-\Omega)s_2^* M^T \\ =& \Omega(L + s_1 M + s_1^* M^T) + (1-\Omega)(L + s_2 M + s_2^* M^T) \\ <& 0, \quad \forall 0 \leq \Omega \leq 1. \end{aligned}$$

Arbitrary poles allocation in $\mathbb{D}_{LM}$ allows getting a desired performance in the feedback systems. Many times it is necessary to intersect two $\mathbb{D}_{LM}$, then the next Proposition is necessary.

Proposition 4.2

Two given characteristic functions $F_{\mathbb{D}_{1,2}}(s)$ with LMI regions $\mathbb{D}_{LM_{1,2}}$, can be intersected in a new convex LMI region $\mathbb{D}_{LM} = \mathbb{D}_{LM_1} \cap \mathbb{D}_{LM_2}$ with a characteristic function

$$F_{\mathbb{D}_{LM}} = diag(F_{\mathbb{D}_1}, F_{\mathbb{D}_2}).$$

Proof

From the given conditions follows that

$$\mathbb{D}_{LM_1} = \left\{ s | \quad F_{\mathbb{D}_{LM1}}(s) < 0 \right\}, \quad \mathbb{D}_{LM_2} = \left\{ s | \quad F_{\mathbb{D}_{LM2}}(s) < 0 \right\},$$

and

$$\begin{aligned} \mathbb{D}_{LM} =& \mathbb{D}_{LM_1} \cap \mathbb{D}_{LM_2} \\ =& \left\{ s | \quad F_{\mathbb{D}_{LM1}}(s) < 0, \quad s | \quad F_{\mathbb{D}_{LM2}}(s) < 0 \right\} \\ =& \left\{ s | \quad diag\left(F_{\mathbb{D}_{LM1}}(s), F_{\mathbb{D}_{LM2}}(s) \right) < 0 \right\}. \end{aligned}$$

Theorem 4.3

Let $\mathbb{D}_{LM}$ be a convex LMI region with a characteristic function $F_{\mathbb{D}}(s) = L + sM + s^* M^T$, then a matrix $A \in \mathbb{R}^{n \times n}$ is $\mathbb{D}$-stable if there exists a symmetric positive definite matrix P such that

$$\Gamma_{\mathbb{D}} = L \otimes P + M \otimes (AP) + M^T \otimes (AP)^T < 0$$

where $\otimes$ is the Kronecker product.
The proof of Theorem 4.3 is too lengthy; however, a compact proof can be found in (MAHMOUD, C., 1996).

Lemma 4.1

A matrix $A \in \mathbb{R}^{n\times n}$ is $\mathbb{D}_{LM_{1,2}}$-stable if there exists a positive definite matrix P such that $\Gamma_{\mathbb{D}_{1,2}} < 0$.

Proof

Let define the associated characteristic functions of the LMI regions $\mathbb{D}_{LM_{1,2}}$ as follows

$$F_{D_{LM1}} = L + s_1 M + s_1^* M^T, \qquad F_{D_{LM2}} = L + s_2 M + s_2^* M^T.$$

Based on Proposition 4.2, the characteristic function of the LMI region $\mathbb{D}_{LM} = \mathbb{D}_{LM_1} \cap \mathbb{D}_{LM_2}$ can be represented by

$$F_{\mathbb{D}_{LM}} = diag(F_{\mathbb{D}_1}, F_{\mathbb{D}_2}) = L + sM + s^* M^T,$$

with

$$L = diag(L_1, L_2), \quad M = diag(M_1, M_2).$$

Then

$$\begin{aligned}
\Gamma_D =& L \otimes P + M \otimes (AP) + M^T \otimes (AP)^T \\
=& diag(L_1, L_2) \otimes P + diag(M_1, M_2) \otimes (AP) + diag(M_1, M_2)^T \otimes (AP)^T \\
=& diag\Big(L_1 \otimes P + M_1 \otimes (AP) + M_1^T \otimes (AP)^T, \\
& L_2 \otimes P + M_2 \otimes (AP) + M_2^T \otimes (AP)^T\Big) \\
=& diag(\Gamma_{D_{LM1}}, \Gamma_{D_{LM2}})
\end{aligned}$$

which means

$$\Gamma_D < 0 \Leftrightarrow \Gamma_{\mathbb{D}_{LM1}} < 0 \quad and \quad \Gamma_{\mathbb{D}_{LM2}} < 0.$$

Proposition 4.3

The matrix $A \in \mathbb{R}^{n\times n}$ is $\mathbb{D}^{\alpha,\beta}$-stable if there exists a matrix P satisfying

$$\begin{aligned}
P &> 0 \\
A^T P + PA + 2\alpha P &< 0 \\
A^T P + PA + 2\beta P &> 0.
\end{aligned} \tag{51}$$

Being the poles allocated according to Figure 48.a. In Equation 51 $\beta < \alpha$.

Proof

Let $s = \sigma + j\omega \in \mathbb{D}_{LM}^{\alpha,\beta}$, then the necessity to prove Proposition 4.3 is $\sigma < -\alpha$ and $\sigma > -\beta$. From the second LMI from Equation (51) based on Theorem 4.3: $L = 2\alpha$ and

$M = 1$, then by definition:

$$\begin{aligned} 2\alpha + s + s^* &< 0 \\ 2\alpha + \sigma + j\omega + \sigma - j\omega &< 0 \\ 2\alpha + 2\sigma &< 0 \\ \sigma &< -\alpha \end{aligned}$$

Figure 48 – $\mathbb{D}$-stability: poles allocation.

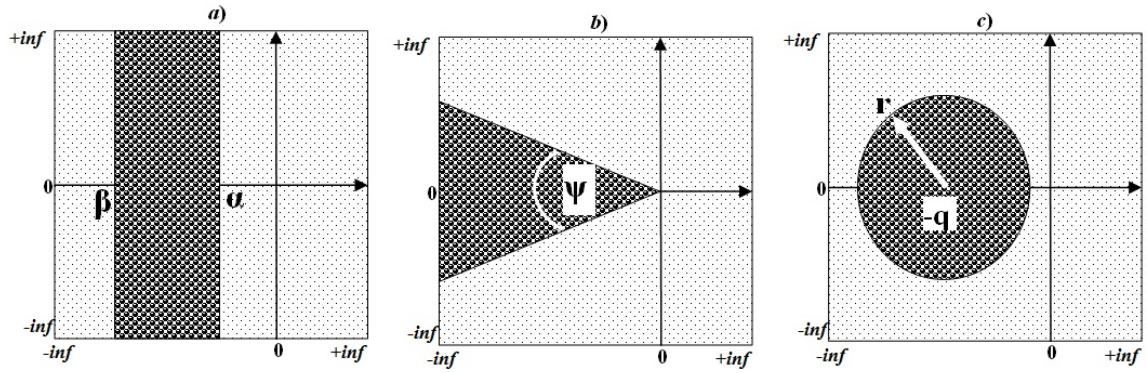

Source – From the author.

From the third line of Equation (51): $L = -2\beta$ and $M = -1$, then by definition:

$$\begin{aligned} -2\beta - s - s^* &< 0 \\ -2\beta - \sigma - j\omega - \sigma + j\omega &< 0 \\ -2\beta - 2\sigma &< 0 \\ \sigma &> -\beta \end{aligned}$$

Proposition 4.4

The matrix $A \in \mathbb{R}^{n\times n}$ is $\mathbb{D}^{\Psi}$-stable if the LMI conditions in Equation (52) are satisfied :

$$\begin{gathered} P > 0 \\ \begin{bmatrix} (PA + A^T P)\sin\frac{\Psi}{2} & (PA - A^T P)\cos\frac{\Psi}{2} \\ (A^T P - PA)\cos\frac{\Psi}{2} & (PA + A^T P)\sin\frac{\Psi}{2} \end{bmatrix} < 0. \end{gathered} \tag{52}$$

Being the poles allocated according to Figure 48.b.

Proof

Let $s = \sigma + j\omega \in \mathbb{D}^{\Psi}_{LM}$, then the necessity to prove Proposition 4.4 is $|\omega| < -\sigma\tan\frac{\Psi}{2}$. From the second LMI from Equation (52) based on Theorem 4.3 it can be held

that $L = 0$ and $M = \begin{bmatrix} \sin\frac{\psi}{2} & \cos\frac{\psi}{2} \\ -\cos\frac{\psi}{2} & \sin\frac{\psi}{2} \end{bmatrix}$, then by definition:

$$\begin{aligned}
s\begin{bmatrix} \sin\frac{\psi}{2} & \cos\frac{\psi}{2} \\ -\cos\frac{\psi}{2} & \sin\frac{\psi}{2} \end{bmatrix} + s^*\begin{bmatrix} \sin\frac{\psi}{2} & -\cos\frac{\psi}{2} \\ \cos\frac{\psi}{2} & \sin\frac{\psi}{2} \end{bmatrix} &< 0 \\
\begin{bmatrix} (s+s^*)\sin\frac{\psi}{2} & (s-s^*)\cos\frac{\psi}{2} \\ (-s+s^*)\cos\frac{\psi}{2} & (s+s^*)\sin\frac{\psi}{2} \end{bmatrix} &< 0 \\
\begin{bmatrix} \sigma\sin\frac{\psi}{2} & j\omega\cos\frac{\psi}{2} \\ -j\omega\cos\frac{\psi}{2} & \sigma\sin\frac{\psi}{2} \end{bmatrix} &< 0 \\
\omega^2 cos^2\tfrac{\psi}{2} < \sigma^2 sin^2\tfrac{\psi}{2}, \sigma\sin\tfrac{\psi}{2} &< 0 \\
\omega^2 < \sigma^2 tan^2\tfrac{\psi}{2}, \sigma\tan\tfrac{\psi}{2} &< 0 \\
|\omega| < -\sigma\tan\tfrac{\psi}{2}
\end{aligned}$$

Proposition 4.5

The matrix $A \in \mathbb{R}^{n\times n}$ is $\mathbb{D}^{r,q}$-stable if there exists a matrix P satisfying

$$\begin{aligned}
P &> 0 \\
\begin{bmatrix} -rP & qP + PA \\ qP + A^T P & -rP \end{bmatrix} &< 0,
\end{aligned} \tag{53}$$

with the poles allocated according to Figure 48.c.

Proof

Let $s = \sigma + j\omega \in \mathbb{D}^{r,q}_{LM}$, then the necessity to prove Proposition 4.5 is $(\sigma+q)^2+\omega^2 < r^2$. From the second LMI from (53) based on Theorem 4.3: $L = \begin{bmatrix} -r & q \\ q & -r \end{bmatrix}$, $M = \begin{bmatrix} 0 & 1 \\ 0 & 0 \end{bmatrix}$, now by definition:

$$\begin{aligned}
\begin{bmatrix} -r & q \\ q & -r \end{bmatrix} + s\begin{bmatrix} 0 & 1 \\ 0 & 0 \end{bmatrix} + s^*\begin{bmatrix} 0 & 0 \\ 1 & 0 \end{bmatrix} &< 0 \\
\begin{bmatrix} -r & s+q \\ s^*+q & -r \end{bmatrix} &< 0 \\
(s+q)(s^*+q) &< r^2 \\
(\sigma+q)^2 + \omega^2 &< r^2
\end{aligned}$$

4.3.3 Stabilization

This subsection aims to find a fixed state feedback $u = Kx$ to stabilize the uncertain system $A(\Omega)$ and arbitrary performance. The closed-loop uncertain system is defined as follows:

$$\dot{x} = A_C(\Omega)x, \qquad \Omega \in \mathbb{E}^4 \tag{54}$$

with

$$A_c(\Omega) = A(\Omega) + BK.$$

In the remaining of this subsection, LMI conditions based on the results depicted in the last subsections are presented to find the feedback gain as mentioned earlier.

Theorem 4.4

The feedback system $A_c(\Omega)$ with gain $u = Kx$ is asymptotically stable if there exists a positive semi-definite matrix Q and W satisfying

$$A(\Omega)Q + QA^T(\Omega) + BW + W^TB^T < 0$$

where $K = WQ^{-1}$.

Proof

Theorem 4.2 establishes that

$$(A(\Omega) + BK)^TP + P(A(\Omega) + BK) < 0,$$

now, let multiply both sides by $Q = P^{-1}$

$$QA^T(\Omega)PQ + QK^TB^TPQ + QPA(\Omega)Q + QPBKQ < 0,$$

let define a new variable $W = KQ$ giving

$$QA^T(\Omega) + W^TB^T + A(\Omega)Q + BW < 0.$$

From Propositions 4.2, 4.3, 4.4 and 4.5, the next corollary can be formulated.

Corollary 4.1

If there exists a symmetric positive definite matrix Q and a matrix W satisfying the following conditions

$$\begin{aligned}
A(\Omega)Q + QA^T(\Omega) + BW + W^TB^T + 2\alpha Q &< 0,\\
A(\Omega)Q + QA^T(\Omega) + BW + W^TB^T + 2\beta Q &> 0,\\
\begin{bmatrix} -rQ & qQ + A(\Omega)Q + BW \\ qQ + QA(\Omega)^T + W^TB^T & -rQ \end{bmatrix} &< 0,\\
\begin{bmatrix} \xi_1(\Omega)\sin\frac{\psi}{2} & \xi_2(\Omega)\cos\frac{\psi}{2} \\ \xi_2^T(\Omega)\cos\frac{\psi}{2} & \xi_1(\Omega)\sin\frac{\psi}{2} \end{bmatrix} &< 0
\end{aligned}$$

with

$$\begin{aligned}
\xi_1(\Omega) &= A(\Omega)Q + QA(\Omega)^T + BW + W^TB^T,\\
\xi_2(\Omega) &= A(\Omega)Q - QA(\Omega)^T + BW - W^TB^T
\end{aligned}$$

then, the LTI uncertain closed-loop system $A_c(\Omega)$ with gain $K = WQ^{-1}$, becomes $\mathbb{D}^{SLE}$-stable for any initial condition $x_o \in \mathbb{R}$.

Proof

In Theorem 4.2 it was proven that LTI uncertain system was affined with LTI certain system, both hold stability properties. Thus, in Equation (51) let replace A with $A_c(\Omega)$, so it can be held that

$$(A(\Omega) + BK)^T P + P(A(\Omega) + BK) + 2\alpha P < 0,$$

since $K = WP$, the expression above turns non linear in P. Let multiply either side by $Q = P^{-1}$ as follows

$$QA^T(\Omega)PQ + QK^T B^T PQ + QPA(\Omega)Q + QPBKQ + 2\alpha QPQ < 0.$$

This new inequality remains nonlinear, then let define a second new variable $W = KQ$. This gives

$$QA^T(\Omega) + W^T B^T + A(\Omega)Q + BW + 2\alpha Q < 0.$$

Now the expression above is an LMI. From W it is possible to recover the gain $K = WQ^{-1}$. The same variable replacement can be done in the remaining LMI condition as follows

$$\begin{aligned}
(A(\Omega) + BK)^T P + P(A(\Omega) + BK) + 2\beta P &>0,\\
QA^T(\Omega)PQ + QK^T B^T PQ + QPA(\Omega)Q + QPBKQ + 2\beta QPQ &>0,\\
QA^T(\Omega) + W^T B^T + A(\Omega)Q + BW + 2\beta Q &>0.
\end{aligned}$$

Similarly, let introduce in Equation (53) the variables replacement as follows

$$\begin{aligned}
\begin{bmatrix} -rP & qP + PA \\ qP + A^T P & -rP \end{bmatrix} &<0,\\
\begin{bmatrix} -rP & qP + P(A(\Omega) + BK) \\ qP + (A(\Omega) + BK)^T P & -rP \end{bmatrix} &<0,\\
\begin{bmatrix} -rQ & qQ + QPA(\Omega)Q + QPBKQ \\ qQ + QA^T(\Omega)PQ + QK^T B^T PQ & -rQ \end{bmatrix} &<0,\\
\begin{bmatrix} -rQ & qQ + A(\Omega)Q + BW \\ qQ + QA^T(\Omega) + W^T B^T & -rQ \end{bmatrix} &<0.
\end{aligned}$$

Finally, let develop the same procedure in Equation (52):

$$PA + A^T P = \xi_1'(\Omega) \quad ; \quad PA - A^T P = \xi_2'(\Omega),$$

by replacing variables:

$$\begin{aligned}
P(A(\Omega) + BK) + (A(\Omega) + BK)^T P &= \xi_1'(\Omega)\\
QPA(\Omega)Q + QPBKQ + QA^T(\Omega)PQ + QK^T B^T PQ &=\\
A(\Omega)Q + BW + QA^T(\Omega) + W^T B^T &= \xi_1(\Omega),
\end{aligned}$$

and

$$\begin{aligned}
P(A(\Omega) + BK) - (A(\Omega) + BK)^T P &= \xi_2'(\Omega)\\
QPA(\Omega)Q + QPBKQ - QA^T(\Omega)PQ - QK^T B^T PQ &=\\
A(\Omega)Q + BW - QA^T(\Omega) - W^T B^T &= \xi_2(\Omega).
\end{aligned}$$

4.4 PRACTICAL APPLICATIONS

The LMI conditions presented in Corollary 4.1 can be set to obtain stabilization besides desired performance such as overshoot, settling time, rising time among other performance parameters. Note that depending on performance requirements, it is not always necessary to use all the LMI conditions as illustrated in the practical applications presented below. This research intends to offer a standard procedure to control the SLE based system. Besides asymptotic stabilization, arbitrary performance will be stated too. SLE systems have plenty of joints, so it is impossible to warrant constant friction parameters for each joint, thereby being considered an uncertain system.

This section presents three examples of SLE systems where the technique shown in this Chapter is applied. The simulations and animations of SLE systems were developed by using Simscape-Simulink. Unlike other Simulink blocks representing mathematical operations or operating on signals, Simscape blocks represent physical components or relationships directly being possible to configure mass, inertia, friction, and other dynamic forces. Proposition 4.1 proves that the LMI conditions operate under convex conditions. Therefore, CVX (GRANT et al., 2008) can be used, a convex programming Matlab software. The first step of this technique is to identify the parameters of the system employing an MSD model. The parameters to be identified are the mass (m), spring and damper coefficients (k, b).

Table 3 – Identified parameters and uncertainties.

	Mass [g]	Damper coef. (b)[g/s]	Spring coef. (k)[g/s^2]	Δb [%]	Δk [%]
Mirror	994.95	240.56	24.07	20	15
Window	19.4628	19.6575	6.2184	10	10
Roof	9.7371	0.0834	1.11	14	17

Source – From the author.

Due to lubrication in the joints, stiffness of the bars, vibrations among others the system can operate in an uncertain range which is expressed in the MSD model like uncertainties in b and k. In Table 3, by employing Equation (42), the parameters for each application are calculated. There, Δb and Δk come from the uncertain kinetic friction coefficients, expressed like uncertain b and uncertain k in the MSD model.

4.4.1 Retractable mirror

The retractable mirror, shown in Figure 49, was designed to avoid the need of huge mirrors. The user can move in front of the mirror, following the user by employing an optical sensor. Based on the classification presented in Chapter 2, the folding structure is a heterogeneous assembly formed by translational units. In this case, it is used a linear actuator with maximum range of 0.15 meters as depicted in Figure 49.

Figure 49 – Retractable mirror: a) folding condition b) deploying condition.

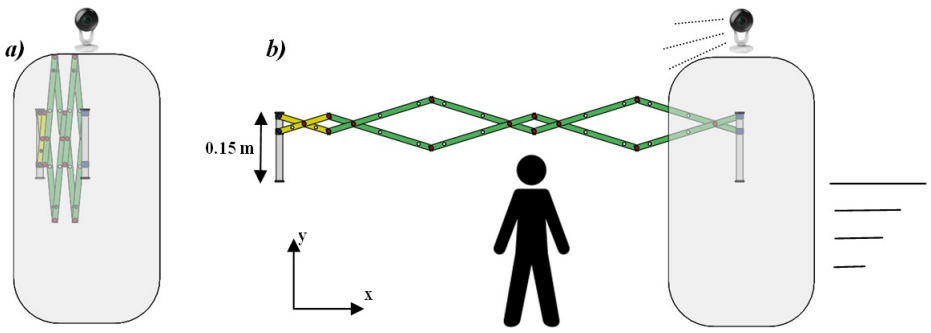

Source – From the author.

The maximum displacement in x – *axis* of the mirror is 1.6 meters. Note that there are 19 joints in this system. Because of lubrication, by identification, it is computed that the kinematic friction $\mu_d[Ns/m]$ oscillates between $0.05 < \mu_d < 0.2$ in the joints. Under the supposition that the user in front of the mirror is not going to run, a settling time (t_s) less than 3 seconds is defined. An overshoot $Mp < 5\%$ is specified to avoid vibration due to abrupt stops. The following subsection presents a solution to achieve the requirements described in this subsection based on the control strategy presented in this Chapter.

4.4.1.1 Results

To achieve the performance for the retractable mirror $t_s < 3s$, the formula $\sigma = 4/t_s$ can be used, and $\sigma < 1.33$ can be computed, which means $\alpha = 1.33$ according to Figure 48 of $\mathbb{D}$-stability. Then, to achieve a maximum overshoot of $Mp < 5\%$, the expression below can be used

$$\zeta = \frac{-\ln(Mp/100)}{\sqrt{\pi^2 + \ln(Mp/100)^2}}, \tag{55}$$

giving a damping ratio $\zeta = 0.69$. Based on $\mathbb{D}$-stability it is calculated $\psi/2 = \cos^{-1}\zeta = 0.8$ rad. Let set $\alpha = 1.33$ and $\psi/2 = 0.8$ rad in the LMI conditions of Corollary 4.1. A performance comparison of Lyapunov stabilization with $\mathbb{D}^{SLE}$-stabilization is depicted in Figure 50. In Figure 50, the axis represent the horizontal displacement in meters and the time in seconds.

Note 1

In Proposition 4.2 it was shown that two LMI regions $\mathbb{D}_{LM1,2}$ can be intersected in a new convex LMI region. Aiming to obtain feasible solutions in the LMI conditions, it is important to avoid the location of poles in null-sets. For example, if it is set $r = 2$, $q = 3$, $\alpha = 6$, $\beta = 10$ in Corollary 4.1, then the intersection of both regions: the circular

one with center in $q = -3$ and radius $r = 2$, and the region defined between $\alpha = 6$ and $\beta = 10$ on the plane $\mathbb{C}$, is going to lead into a null-set. In summary, if $\mathbb{D}_{LMi} \cap \mathbb{D}_{LMj} = \varnothing$ in Corollary 4.1, then a infeasible solution will be obtained. Besides, it is possible to get infeasible solutions by setting extreme performance in the SLE system. For example, if the retractable mirror is set a settling time of $50ms$ instead of $3s$, then the CVX solver will return an unfeasible solution warning.

Figure 50 – Retractable mirror performance.

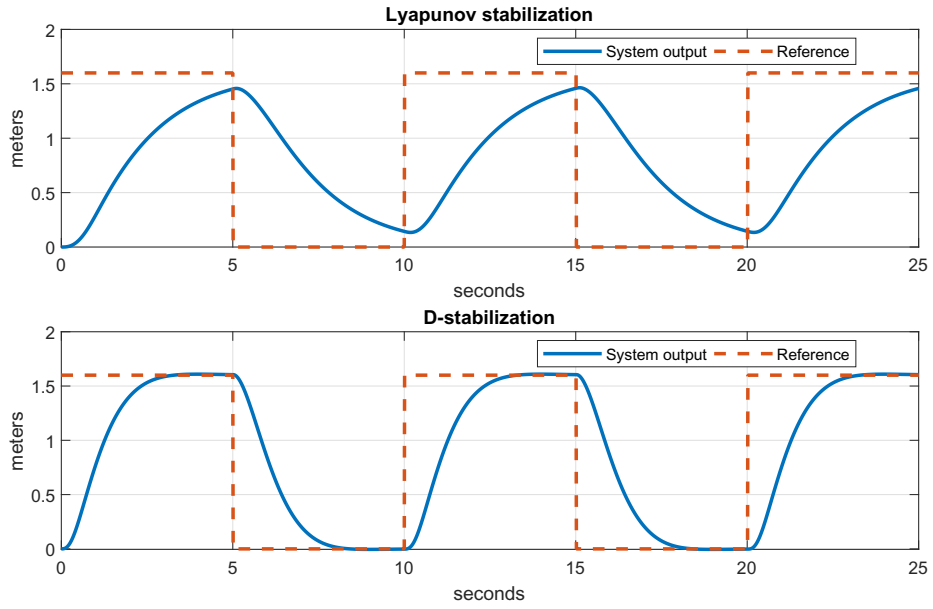

Source – From the author.

Note 2

In the retractable mirror example, if it is desired to obtain a faster response, it is necessary to recalculate the tuning parameters in terms of settling time. For example, instead of 3 seconds in the desired settling time, it can be defined 2 or 1 second. The procedure presented in the last subsection can be computed $\alpha = 2$ and $\alpha = 4$ for 2 and 1 second, respectively. In Figure 51 it is plotted the performances of the retractable mirror based on different tuning parameters. Of course, the response turns faster; on the other hand, the overshoot increases too. Note that this could lead to abrupt vibrations in the case of the mirror. The tuning parameters in the practical applications presented in this Chapter can be recalculated to achieve different performances on the condition that a feasible solution can be computed.

Figure 51 – Performance comparison based on different tuning parameters.

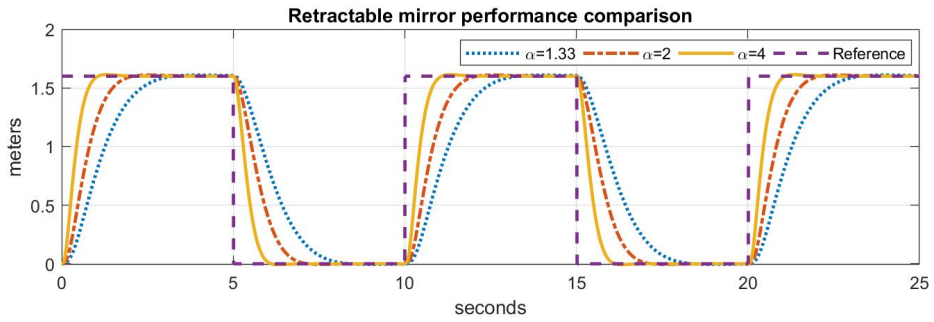

Source – From the author.

4.4.2 Intelligent window

This window is designed to operate according to the sunlight intensity measured by a light sensor. In this case, a rotatory actuator could be employed which could be a DC motor. In the last case were employed translational SLE units. In this case, the assembly is composed of angulated SLE. This kind of SLE assemblies can form closed mobile structures (YOU, Z., 2011), as depicted in Figure 52.

Figure 52 – Intelligent window a.open b.middle c. closed position.

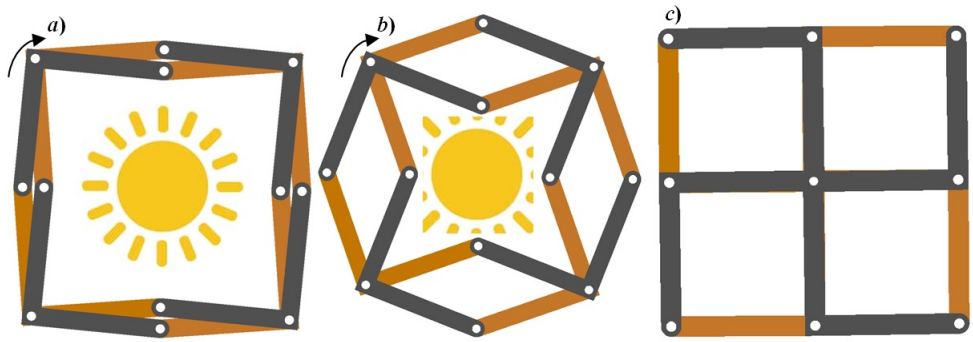

Source – From the author.

The dimension of the square window in the closed position (Figure 52.c) is 15 centimeters per side. This assembly has 12 revolute joints, which operate with a dynamic friction coefficient equal to 0.01 considering lubricated joints. Due to constant use or lack of lubrication, the coefficient increase up to 0.1. Thus it is held that $0.01 < \mu_d < 0.1$. Under the fact that there are no abrupt changes in weather, the desired performance is to have a settling time t_s in the range $0.6 < t_s < 2$. The overshoot is not a constraint however it is important to avoid high peaks.

4.4.2.1 Results

The performance desired for the intelligent window is to get a t_s between 0.6 and 2 seconds. Two ways can achieve this performance: the first one is by allocating the poles between α and β, the second one is by allocating the poles in a circle with center in $-q$ and radius r (see Figure 48). Aiming to avoid a high overshoot, let use the circle. By employing the formula $\sigma = 4/t_s$ it is held that $6 > \sigma > 2$ which can be interpreted like a circle with center in $q = 4$ and radius $r = 2$. The desired performance and a comparison with conventional Lyapunov stabilization can be analyzed in Figure 53 where the axis represent the percentage of light blocked by the window and the time in seconds.

Figure 53 – Intelligent window performance.

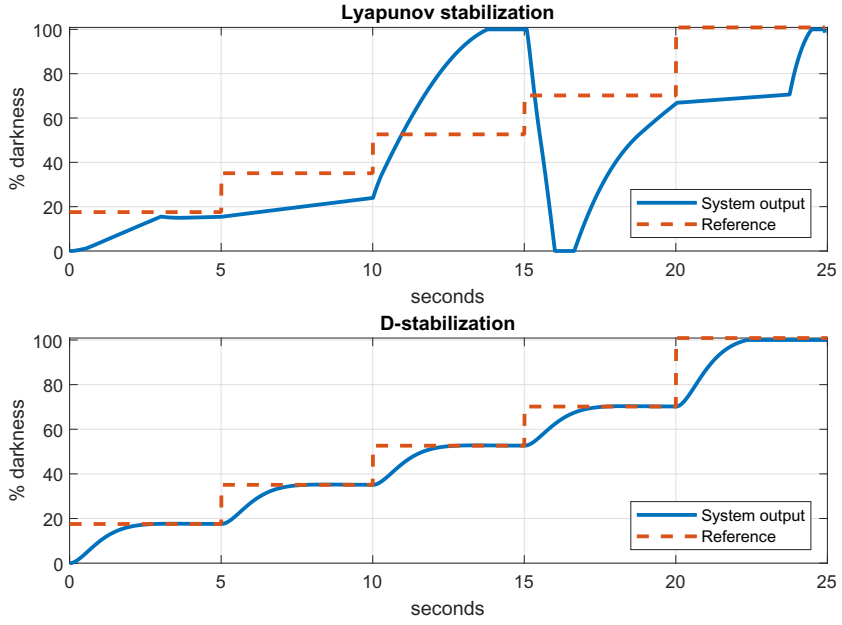

Source – From the author.

4.4.3 Folding roof

This mechanism (see Figure 30) can be employed in cars, motorcycles, bikes and residential applications, such as a balcony, a pool, or a playground. This structure has 14 joints operating with a friction coefficient in the range of $0.2 < \mu_d < 0.4$. The desired performance, in this case, is set with a settling time in the range $1 < t_s < 2$ s and a maximum overshoot of $Mp < 3\%$.

4.4.3.1 Results

To achieve the previously specified performance by the folding roof, let use the formula $\sigma = 4/t_s$; thus $\alpha = 2$ and $\beta = 4$ can be computed. Then, by replacing the overshoot of $Mp = 3\%$ in Equation (55), $\zeta = 0.744$ and $\psi/2 = 0.736rad$ can be calculated. Let replace these values in the LMI conditions of Corollary 4.1. The roof performance and a comparison with Lyapunov conventional stabilization approach (Theorem 4.4) are presented in Figure 54. The axis represent the percentage of the closure in the folding roof and the time in seconds.

Figure 54 – Retractable roof performance.

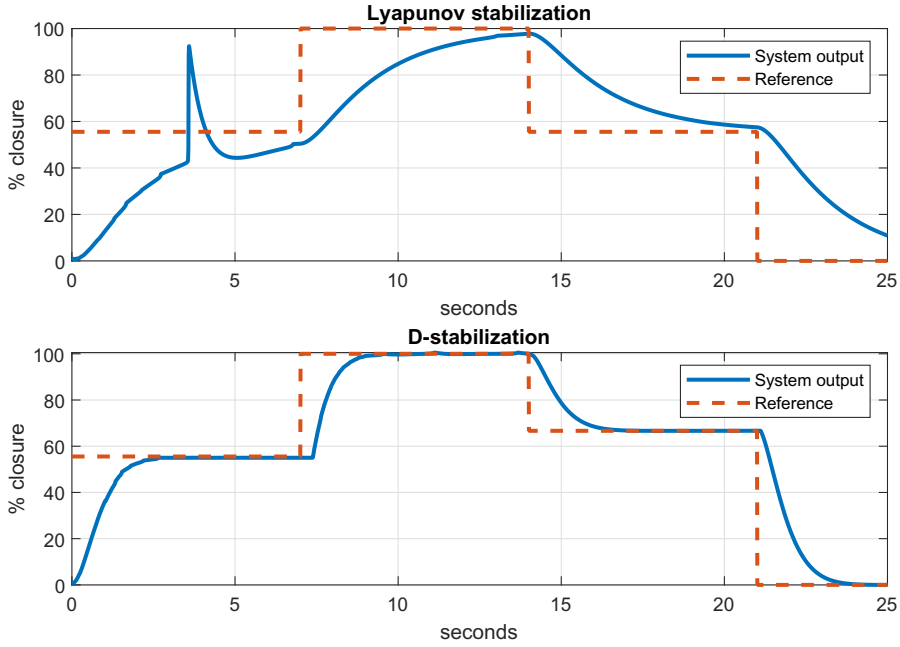

Source – From the author.

A summary of the tuning parameters set in Corollary 4.1 of the three examples presented before is depicted in Table 4.

Table 4 – Tuning parameters in $\mathbb{D}^{SLE}$-stabilization approach.

	α	β	r	q	$\phi/2$ [rad]
Mirror	1.33	-	-	-	0.8
Window	-	-	2	4	-
Roof	2	4	-	-	0.736

Source – From the author.

4.4.4 SLO control - example

In this subsection, the SLO system of Figure 38 is controlled using the approaches presented above. The dimensions of the structure are borrowed from the Example of Paragraph 3.2.1.1.1. The simulation to identify the parameters of the SLO systems, as well as its control, was developed using Simscape-Simulink. The identified parameters from the simulation are m = 127.3 g, k = 2.15 g/s^2, and b = –29.7 g/s. The states equation can be obtained replacing the identified parameters, m, k and b, in Equation (36). Then, Corollary 4.1 is used to stabilize and define an arbitrary performance in the SLO system. The resulting performance of the SLO system can be seen in Figure 55.

Figure 55 – Control of SLO composed by translational SLE with constatnt bar length, and gate and guide perpendicular.

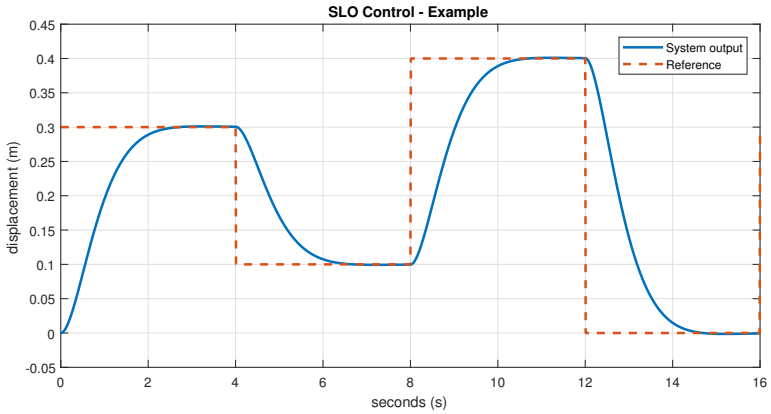

Source – From the author.

The tuning of the controller was performed locating the poles, from the feedback system, in a circle with center in –6 and radius equal to 4 on the S–plane according to the Figure 48.c.

4.5 CHAPTER CONCLUSION

The robust control strategy presented in this chapter can be applied in any SLE based system, ensuring stabilization and zero steady-state error. The robustness of this approach reduces the uncertainties influence of dynamic forces as friction in the joints. Moreover, by allocating the poles in arbitrary regions, defining the desired performance can be considered one extra DoF to design the controller.

5 CONSTRAINTS ON CONTROL AND PERFORMANCE OF SLE BASED SYSTEM USING MPC

This chapter addresses the use of model predictive control (MPC) to deal with some of the constraints that must be considered in stabilizing the SLE-based system. Failure to consider limitations on actuators can cause instability or poor performance. Deployable structures can exhibit singularities in their motion. SLE is not an exception; hence, this approach offers an alternative to avoid singularities and collisions. In addition, this approach can restrict the deployment movement of the system being possible to establish a monotonic ascending or descending behavior. Almost all physical dynamical systems in real-life work under constraints or limitations (JUNGERS, 2008; FENG, 2018). At the same time, many feedback controllers are designed under unlimited signal conditions, omitting the technical specification of the hardware such as power saturation, the slew rate of force, sensor range, delays, among others (TARBOURIECH, 2011; DOS SANTOS; CONCEICAO, 2013). This carelessness can lead to poor performance or instability (TANAKA, 2004; GRIJALVA, 2017). Another omission of controllers is the restriction on the process dynamics due to aesthetics, safety, singularities or constructive reasons. Two folding domotic devices: a lamp (as shown in Figure 16) and a chair (see Figure 57) are used to test the presented method.

5.1 DESCRIPTION OF THE PRACTICAL APPLICATIONS

In a practical implementation of SLE systems, it is important to consider the actuator specifications, especially the force amplitude and slew rate. Linear and rotatory actuators are implemented in SLE systems as the actuator's force supplied the control input in the feedback plant (GRIJALVA et al., 2020). The absolute force value provided by the actuator is the force amplitude. The slew rate is the force variation in a time period. Also, it is possible to find requirements on the position of the SLE mechanism, which is the the system's output. These requirements can be defined for safety or to avoid singularities or collisions in the structure. MPC is a technique that can be exclusively developed in discrete-time (ROSSITER, J., 2003) being necessary to define a Sampling time (Ts) which is $Ts = 0.1$ s. The choose Ts was done under the fact that the dynamics of both plants are similar, having a desired settling time of about 2 s. In this section, three applications of SLE systems based on domotics are presented, considering constraints on the plants' input and output.

5.1.1 Retractable hall lamp

The structure analyzed in this subsection, see Figure 56, is composed of four translational and three polar SLE according to the classification for SLE presented in Chapter 2. In folding condition the lamp has a width of 0.8 m and a height of 0.6 m.

In deploying condition the lamp has a width of 1.3 m and a height of 2.1 m. The input overture δ illustrated in Figure 16.b has a limit equal to δ_{BIF}, at this point, the structure exhibits a collision. Accordingly, to prevent collisions, the lamp performance must avoid overshoot. Besides, due to aesthetics purposes, it is desired that the lamp has a monotonic displacement. In summary, the constraints, in this case, are the overshoot and monotonic displacement.

Figure 56 – Retractable lamp: a) Folding condition b) Deploying condition c) Collision.

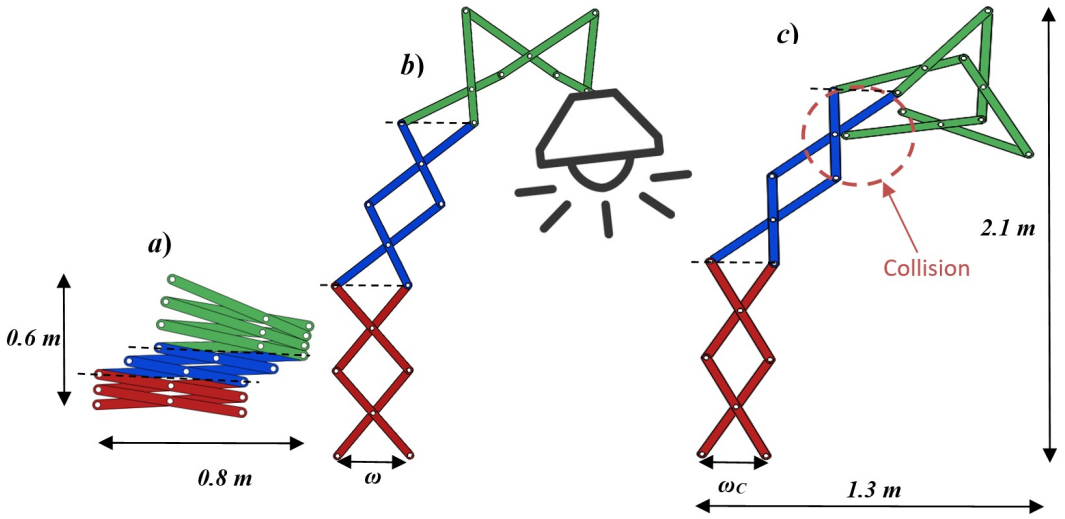

Source – From the author.

5.1.2 Folding chair

This chair was designed to be compacted in the volume of the seat (see Figure 57.a). Therefore, the chair's dimensions in folding conditions are length and width equal to 0.7 m; the height is equal to 0.15 m. The device can be deployed up to a maximum seat height equal to 0.65 m, while the back plate reaches 1.3 m (see Figure 57.c). However, because of constructive reasons, it is desired a maximum deployment equal to 0.6 m. The actuator employed in this application has a maximum force amplitude of 200 N, and the maximum slew rate is 50 N at each Ts. In summary, the system has three constraints: the maximum actuator force amplitude set at 200 N, the actuator slew rate set at 50 N, and the plant output should be constrained to 0.6 m.

5.1.3 Dynamic equation

The dynamic equation is obtained using the SLE systems approach, based on identification systems theory presented in Subsection 4.1.3. The model used in the

identification process is an ARX given by

$$y_k + a_1 y_{k-1} + a_2 y_{k-n_a} = b_0 u_{k-n_k}. \tag{56}$$

Figure 57 – Folding chair: a)Folding b) Deployed c) Maximum deploying.

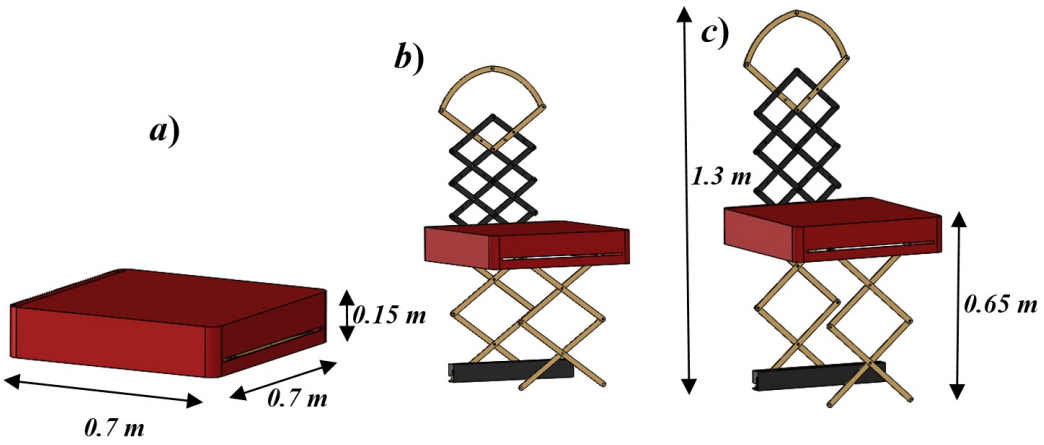

Source – From the author.

The simulations to identify the parameters of both SLE systems were developed using Simscape-Simulink. The identified values from the plants are detailed in Table 5. For

Table 5 – Identified discrete-time parameters from the chair and the lamp.

	a_1	a_2	b_0
Lamp	-1.9677	0.9625	5.3379e-05
Chair	-1.9778	0.9716	2.6230e-05

Source – From the author.

convenience, the parameters from Table 5 are expressed by polynomials in Z domain as follows

$$\begin{aligned} B_L(z^{-1}) &= b_0, A_L(z^{-1}) = 1 + a_1 z^{-1} + a_2 z^{-2}, \\ B_C(z^{-1}) &= b_0, A_C(z^{-1}) = 1 + a_1 z^{-1} + a_2 z^{-2}. \end{aligned} \tag{57}$$

In Equation (57), B_L, A_L and B_C, A_C are the polynomials in the Z domain for the lamp and chair, respectively, where the coefficients a and b have the values detailed in Table 5.

5.2 MODEL PREDICTIVE CONTROL FOR SLE SYSTEMS

In this section, to control the SLE systems, it is used one of the most popular MPC algorithms. The method is developed in detail and adapted to the dynamic

equation presented in the last section. The original algorithm is modified to include the conditions of SLE systems. This method is tested on the two plants presented above, illustrating its effectiveness and how it can be implemented.

5.2.1 Generalized predictive control

This algorithm was introduced in (CLARKE D., 1987) as a successful and popular method in the industry and academia (MARRUEDO et al., 2002). Later, (CAMACHO E., 1993) presented a constrained approach of GPC. In the subsequent years, books and articles applying these industry process and robotics approaches have been published. The concept of GPC is to compute a sequence of future control values so that it minimizes a multistage cost function under a prediction horizon. The cost function includes weighting control which is a degree of freedom to set the performance of the feedback system. These statements are illustrated in the sequel.

5.2.1.1 Formulation of the GPC for SLE

Based on the dynamic equation, in discrete-time, obtained by identification procedure, it can be defined a Controller auto-regressive with integrated moving-average (CARIMA), without delays, to apply the GPC as follows

$$A(z^{-1})y_k = B(z^{-1})u_{k-1} + C(z^{-1})\frac{e_k}{\Delta}, \tag{58}$$

where u_k and y_k are the input and output respectively of the SLE system at each sample k, e_k is a zero mean white noise characterized by a C polynomial, and $\Delta = 1 - z^{-1}$ is a discrete-time integrator. For convenience, the C polynomial is chosen to be 1. Since GPC uses predictions in the future, it is defined a prediction of the output advanced j steps ahead in the future as y_{k+j}. To compute the future outputs, it is considered the following Diophantine equation

$$1 = E_j(z^{-1})\bar{A}(z^{-1}) + z^{-j}F_j(z^{-1}). \tag{59}$$

In Equation (59) the polynomial $\bar{A} = \Delta A(z^{-1})$, E_j can be obtained by dividing 1 by $\bar{A}(z^{-1})$ being $z^{-j}F_j(z^{-1})$ the remainder of the division. The Equation (58) can be expressed in future predictions by multiplying it by $z^j E_j(z^{-1})$ as follows

$$E_j(z^{-1})\bar{A}(z^{-1})y_{k+j} = E_j(z^{-1})B(z^{-1})\Delta u_{k+j-1} + E_j(z^{-1})e_{k+j}. \tag{60}$$

As the terms of the white noise in the future have zero mean and by replacing Equation (59) in Equation (60), Equation (60) can be rewritten as

$$y_{k+j} = G_j(z^{-1})\Delta u_{k+j-1} + F_j(z^{-1})y_k, \tag{61}$$

in Equation (61) the polynomial $G_j(z^{-1}) = E_j(z^{-1})B(z^{-1})$. The GPC technique consists of applying a control sequence that minimizes a cost function of the form

$$J = \sum_{j=N_1}^{N_P} \delta\varepsilon_j^2 + \sum_{j=1}^{N_U} \lambda\Delta u_{j-1}^2, \tag{62}$$

where N_U and N_P are the control and prediction horizons respectively, the predicted error is $\varepsilon = y_{k+j} - r_{k+j}$ being r_{k+j} the desired reference, and δ and λ are the cost function's weighs. Since it was not considered delays in the plant, the value of the starting prediction horizon N_1 can be equal to 1. By using Equation (61), and for simplicity equation (62) can be rewritten in the following matrix form (NORMEY-RICO J., 2007)

$$J = (\mathbf{G\Delta u + F - r})^T \delta(\mathbf{G\Delta u + F - r}) + \mathbf{\Delta u}^T \lambda \mathbf{\Delta u}, \tag{63}$$

the controller can be calculated by minimizing the cost function J in Equation (63) over $\mathbf{\Delta u}$. The function J can be rewritten associating the common terms of Δu as follows

$$\begin{aligned}
J = & \quad (G\Delta u + F - r)^T \delta(G\Delta u + F - r) + \Delta u^T \lambda \Delta u, \\
= & \quad \left(\Delta u^T G^T + F^T - r^T\right) \delta \left(G\Delta u + F - r\right) + \Delta u^T \lambda \Delta u, \\
= & \quad \Delta u^T G^T \delta G \Delta u + \Delta u^T G^T \delta F - \Delta u^T G^T \delta r + F^T \delta G \Delta u + F^T \delta F \\
& \quad -F^T \delta r - r^T \delta G \Delta u - r^T \delta F + r^T \delta r + \Delta u^T \lambda \Delta u, \\
= & \quad \Delta u^T \left(G^T \delta G + \lambda\right) \Delta u + 2 \left(F^T - r^T\right) \delta G \Delta u + (F^T + r^T)(\delta r - \delta F).
\end{aligned} \tag{64}$$

Figure 58 – GPC scheme for SLE systems.

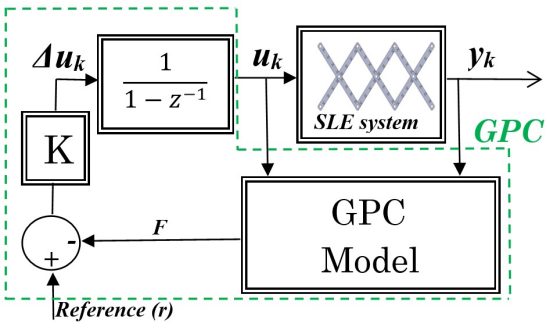

Source – From the author.

The expression in Equation (64) can be minimized in the following way

$$\begin{aligned}
\min_{\Delta u} J = & \quad \frac{\partial J}{\partial \Delta u}, \\
= & \quad 2 \left(G^T \delta G + \lambda\right) \Delta u + 2 \left(F^T - r^T\right) \delta G.
\end{aligned} \tag{65}$$

From Equation (65), the control law can be extracted as follows

$$\Delta u = \underbrace{\left(G^T \delta G + \lambda\right)^{-1} G^T \delta}_{K}(r - F). \tag{66}$$

Based on Equation (66), the discrete-time controller can be represented by the scheme depicted in Figure 58. In the next subsection, the strategy introduced above is going to be applied in the two SLE systems previously defined in Section 5.1.

5.2.2 Practical application of GPC on SLE based systems

This Subsection focuses on the plants' performance without considering the constraints on the feedback system. Both applications are tested using the GPC and a discretized approach of the Robust control method presented in Chapter 4.

5.2.3 Lamp control

The performances of the lamp obtained by applying the two approaches, GPC and Lyapunov (see Figure 59), are almost similar. On the other hand, both approaches exhibit overshoot, it can be seen in the zoom box in Figure 59.

Figure 59 – Lamp: Performance and control comparison.

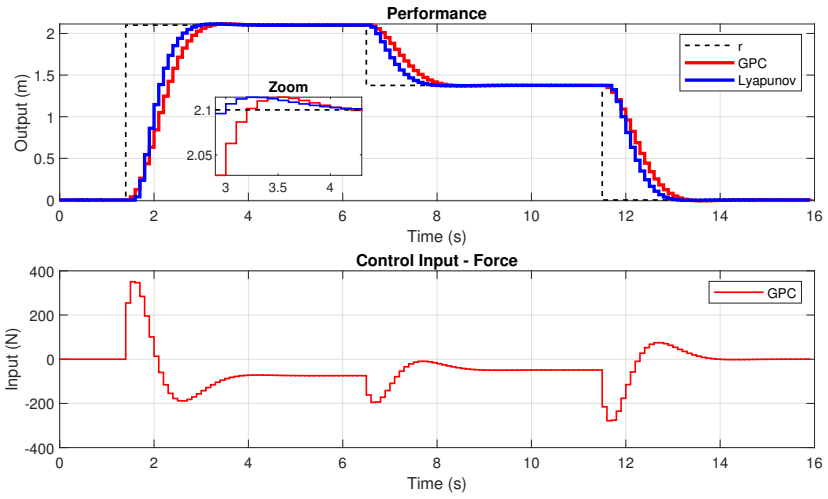

Source – From the author.

At the same time, it is evident that there is not a monotonic behavior. To achieve the performance offered by the GPC approach, an actuator with a maximum force of about 400 N is required. In this case, the overshoot causes a collision that could damage or shorten the life of the device. The Lyapunov stability-based controller was tuned allocating the poles in a circle with center in –8 and a radius of 4 on the *S*-plane; then,

this controller is discretized using the Tustin method, more details about this approach can be found in the Chapter 4. The tuning parameters of the GPC can be found in Table 6.

5.2.4 Chair control

There is a little difference between the performance in both GPC and Lyapunov cases (as seen in Figure 60). The GPC control input oversteps the actuator constraint of 200 N. The same occurs with the maximum slew rate, in Figure 60 it is possible to see a demand of a slew rate about 200 N between the eleventh and twelfth second.

Figure 60 – Chair: Performance and control comparison.

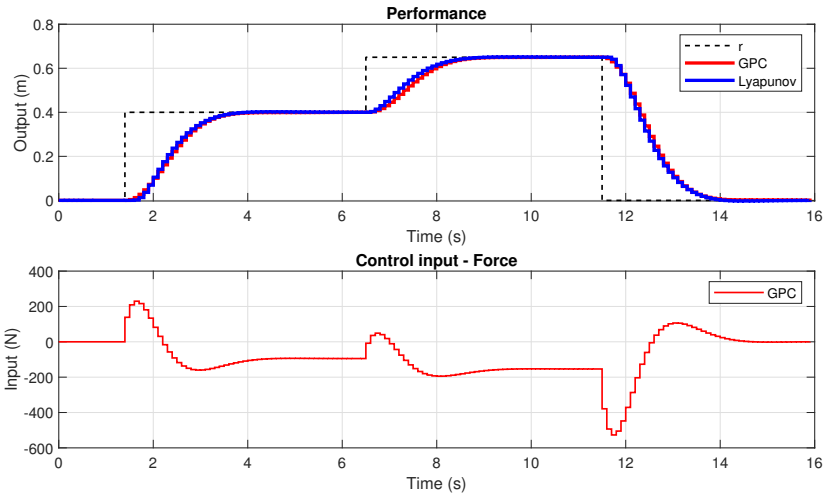

Source – From the author.

The restriction on the output set to a maximum of 0.6 m is also not achieved. For the Lyapunov based approach the tuning was done by allocating the poles of the system in a circle with center in –6 and a radius of 4 on the *S*-plane; then, this controller is discretized using the Tustin method. More details about this approach can be found in the Chapter 4. The GPC was tuned by applying the values of the parameters detailed in Table 6. A more detailed information about the tuning of GPC can be found in (CLARKE, 1994; CAMACHO, 2013).

Table 6 – Tuning parameters of GPC.

	N_U	N_P	δ	λ
Lamp	8	40	1	5e-06
Chair	8	40	1	1e-05

Source – From the author.

5.3 OPTIMAL SOLUTIONS TO DEAL WITH CONSTRAINTS ON CONTROL AND PERFORMANCE OF SLE SYSTEMS

Without considering constraints or restrictions on the feedback system could lead to a poor performance or instability. The last section showed the plants' performance introduced in Section 5.1 using GPC algorithm; however, the constraints specified in Section 5.1 were not achieved. Thus, this section presents an optimal approach to deal with the constraints in the input and output of SLE system. The results of this section are compared with the results obtained in the last section being possible to conclude about the advantages and disadvantages of this approach. For convenience, the Equation (64) is rewritten in the following quadratic form

$$J = \frac{1}{2}\Delta u^T \xi \Delta u + \beta \Delta u + \tau, \tag{67}$$

with

$$\xi = 2\left(G^T \delta G + \lambda\right), \quad \beta = 2\left(F^T - r^T\right)\delta G, \quad \textit{and} \quad \tau = (F^T + r^T)(\delta r - \delta F).$$

If it is imposed the condition in Equation (68) (CAMACHO E., 2013), where H and b are matrices with corresponding dimensions, to find the optimal solution to minimize J from Equation (67), then it is possible to adapt the SLE systems constraints. This procedure is detailed in the remaining of this section. The constraints in the feedback system can be written in the form (CAMACHO E., 2013):

$$H\Delta u \leq b, \tag{68}$$

where H and b are matrices with corresponding dimensions. The procedure to find the optimal solution to minimize J from Equation (67) considering the SLE systems constraints is detailed in the next section.

5.3.1 Actuator limited slew rate force

The folding chair has two constraints on the actuator; one of them is the limited slew rate force which is represented in the system as Δu. The requirement in the chair actuator was $\left|\Delta u\right| \leq 50$ N. To formulate this requirement in the constraint condition in Equation (68,) the inequality below can be used

$$\Delta u_{Min} \leq \Delta u \leq \Delta u_{Max}, \tag{69}$$

the Equation (69) can be rewritten in a matrix form as

$$\underbrace{\begin{bmatrix} 1 & 0 & \cdots & 0 \\ 0 & 1 & \cdots & 0 \\ \vdots & \vdots & \ddots & \vdots \\ 0 & 0 & \cdots & 1 \end{bmatrix}}_{I_{N_U \times N_U}} \underbrace{\begin{bmatrix} \Delta u_k \\ \Delta u_{k+1} \\ \vdots \\ \Delta u_{k+N_U-1} \end{bmatrix}}_{\Delta u} \geq \underbrace{\begin{bmatrix} \Delta u_{Min} \\ \Delta u_{Min} \\ \vdots \\ \Delta u_{Min} \end{bmatrix}}_{1_{N_U \times 1}\Delta u_{Min}} \tag{70}$$

$$\underbrace{\begin{bmatrix} 1 & 0 & \cdots & 0 \\ 0 & 1 & \cdots & 0 \\ \vdots & \vdots & \ddots & \vdots \\ 0 & 0 & \cdots & 1 \end{bmatrix}}_{I_{N_U \times N_U}} \underbrace{\begin{bmatrix} \Delta u_k \\ \Delta u_{k+1} \\ \vdots \\ \Delta u_{k+N_U-1} \end{bmatrix}}_{\Delta u} \leq \underbrace{\begin{bmatrix} \Delta u_{Max} \\ \Delta u_{Max} \\ \vdots \\ \Delta u_{Max} \end{bmatrix}}_{1_{N_U \times 1} \Delta u_{Max}}, \tag{71}$$

in order to adapt the conditions (70) and (71) in the form of (68), it is changed the sign of Equation (70) by multiplying it by –1 and then it is associated both conditions in one matrix as follows

$$\underbrace{\begin{bmatrix} I_{N_U \times N_U} \\ \cdots \\ -I_{N_U \times N_U} \end{bmatrix}}_{H_{\Delta u}} \Delta u \leq \underbrace{\begin{bmatrix} 1_{N_U \times 1} \Delta u_{Max} \\ \cdots \\ -1_{N_U \times 1} \Delta u_{Min} \end{bmatrix}}_{b_{\Delta u}}. \tag{72}$$

The subscript in $H_{\Delta u}$ and $b_{\Delta u}$ represents the constraint in the slew rate force. The constraint in Equation (72) is applied on the the chair system being possible to see in Figure 61 that the slew limit of 50 N is not surpassed. Also, the Constrained generalized predictive control (GPCC) performance is more unsatisfactory than the GPC approach. As more limited is the slew rate in the actuator as the plant can obtain more unsatisfactory performance.

Figure 61 – Chair: Limit on the slew rate of force.

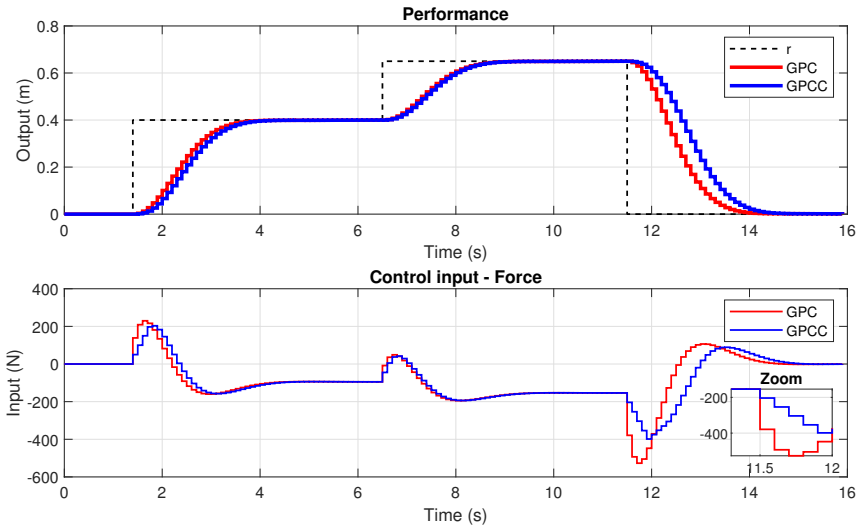

Source – From the author.

5.3.2 Constraint on the actuator force amplitude

Other restriction to be taken into account is the actuator force amplitude. The following inequality can represented this constraint

$$u_{Min} \leq u \leq u_{Max}, \tag{73}$$

for convenience, $\Delta u = u_k - u_{k-1}$ is used to rewrite Equation (73) as

$$\underbrace{\begin{bmatrix} u_{Min} \\ u_{Min} \\ \vdots \\ u_{Min} \end{bmatrix}}_{1_{N_U \times 1} u_{Min}} \leq \underbrace{\begin{bmatrix} 1 & 0 & \cdots & 0 \\ 1 & 1 & \cdots & 0 \\ \vdots & \vdots & \ddots & \vdots \\ 1 & 1 & \cdots & 1 \end{bmatrix}}_{T_{N_U \times N_U}} \underbrace{\begin{bmatrix} \Delta u_k \\ \Delta u_{k+1} \\ \vdots \\ \Delta u_{k+N_U-1} \end{bmatrix}}_{\Delta u} + \underbrace{\begin{bmatrix} u_{k-1} \\ u_{k-1} \\ \vdots \\ u_{k-1} \end{bmatrix}}_{1_{N_U \times 1} u_{k-1}} \leq \underbrace{\begin{bmatrix} u_{Max} \\ u_{Max} \\ \vdots \\ u_{Max} \end{bmatrix}}_{1_{N_U \times 1} u_{Max}}, \tag{74}$$

by developing a procedure similar to the last subsection, it can be adapted the inequality above to have the form of the condition in Equation (68) as follows

$$\underbrace{\begin{bmatrix} T_{N_U \times N_U} \\ \cdots \\ -T_{N_U \times N_U} \end{bmatrix}}_{H_u} \Delta u \leq \underbrace{\begin{bmatrix} 1_{N_U \times 1} u_{Max} \\ \cdots \\ -1_{N_U \times 1} u_{Min} \end{bmatrix}}_{b_u}. \tag{75}$$

Figure 62 – Chair: Constraint on the actuator force amplitude.

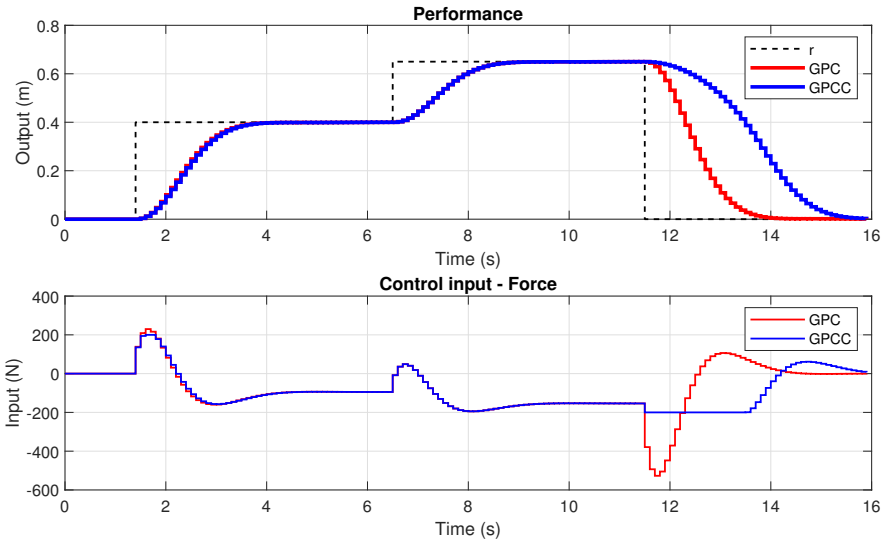

Source – From the author.

The subscript in H_u and b_u represents the constraint in the system's input. In Figure

62, by applying the condition in Equation (75), it is possible to see that the control input of the GPCC approach does not surpass the maximum actuator force amplitude, in this case $|u| \leq 200$ N. Moreover, it can be seen the more unsatisfactory performance presented by the GPCC approach due to the limited actuator force amplitude, especially in the last part, when the system demanded the maximum actuator force.

5.3.3 Restriction on the system output

Because of safety, space availability, among other reasons, it is possible to restrict the SLE system output. In the case of the chair, it was defined a displacement restriction of 0.6 m on the system output. The following inequality can represented this restriction

$$y \leq y_{Max}. \tag{76}$$

Replacing Equation (61) in Equation (76), namely

$$G\Delta u + F \leq y_{Max}, \tag{77}$$

the Equation (77) can be rewritten in the form of (68), see below

$$\underbrace{\left[G_{N_P \times N_U}\right]}_{H_y} \Delta u \leq \underbrace{\left[1_{N_P \times 1} y_{Max} - F_{N_P \times 1}\right]}_{b_y}. \tag{78}$$

Figure 63 – Chair: Restriction on the system output.

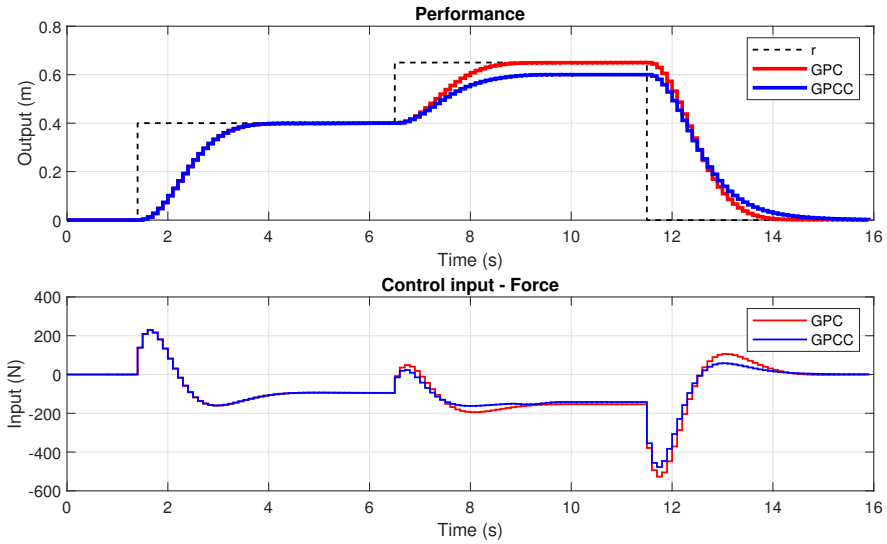

Source – From the author.

The subscript in H_y and b_y represents the constraint in the plant's output. The GPCC,

considering the restriction on the output, is plotted in Figure 63. Even though the reference is set at 0.65 m, the GPCC does not exceed the 0.6 m restriction on the output. In this case, the performance and the control input in this case are almost similar in both GPC and GPCC approaches.

5.3.4 Overshoot avoidance

In Figure 56.c, it was possible to see how the overshoot can cause an undesired collision. The overshoot can reduce mobility, increase jams, poor quality (in manufactured products), singularities, among other drawbacks. The condition to avoid overshoot can be defined as

$$\begin{aligned} y \leq r, \quad if \quad r > y, \\ y \geq r, \quad if \quad r < y, \end{aligned} \tag{79}$$

where r is the reference and y is the output of the plant. Replacing Equation (61) in Equation (79), namely

$$G\Delta u + F \leq r \quad \wedge \quad G\Delta u + F \geq r. \tag{80}$$

Figure 64 – Lamp: Constraint on overshoot.

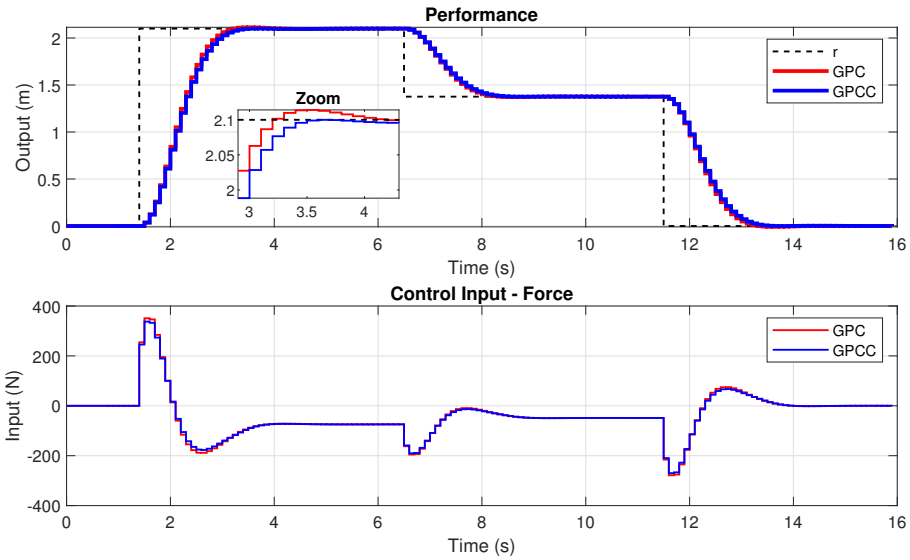

Source – From the author.

The inequalities in (79) can be rewritten in the form of (68) as follows

$$\underbrace{\begin{bmatrix} G_{N_P \times N_U} \\ \cdots \\ -G_{N_P \times N_U} \end{bmatrix}}_{H_O} \Delta u \leq \underbrace{\begin{bmatrix} 1_{N_P \times 1} r - F_{N_P \times 1} \\ \cdots \\ -1_{N_P \times 1} r + F_{N_P \times 1} \end{bmatrix}}_{b_O}. \tag{81}$$

The subscript in H_O and b_O represents the constraint on the overshoot. In Figure 64, the control input of both GPC and GPCC approaches are similar; however in the performance's zoom, it is possible to see that the GPCC approach does not exhibit overshoot, warranting the collision avoidance by the lamp structure.

5.3.5 Monotonic behavior

The last requirement set to the lamp system was to have a monotonic performance. In terms of the output, it can be defined the monotonic motion by the following conditions

$$\begin{aligned} y_{k+j} &\leq y_{k+j+1}, if \quad y < r, \\ y_{k+j} &\geq y_{k+j+1}, if \quad y > r. \end{aligned} \tag{82}$$

If it is used Equation (61) in Equation (82), namely

$$G_{k+j}\Delta u + F_{k+j} \leq G_{k+j+1}\Delta u + F_{k+j+1} \quad \wedge \quad G_{k+j}\Delta u + F_{k+j} \geq G_{k+j+1}\Delta u + F_{k+j+1}, \tag{83}$$

associating the terms of Δu, Equation (83) can be rewritten as

$$\begin{aligned} &\underbrace{\begin{bmatrix} G_0 & 0 & \cdots & 0 \\ G_0 - G_1 & G_0 & \cdots & 0 \\ \vdots & \vdots & \ddots & \vdots \\ G_{N_P-2} - G_{N_P-1} & G_{N_P-3} - G_{N_P-2} & \cdots & G_0 \end{bmatrix}}_{\widetilde{G}} \Delta u \leq \underbrace{\begin{bmatrix} F_1 - F_0 \\ F_2 - F_1 \\ \vdots \\ F_{N_P-1} - F_{N_P} \end{bmatrix}}_{\widetilde{F}} \quad \wedge \\ &\underbrace{\begin{bmatrix} G_0 & 0 & \cdots & 0 \\ G_0 - G_1 & G_0 & \cdots & 0 \\ \vdots & \vdots & \ddots & \vdots \\ G_{N_P-2} - G_{N_P-1} & G_{N_P-3} - G_{N_P-2} & \cdots & G_0 \end{bmatrix}}_{\widetilde{G}} \Delta u \geq \underbrace{\begin{bmatrix} F_1 - F_0 \\ F_2 - F_1 \\ \vdots \\ F_{N_P-1} - F_{N_P} \end{bmatrix}}_{\widetilde{F}}. \end{aligned} \tag{84}$$

The inequalities in (84) can be rewritten in the form of (68) as follows

$$\underbrace{\begin{bmatrix} \widetilde{G}_{N_P \times N_U} \\ \cdots \\ -\widetilde{G}_{N_P \times N_U} \end{bmatrix}}_{H_M} \Delta u \leq \underbrace{\begin{bmatrix} \widetilde{F}_{N_P \times 1} \\ \cdots \\ -\widetilde{F}_{N_P \times 1} \end{bmatrix}}_{b_M}. \tag{85}$$

The subscript in H_M and b_M represents the constraint on the monotonic performance. Note that the performance in Figure 65 exhibits overshoot. However, the ascending and descending monotonic behavior is achieved. In addition to aesthetics, the monotonic performance avoid abrupt shakes to the user; thus, improving the chair's ergonomic. There are not significant differences in the control input.

Figure 65 – Lamp: Monotonic performance.

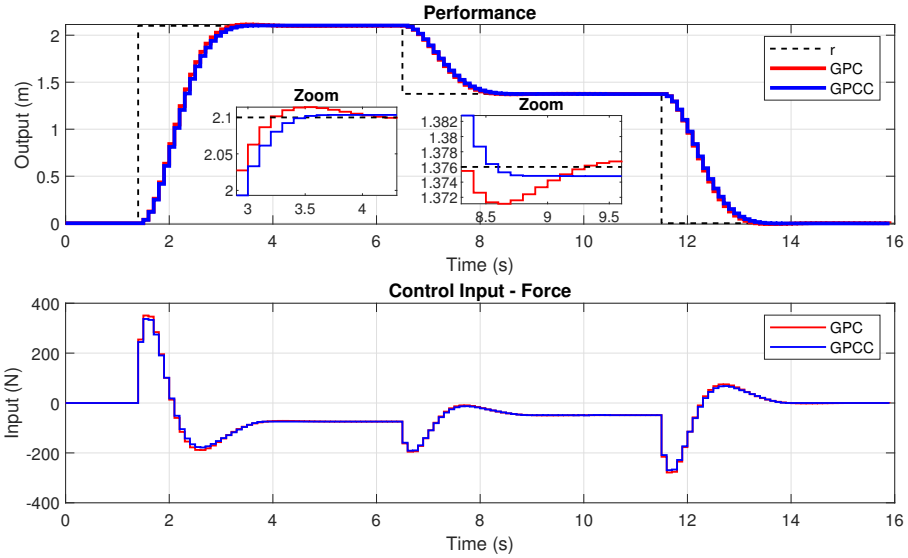

Source – From the author.

5.3.6 Combination of constraints

The requirements for the chair and the lamp systems were achieved one by one in the last subsections. Nevertheless, in Section 5.1, it was specified that the plants should fulfill a group of conditions simultaneously.

Figure 66 – Lamp: Restriction on the overshoot and monotonic performance.

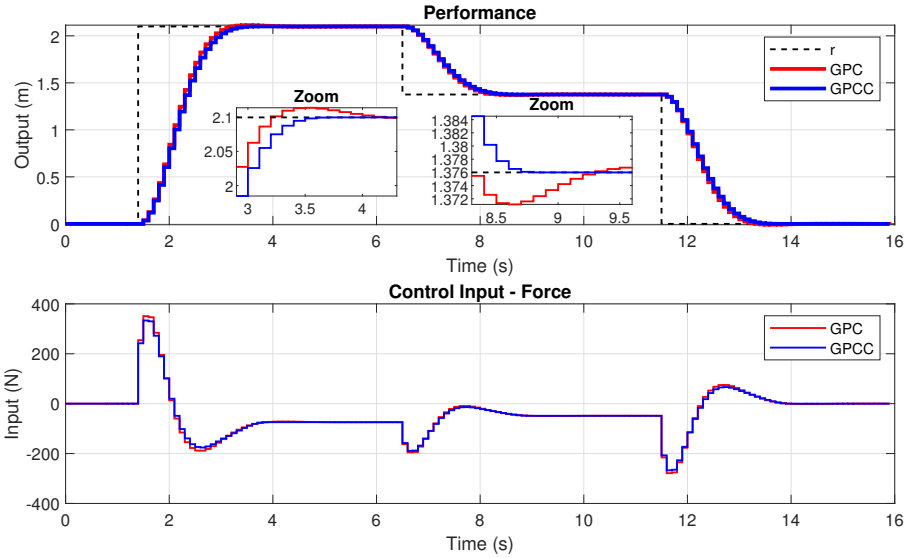

Source – From the author.

It is possible to associate two or more conditions in one matrix. For example, in the case of the chair, three restrictions were defined: maximum actuator slew rate, maximum actuator force amplitude, and displacement constraint on the output. These requirements can be associated as follows

$$\begin{bmatrix} H_{\Delta u} \\ \cdots \\ H_u \\ \cdots \\ H_y \end{bmatrix} \leq \begin{bmatrix} b_{\Delta u} \\ \cdots \\ b_u \\ \cdots \\ b_y \end{bmatrix}. \tag{86}$$

The comparison, considering the three constraints, between the GPC and the GPCC is plotted in Figure 67. The GPCC input does not surpass the maximum values of the actuator amplitude or the actuator slew rate. Because of the actuator limitations, the GPCC performance is more unsatisfactory than the GPC performance. Also, the GPCC performance respects the restriction on the system output.

Figure 67 – Chair: Constrains on slew rate, amplitude of actuators and output.

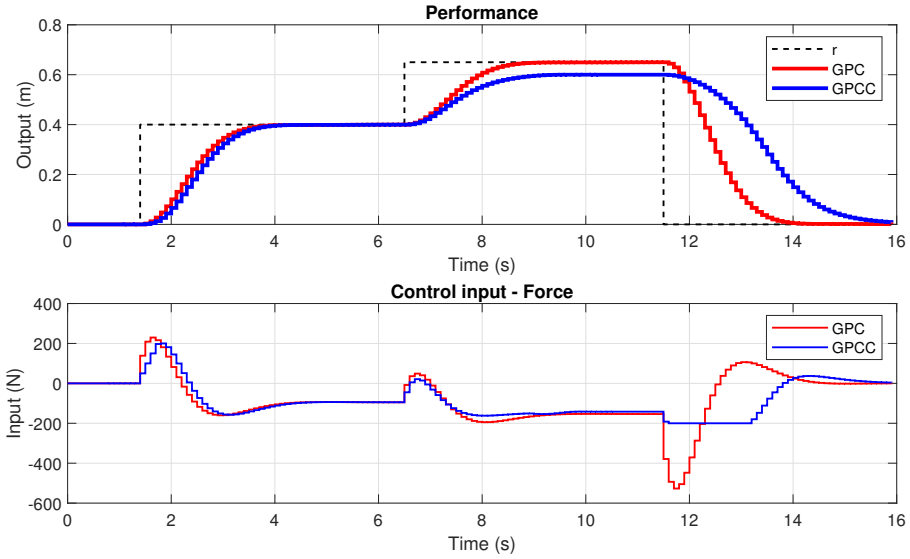

Source – From the author.

In the same way, the conditions imposed to the lamp system can be combined, see below

$$\begin{bmatrix} H_O \\ \cdots \\ H_M \end{bmatrix} \leq \begin{bmatrix} b_O \\ \cdots \\ b_M \end{bmatrix}. \tag{87}$$

In Figure (66), the control input of both approaches is similar; nonetheless, the GPCC performance does not exhibit overshoot, also it satisfies the requirement of monotonic

behavior.

5.3.7 Application in machining process

A typical challenge is long-range machining in manufacturing large products, such as cars, airplanes, and ships (GONZALEZ D., 2017). Traditional industrial robots cannot fit on the large products conveyor line (ATKINSON et al., 2007) as they have to access manufacturing sites within large parts. Another requirement in the manufacturing of these products is industrial safety and high-quality standards (ATKINSON et al., 2007). Overshoot in the tool path can cause inaccurate machining on products (CHEN et al., 2017) leading to low-quality manufacturing. By constraining the path of the tool, accidents can be avoided; thus, improving industrial safety. The drilling system presented in this subsection offers the possibility of reaching a long machining range, in addition to constraining the tool path. In this system, a displacement mechanism based on SLE is used to cover a greater range than conventional drilling machines. The constraints on the tool path are regulated using the MPC approach shown above. This controller accomplishes the task of stabilizing, restricts overshoot, and limits the advance of the tool. The simulation process was developed under ideal conditions; means that the dynamics of the machining process is minimal.

5.3.7.1 Parts of the drilling system

The drilling system, based on Figure 68, is made up of the next parts:

Figure 68 – Drilling system composed by four SLE: a) folding state b) deploying state.

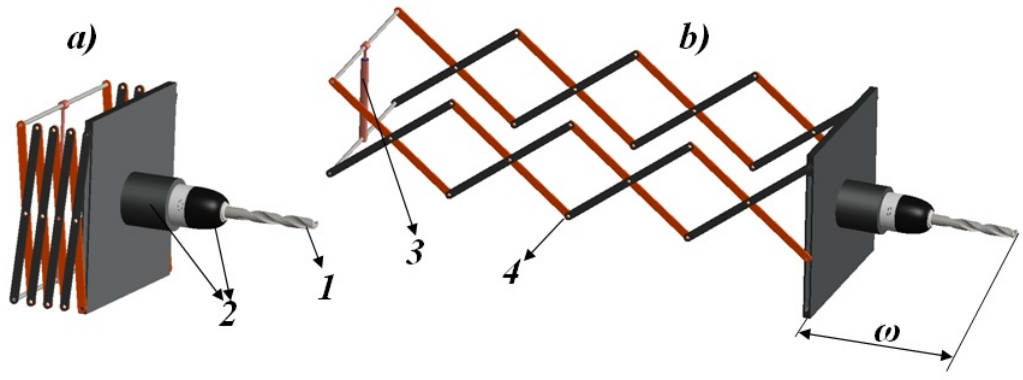

Source – From the author.

1. *Tool:* In this case, a drill bit, which is a cutting tool used to remove material to create holes, almost always of circular cross-section.

2. *Chuck and torque generator:* The chuck is in charge of securing the drill bit. The torque generator, which can be a motor impulsed by pneumatic or electrical energy, is responsible for transmitting the power to the tool.

3. *Prismatic actuator:* This actuator regulates the deployment of the SLE structure during the advance of the tool by the chuck.

4. *SLE assembly:* This deployable structure gives the characteristic of reaching a long-range to the tool. Its geometric design is discussed in the next subsection.

The values identified from the drilling system, for the ARX model in Equation (56), are $a_1 = -1,95$, $a_2 = 0.93$, and $b_0 = 0.0015$.

5.3.7.2 Constraints on the tool path

In the drilling system depicted in Figure 68, the next restrictions are taken into account:

a) Restriction on the advance of the tool

Because of industrial safety, the availability of space, among other reasons, it is possible to have the need to restrict the tool's path. In the case of the drilling system, a constraint of $y_{Max} = 1$ m was defined in the system's output.

Figure 69 – Constraint on the tool path of the drilling system.

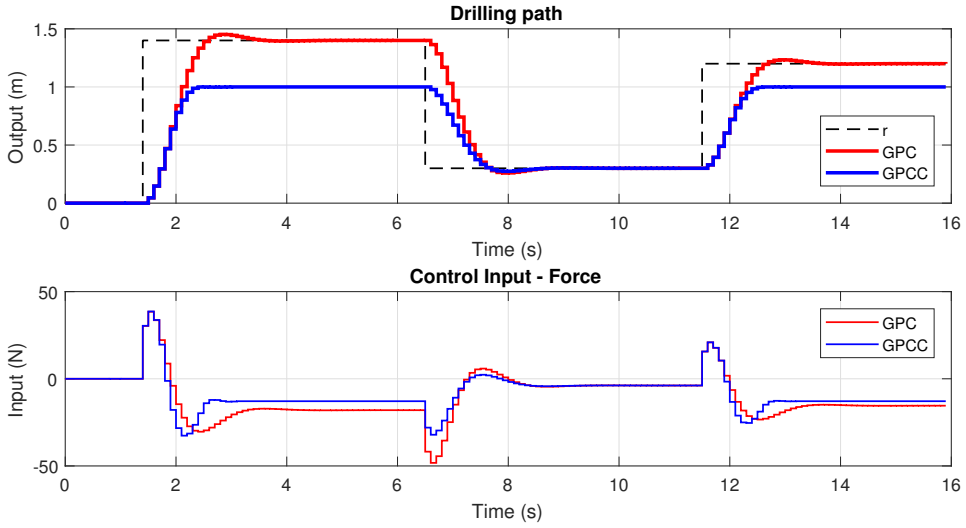

Source – From the author.

In Figure 69, it can be seen a simulation of a drilling process where the tool has to

reach a distance of 1.4 m to make a hole. Then the tool moves back to a reference of 0.3 m, and finally, the tool has to reach a distance of 1.2 m to make a second hole. In the red line on Figure 69, the plant's performance by using the GPC is shown. In the blue line, the performance of the GPCC, in which it is applied the condition in Equation (78), is depicted. Also, it is possible to see that even though the output reference is grater than y_{Max}, the tool path does not exceed the constraint of y_{Max} = 1 m. The force supplied by the prismatic actuator to the mechanism can be seen in Figure 69, too, being possible to conclude that an actuator with a maximum force equal or grater than 50 N is necessary. The controller was tuned as follows: N_P = 40, N_U = 8, λ = 0.001, and δ = 1.

b) Constraint on the overshoot

The overshoot of the tool path can cause poor quality in manufacturing many products. The condition to avoid overshoot was defined in Equation (81).

Figure 70 – Constraint on the overshoot of the drilling path.

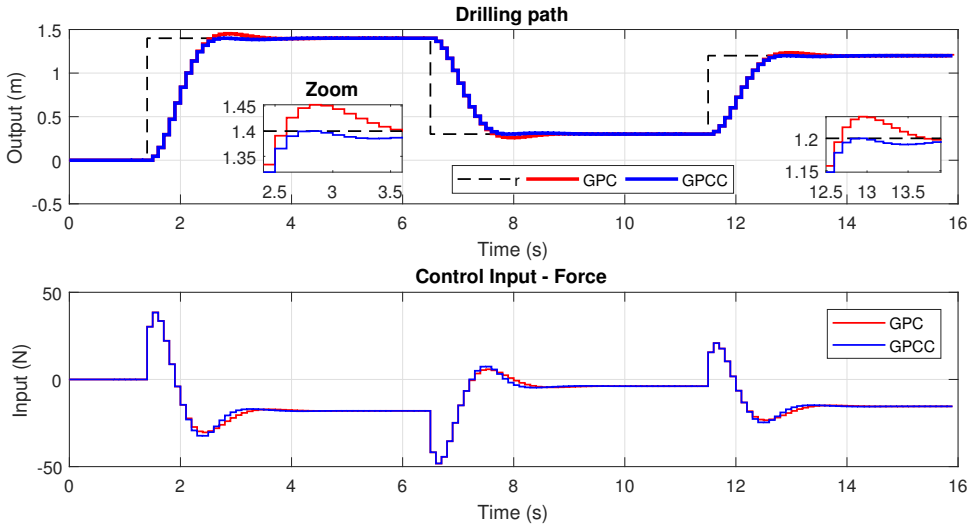

Source – From the author.

In Figure 70, it can be seen a comparison of GPC and GPCC of the drilling path performance. In the blue line, the effectiveness of the GPCC using the condition in Equation (81) is depicted. The overshoot of about 5 cm can cause poor quality in the manufacture or, even worse, and a collision can produce a break in the tool . The force supplied by the actuator is almost similar in both cases being necessary an actuator able to supply at least 50 N.

5.4 CHAPTER CONCLUSION

By improving the tuning parameters on GPC, the SLE system's performance obtained could be better. At the same time, the demand for an actuator with better performance, in terms of force amplitude and slew rate, would be higher. In practical implementations, it is necessary to know and consider the actuator's specifications from SLE systems. Thus, previously to the implementation, the controller designed and simulated can be considered trustworthy. In all the situations the GPCC does not violate the restrictions; on the other hand, it was possible to see that the constraints and limitations caused a more unsatisfactory performance than the GPC. This approach offers the possibility of defining the constraints one by one or in group by combining them. In all cases of the feedback systems introduced in this chapter, it was found a feasible solution; nevertheless, if the requirements defined to the system are physically impossible to be achieved, then the solver will show an alert message of unfeasible solution. Physical and safety restrictions can be implemented rapidly in the controller system. The restrictions in the controller does not increment, in general, the computational complexity of the problem to be solved. The combination of constraints in the system can lead to unfeasible problems in the controller, not due to the method, but due to physical aspects in the plant.

6 CONCLUSION

One of the main principles of mechatronics is the design of the product as a whole, that is, avoiding design in stages; for example, separating mechanical, electronic, and the computational design. The mechatronic expert when designing the mechanical structure also thinks about the electronic part and programming to achieve this target, resulting in an optimized mechatronic device. From this perspective, Folding Mechatronics is presented in this thesis as a new technology that aims to design mechatronic products that can compact and deploy as necessary. All the applications presented in this work were designed from a mechatronic perspective; however, it is important to highlight that in order to aid reader comprehension, this thesis was divided into separate sections devoted to mechanics and automation.

SLE structures generally have one degree of freedom being necessary to use only one actuator to control the entire structure regardless of the number of SLE that the assembly may have. Using only one actuator, in the control of devices made up of SLE, helps to improve energy efficiency and simplify the design of control algorithms.

The use of DQ in the kinematic analysis of planar and spherical SLE proved to be an efficient tool from a computational perspective as well as being versatile. The possibility of representing mechanical connectors through DQ helps to analyze three-dimensional structures. Also through the examples of the lamp and the television furniture it was proved that the DQs can be used to orient vectors, lines and planes. Algorithm 2 was used to analyze the SLE structures workspace, making it possible to design SLE based devices more efficiently. Through Algorithm 1 it was possible to detect singularities in the SLE structures, these singularities were considered when designing the control algorithms in order to avoid unsatisfactory performance or instability. The spherical SLE were classified in a similar way to the planar SLE. A kinematic analysis was also performed using DQ. Through practical applications such as the spherical retractable roof (Figure 31) and the spherical lamp (Figure 32) it was shown that one of the main advantages of this type of SLE is that three-dimensional structures can be formed with a lower amount of SLE. Besides, it is not possible to conclude on the advantages and disadvantages between the planar and the spherical SLE, these will depend strictly on the application.

Inspired by folding hand fan SLO, which combines SLE with origami, proved to be a good tool when designing lightweight folding structures of large size. The kinematic analysis of SLO could be performed using the theory based on DQ developed in Chapter 2.

The strategy shown in Chapter 4 to obtain states equation, both in continuous time and in discrete time, representing the dynamics of SLE-based systems proved to be fast, efficient, and versatile. The robust control strategy presented in Chapter 4 was

tested in many SLE based system, ensuring stabilization and zero steady-state error. The robustness of this approach reduced the uncertainties influence of dynamic forces such as friction in the joints. The performance of SLE based systems was defined using LMI-based conditions which limit the feedback system's poles in an arbitrary region on the S-plane being possible to regulate the rising time, overshoot, settling time and other performance parameters. The SLE structre, in the SLO robots control, was used to regulate the morphology and performance being possible to apply effectively the robust control strategy presented in Chapter 4.

In mechatronic applications it is necessary to consider the limitations in amplitude and slew rate of the force provided by the actuators. Chapter 5 shows a strategy to control systems based on SLE considering actuator's limitations and movement restrictions. The predictive strategy can consider the constraints one by one or group them at the same time. This strategy proved to be effective in avoiding singularities and collisions; for example, in the machining application depicted in Figure 67, the predictive strategy avoided the collision of the tool at the same time offered a high quality machining since the overshoot of the tool was restricted in the optimization condition of the GPC.

The design of versatile and efficient mechanisms with an embedded control system has wide application in home automation, aeronautics, architecture and in the industries' automation. Flexible manufacturing cells could be designed using the long-range drilling system presented in Chapter 5. This type of mechatronic systems contributes to Industry 4.0 that seeks the interactivity of machines and processes. Smart furniture that can be compacted and have an integrated control system could give way to multi-functional environments. For example, using the internet of things with a cell phone application, a room in an apartment or a house could be transformed from a living room into a study-room or a kitchen only by unfolding and compacting the appropriate furniture. In the same way, folding mechatronics makes possible to create flexible environments in various industries that, in addition to being versatile, will have the possibility of interconnecting and showing their performance to the user in real time. Applications of this technology and other aspects are mentioned in the suggestions for future work in the next section.

6.1 SUGGESTIONS FOR FUTURE WORK

Suggestions for future work include:

- Research about the differential kinematics, based on DQ, being possible to define conditions and theorems to deal with the kinematic control of SLE.
- Use another folding mechanism instead of SLE. For example, continuous tension elements with discontinuous compression elements such as cables and struts,

this method is known as tensegrity.

- Use other crease patterns in the design of SLO robots.
- Design and fabricate SLO applications mainly focused on mobile robots, energy storage, gripping and architecture.
- Explore LMI conditions to deal with constraints in states, input, and output of SLE based systems.
- Research about solutions related to the influence of delays and disturbances in SLE systems.
- Develop industrial and domotics applications based on Folding Mechatronics considering aspects of Industry 4.0.

6.2 PUBLICATION LIST

The following papers were published in relation to the work presented in this thesis.

- GRIJALVA, Juan G.; DE PIERI, Edson R.; MARTINS, Daniel. Dual-quaternion on simple scissor-like elements. In IFToMM World Congress on Mechanism and Machine Science. Springer, Cham, 2019. p. 449-458.
- GRIJALVA, Juan Gabriel Guerrero; DE PIERI, Edson Roberto. Kinematic analysis of scissor-like elements using dual quaternions, 2020, PREPRINT available at Research Square [https://doi.org/10.21203/rs.3.rs-45973/v1]
- GRIJALVA, Juan G.; DE PIERI, Edson R.; MARTINS, Daniel. Robust control of scissor-like elements based systems. Mechanism and Machine Theory, 2020, vol. 150, p. 103849.
- GRIJALVA, Juan Gabriel Guerrero; DE PIERI, Edson Roberto; MARTINS, Daniel. Synthesis of a Retractable Roof System Based on Spherical Scissor-Like Elements. In International Symposium on Multibody Systems and Mechatronics. Springer, Cham, 2021. p. 246-253.
- G GRIJALVA, Juan; PIERI, Edson R. De; MARTINS, Daniel. Long-Range Drilling System with Constrained Tool Path Based on Scissor-Like Elements. In Advances in Industrial Machines and Mechanisms. Springer, Singapore, 2021. p. 185-193.

REFERENCES

AKGUN, Yenal. **A novel transformation model for deployable scissor-hinge structures**. Thesis (PhD)— University of Stuttgart, Faculty of Architecture and Urban Planning, 2010.

ALY, Ayman A. Car suspension control systems: basic principles. **International journal of control, automation and systems**, 2012, vol. 1, no 1, p. 41-46.

ATKINSON, Joe, et al. **Robotic drilling system for 737 aileron**. SAE Technical Paper, 2007.

BENCIOLINI, Battista; VITTI, Alfonso. A new quaternion based kinematic model for the operation and the identification of an articulated arm coordinate measuring machine inspired by the geodetic methodology. **Mechanism and Machine Theory**, 2017, vol. 112, p. 192-204.

BHOVAD, Priyanka; KAUFMANN, Joshua; LI, Suyi. Peristaltic locomotion without digital controllers: Exploiting multi-stability in origami to coordinate robotic motion. **Extreme Mechanics Letters**, 2019, vol. 32, p. 100552.

CAMACHO, EF. Constrained generalized predictive control. IEEE Transactions on Automatic Control, 1993, vol. 38, no 2, p. 327-332.

CAMACHO, Eduardo F.; ALBA, Carlos Bordons. Model predictive control. Springer science and business media, 2013.

CASEMENT, Suzanne, et al. Starshade design driven by stray light from edge scatter. In Space Telescopes and Instrumentation 2012: Optical, Infrared, and Millimeter Wave. **International Society for Optics and Photonics**, 2012. p. 84424H.

CHEN, Shou-yan; ZHANG, Tie; ZOU, Yan-biao. Fuzzy-sliding mode force control research on robotic machining. Journal of Robotics, 2017, vol. 2017, p. 1-9.

CHEN, Yan, et al. Mobile assemblies of four-spherical-4R-integrated linkages and the associated four-crease-integrated rigid origami patterns. **Mechanism and Machine Theory**, 2019, vol. 142, p. 103613.

CHEN, Yao; YAN, Jiayi; FENG, Jian. Geometric and kinematic analyses and novel characteristics of origami-inspired structures. Symmetry, 2019, vol. 11, no 9, p. 1101-1115.

CHEVALLIER, D. P. Lie algebras, modules, dual quaternions and algebraic methods in kinematics. **Mechanism and Machine Theory**, 1991, vol. 26, no 6, p. 613-627.

CHEVALLIER, D. P. On the transference principle in kinematics: its various forms and limitations. **Mechanism and Machine Theory**, 1996, vol. 31, no 1, p. 57-76.

CLARKE, David W.; MOHTADI, Coorous; TUFFS, P. S. Generalized predictive control—Part I. The basic algorithm. Automatica, 1987, vol. 23, no 2, p. 137-148.

CLARKE, David (ed.). Advances in model-based predictive control. Oxford: Oxford university press, 1994.

CONCEIÇÃO, André Gustavo Scolari, et al. Design and implementation of model-predictive control with friction compensation on an omnidirectional mobile robot. IEEE/ASME Transactions On Mechatronics, 2013, vol. 19, no 2, p. 467-476.

DAI, Jian S. Euler–Rodrigues formula variations, quaternion conjugation and intrinsic connections. **Mechanism and Machine Theory**, 2015, vol. 92, p. 144-152.

DE TEMMERMAN, Niels. **Design and analysis of deployable bar structures for mobile architectural applications**. Thesis (PhD)— Vrije Universiteit Brussel, Department of Architectural Engineering Sciences, 2007.

DOS SANTOS, Carlos Henrique Farias; DE PIERI, Edson Roberto. Functional machine with Takagi–Sugeno inference to coordinated movement in underwater vehicle-manipulator systems. IEEE Transactions on Fuzzy Systems, 2013, vol. 21, no 6, p. 1105-1114.

DUAN, Guang-Ren; YU, Hai-Hua. LMIs in control systems: analysis, design and applications. CRC press, 2013.

DUFFY, Oliver B., et al. Structural evolution of salt-influenced fold-and-thrust belts: a synthesis and new insights from basins containing isolated salt diapirs. Journal of Structural Geology, 2018, vol. 114, p. 206-221.

EBIHARA, Yoshio; PEAUCELLE, Dimitri; ARZELIER, Denis. S-variable approach to LMI-based robust control. New York: Springer, 2015.

ESCRIG, Felix. Expandable space structures. International Journal of Space Structures, 1985, vol. 1, no 2, p. 79-91.

FARRUGIA, Pierre. **Kinematic analysis of foldable structures**. Thesis (PhD)—University of Surrey (United Kingdom), 2008.

FEATHERSTONE, Roy. Plucker basis vectors. In Proceedings 2006 IEEE International Conference on Robotics and Automation, 2006. ICRA 2006. IEEE, 2006. p. 1892-1897.

FENG, Jingshan Zhao Zhijing; CHU, Ning Ma Fulei. Design of special planar linkages. Springer, 2014.

FENG, Gang. Analysis and synthesis of fuzzy control systems: a model-based approach. CRC press, 2018.

GONZALEZ, Daniel J.; ASADA, H. Harry. Design and analysis of 6-dof triple scissor extender robots with applications in aircraft assembly. **IEEE Robotics and Automation Letters**, 2017, vol. 2, no 3, p. 1420-1427.

GRANT, Michael C.; BOYD, Stephen P. Graph implementations for nonsmooth convex programs. En Recent advances in learning and control. Springer, London, 2008. p. 95-110.

GRIJALVA, J. G.; KLUG, Michael; CASTELAN, E. Control of a quadrotor under sensors sampling limitations using TS fuzzy modeling: a discrete time approach. In Simposio Brasileiro de Automacao Inteligente, 2017, p. 351-357.

GRIJALVA, Juan G.; DE PIERI, Edson R.; MARTINS, Daniel. Dual-quaternion on simple scissor-like elements. In IFToMM World Congress on Mechanism and Machine Science. Springer, Cham, 2019. p. 449-458.

GRIJALVA, Juan G.; DE PIERI, Edson R.; MARTINS, Daniel. Robust control of scissor-like elements based systems. **Mechanism and Machine Theory**, 2020, vol. 150, p. 103849.

GRIJALVA, Juan Gabriel Guerrero; DE PIERI, Edson Roberto; MARTINS, Daniel.

Synthesis of a Retractable Roof System Based on Spherical Scissor-Like Elements. In International Symposium on Multibody Systems and Mechatronics. Springer, Cham, 2021. p. 246-253.

HESTENES, David. New foundations for classical mechanics. Springer Science and Business Media, 2012.

HOBERMAN, Charles. Reversibly expandable doubly-curved truss structure. U.S. Patent No 4,942,700, 24 Jul. 1990.

HOBERMAN, Charles. Radial expansion/retraction truss structures. U.S. Patent No 5,024,031, 18 Jun. 1991.

HOBERMAN, Chuck. Unfolding architecture. Architectural Design, 1993, no 102, p. 56-59.

JIANGUO, Cai, et al. Nonrigidly foldability analysis of Kresling cylindrical origami. Journal of Mechanisms and Robotics, 2017, vol. 9, no 4, p. 041018.

JUNGERS, Marc, et al. Bounded Nash type controls for uncertain linear systems. Automatica, 2008, vol. 44, no 7, p. 1874-1879.

LAI, Eleonora; MULAS, Maria G. A MSD model for coupled analysis of pedestrian-footbridge dynamic interaction. Procedia engineering, 2017, vol. 199, p. 2864-2870.

LENNART, Ljung. System identification: theory for the user. PTR Prentice Hall, Upper Saddle River, NJ, 1999, vol. 28.

LI, Xiangyun, et al. A unified algorithm for analysis and simulation of planar four-bar motions defined with R-and P-joints. Journal of Mechanisms and Robotics, 2015, vol. 7, no 1, p. 011014.

LI, Ju; MICHAEL MCCARTHY, J. Analysis of two spherical parallel manipulators with hidden revolute joints. Journal of Mechanisms and Robotics, 2017, vol. 9, no 3, p. 031007.

LI, Shuguang, et al. Fluid-driven origami-inspired artificial muscles. Proceedings of the National academy of Sciences, 2017, vol. 114, no 50, p. 13132-13137.

LI, J., et al. A soft active origami robot. **Extreme Mechanics Letters**, 2018, vol. 24, p. 30-37.

LOUNESTO, Pertti. Clifford algebras and spinors. Cambridge university press, 2001.

MAHMOUD, Chilali; PASCAL, Gahinet. H(infinite) design with pole placement constraints: an LMI approach. IEEE Transactions on Automatic Control, 1996, vol. 41, no 3, p. 358-367.

MARRUEDO, D. Limon; ALAMO, T.; CAMACHO, E. F. Input-to-state stable MPC for constrained discrete-time nonlinear systems with bounded additive uncertainties. In Proceedings of the 41st IEEE Conference on Decision and Control, 2002. IEEE, 2002. p. 4619-4624.

NELSON, Todd G., et al. Origami-inspired sacrificial joints for folding compliant mechanisms. **Mechanism and Machine Theory**, 2019, vol. 140, p. 194-210.

NORMEY-RICO, Julio E. Control of dead-time processes. Springer Science and Business Media, 2007.

PENG, Rui; MA, Jiayao; CHEN, Yan. The effect of mountain-valley folds on the rigid foldability of double corrugated pattern. **Mechanism and Machine Theory**, 2018, vol. 128, p. 461-474.

GONZÁLEZ, José Alfonso Pérez. Los abanicos de Aldaia. Narria: Estudios de artes y costumbres populares, 1994, no 65, p. 27-33.

QIAN, Gonglin. Chinese Fans: Artistry and Aesthetics. Long River Press, 2004.

RADAVELLI, Luiz, et al. A comparative study of the kinematics of robots manipulators by Denavit-Hartenberg and dual quaternion. Mecánica Computacional, 2012, vol. 31, no 15, p. 2833-2848.

RADAVELLI, L. Análise cinemática direta de robôs manipuladores via álgebra de clifford e quatérnios. 2013. Master Thesis, Mechanical Engineering Department, UFSC.

RADAVELLI, Luiz Alberto, et al. A screw dual quaternion operator for serial robot kinematics. Proceedings of PACAM XIV, Santiago, 2014, p. 27-38.

RADAVELLI, Luiz A., et al. Cinemática posicional de robôs via iteração e quatérnios. Proceeding Series of the Brazilian Society of Computational and Applied Mathematics, 2015, vol. 3, no 1, p. 0101921-0101927.

ROSSITER, J. Anthony. Model-based predictive control: a practical approach. CRC press, 2003.

RUS, Daniela; TOLLEY, Michael T. Design, fabrication and control of origami robots. Nature Reviews Materials, 2018, vol. 3, no 6, p. 101-112.

SANABRIA-BARBOZA, Diana. El Rolling Bridge de Londres. Master Thesis, Programa de Ingeniería Estructural. Universidad de Costa Rica , 2015.

SELIG, Jon M. Geometric fundamentals of robotics. Springer Science and Business Media, 2004.

TANAKA, Kazuo; WANG, Hua O. Fuzzy control systems design and analysis: a linear matrix inequality approach. John Wiley and Sons, 2004.

TARBOURIECH, Sophie, et al. Stability and stabilization of linear systems with saturating actuators. Springer Science and Business Media, 2011.

TSAI, Lung-Wen. Robot analysis: the mechanics of serial and parallel manipulators. John Wiley and Sons, 1999.

VICHIK, Sergey; BORRELLI, Francesco. Solving linear and quadratic programs with an analog circuit. Computers and Chemical Engineering, 2014, vol. 70, p. 160-171.

YOU, Zhong; CHEN, Yan. Motion structures: deployable structural assemblies of mechanisms. Crc Press, 2011.

YU, Jingjun; JIN, Zhao; KONG, Xianwen. Identification and comparison for continuous motion characteristics of three two-degree-of-freedom pointing mechanisms. Journal of Mechanisms and Robotics, 2017, vol. 9, no 5, p. 051015.

ZANARDO, Agostino. Two-dimensional articulated systems developable on a single or double curvature surface. Meccanica, 1986, vol. 21, no 2, p. 106-111.

ZHAO, Jing-Shan; CHU, Fulei; FENG, Zhi-Jing. The mechanism theory and application

of deployable structures based on SLE. **Mechanism and Machine Theory**, 2009, vol. 44, no 2, p. 324-335.

ZHAO, Jing-Shan, et al. Structure synthesis and statics analysis of a foldable stair. **Mechanism and Machine Theory**, 2011, vol. 46, no 7, p. 998-1015.

ZHOU, Lifeng, et al. Projection kinematic analysis of DNA origami mechanisms based on a two-dimensional TEM image. **Mechanism and Machine Theory**, 2017, vol. 109, p. 22-38.

APPENDIX A – GENERAL FOLDING CONDITIONS

In this Appendix, it is presented the folding conditions that must be achieved by all the planar and spherical SLE assemblies in order to ensure folding capability.

A.0.1 General folding conditions

Under the fact that SLE assemblies are able to be stored in a compact shape, then it is necessary to determine conditions to ensure the folding and deploying state of the assembly.

Figure 71 – Folding conditions for conventional SLE assemblies

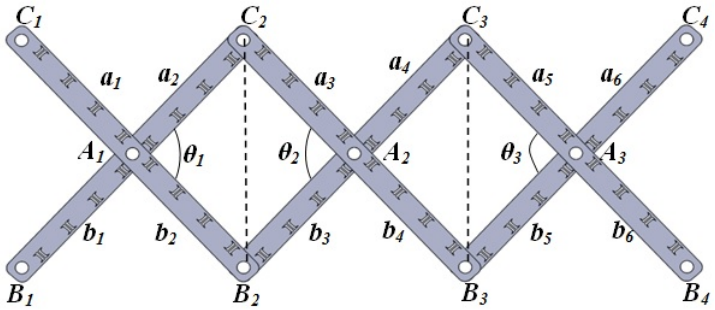

Source – From the author.

Figure 71 shows an assembly of three SLE units. At compact configuration the points $A_{1,2,3}$, $B_{1,2,3,4}$ and $C_{1,2,3,4}$ of all three SLE units must be collinear. So, when cosine rule is applied to $B_2A_1C_2$ and $B_2A_2C_2$ we have:

$$a_2^2 + b_2^2 - 2a_2b_2\cos\theta_1 = a_3^2 + b_3^2 - 2a_3b_3\cos\theta_2 \tag{88}$$

in Equation (88) if $\theta_1 = \theta_2 = \pi$ (at compact state), then we conclude that:

$$a_{i-1} + b_{i-1} = a_i + b_i \tag{89}$$

Equation (89) (ESCRIG, F., 1985) is the basic folding condition for SLE assemblies of translational and polar planar units. For the spherical case, let choose a point O_1 in the convex region of the SLE assembly of Figure 72, from this point let draw a line to the linking hinges ($E_{2,3}$, $F_{2,3}$) between SLE units, then in compact state it must be necessary to have the same arc length being necessary to achieve the conditions:

$$\begin{aligned} \overline{E_2F_2} &= \beta_1\overline{O_1E_2} \\ \overline{E_3F_3} &= \beta_2\overline{O_1E_3}. \end{aligned} \tag{90}$$

Figure 72 – Folding condition for spherical SLE

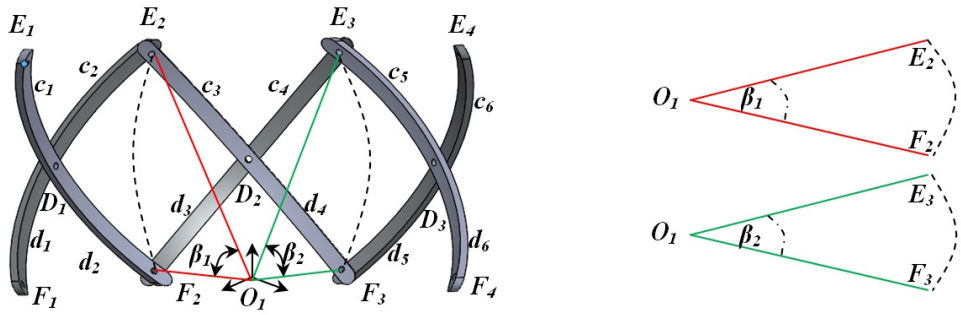

Source – From the author.

The condition in Equation (90) (GRIJALVA et al., 2021) holds only if $O_1E_2 = O_1F_2$ and $O_1E_3 = O_1F_3$. This condition can be interpreted as an spherical restriction, it means that the common plane where the bars of the spherical SLE bars rotate freely has spherical geometry.

ANNEX A – ALGORITHMS TO OPERATE DUAL QUATERNIONS IN MATLAB

The algorithms below[1] (RADAVELLI, L., 2013) were used in this thesis to operate with dual quaternions

CONJUGADOS E DUAIS

ConjDual

```
% Dual de um Quatérnio Dual
%
% Para h = [a0 a1 a2 a3 b0 b1 b2 b3]' um quatérnio dual,
% ConjQuatDual(h) resulta
% dual(h) = [a0 a1 a2 a3 -b0 -b1 -b2 -b3]'
%
function y = ConjDual(h)
q1 = h(1:4);
q2 = h(5:8);
y = [ q1
-q2 ];
```

ConjQuat

```
% Função que retorna o conjugado de um Quatérnio
%
% Para q = [a0 a1 a2 a3]' um quatérnio,
% ConjQuat(q) resulta q* = [a0 -a1 -a2 -a3]'
%
function y = ConjQuat(q)
y = [ q(1) -q(2) -q(3) -q(4) ]';
```

ConjQuatDual

```
% Conjugado de um Quatérnio Dual
h* = q1*+q2*e
% % Para h = [a0 a1 a2 a3 b0 b1 b2 b3]' um quatérnio dual,
% ConjQuatDual(h) resulta
```

[1] To avoid translation errors, the functions and comments were kept in the language (Portuguese) presented in the original version.

```
% h* = [a0 -a1 -a2 -a3 b0 -b1 -b2 -b3]'
%
function y = ConjQuatDual(h)
q1 = h(1:4);
q2 = h(5:8);
y = [ ConjQuat(q1)
ConjQuat(q2) ];
```

PRODUTOS

```
% Produto entre Quatérnios
%
% Para q1 = a0+q1 = x + u
% q2 = b0+q2 = y + v
% ProdQuat(q1,q2) resulta
% q1q2 = [x*y-u'*v
% x*v+y*u+ProdExterno(u,v)];
%
function P = ProdQuat(q1,q2)
% Produto definido vetorialmente
x = q1(1);
u = q1(2:4);
y = q2(1);
v = q2(2:4);
P(1,:) = x*y-u'*v;
P(2:4,:) = x*v+y*u+ProdExterno(u,v);
% Produto definido matricialmente
a = q1;
M = [a(1) -a(2) -a(3) -a(4)
a(2) a(1) -a(4) a(3)
a(3) a(4) a(1) -a(2)
a(4) -a(3) a(2) a(1)];
P = M*q2;
```

```
% Produto entre Quatérnios Duais
%
```

```
% Para h1 = q11 + e(q12)
% h2 = q21 + e(q22)
% ProdQuatDual(h1,h2) resulta
% h1h2 = q11q21+e(q11,q22+q12,q21)
%
function y = ProdQuatDual(h1,h2)
a1 = h1(1:4); d1 = h1(5:8);
a2 = h2(1:4); d2 = h2(5:8);
y = [ProdQuat(a1,a2)
ProdQuat(a1,d2)+ProdQuat(d1,a2)];
```

OPERADORES

```
% Operador de rotação via Quatérnio utilizado
% na aplicação simples (AS) - parâmetros na íntegra
%
% Para 's' o vetor que define o eixo de rotação,
% 'ta' o ângulo de rotação,
% QuatRotAS(s,ta) resulta
% q = cos(ta) + s sen(ta)
%
function q = QuatRotAS(s,ta)
if norm(s) =1
s = s./norm(s);
end
sx = s(1); sy = s(2); sz = s(3);
q = [ cos(ta)
(sin(ta))*sx
(sin(ta))*sy
(sin(ta))*sz ];
```

```
% Operador de rotação via Quatérnio
% utilizado na aplicação conjugada (AC)
%
% Para 's' o vetor que define o eixo de rotação,
% 'ta' o ângulo de rotação, % QuatRotAC(s,ta)
```

```
% resulta q = cos(ta/2) + s sen(ta/2)
%
function q = QuatRot(s,ta)
if norm(s) =1
s = s./norm(s);
end
sx = s(1); sy = s(2); sz = s(3);
q = [ cos(ta/2)
(sin(ta/2))*sx
(sin(ta/2))*sy
(sin(ta/2))*sz ];


        % % Operador de Movimento Helicoidal - SDQ
%
% Para 'd', 'ta', os parâmetros do movimento helicoidal,
% 's', o vetor diretor que define o eixo helicoidal,
% SDQ(d,ta,s) resulta no operador SDQ do movimento helicoidal
%
function h = SDQ(d,ta,s)
sx = s(1); sy = s(2); sz = s(3);
mx = m(1); my = m(2); mz = m(3);
h = [ cos(ta/2)
(sin(ta/2))*sx
(sin(ta/2))*sy
(sin(ta/2))*sz
-d/2*sin(ta/2)
(d/2*cos(ta/2))*sx
(d/2*cos(ta/2))*sy
(d/2*cos(ta/2))*sz ];
```